DOE/ER/45449 - 3

ABSTRACT OF DISSERTATION
GRADUATE SCHOOL, UNIVERSITY OF ALABAMA AT BIRMINGHAM

Degree Ph. D. Program Materials Engineering

Name of Candidate Hongjun Zuo

Committee Chair(s) Raymond G. Thompson and Robin Griffin

Title Mechanism of Constitutional Liquid Film Migration

Liquid film migration (LFM) in liquid phase sintering classically involves a large metastable liquid volume adjacent to solid, and migration occurs at an isolated solid-liquid (S-L) interface. Constitutional liquid film migration (CLFM), discovered in alloy 718, has major characteristics similar to those of LFM, except that the metastable liquid is from the constitutional liquation of precipitates on the grain boundary. The similarity between LFM and CLFM has led to the theory that coherency lattice strain responsible for LFM is also responsible for CLFM.

The coherency strain hypothesis was tested in this study by evaluating whether the Hillert model of LFM would also apply for CLFM. Experimental results of CLFM in alloy 718 showed that migration velocity followed the trend predicted by the Hillert model. This indicates that the coherency strain hypothesis of LFM also applies for CLFM and that the coherency lattice strain responsible for LFM is also the driving force for CLFM.

Constitutional liquid film migration was also successfully sought in a Ni-16%Nb binary alloy. The experimental results showed that migration velocity varied as a function of isothermal holding time, following the trend predicted by the modified Hillert model for samples precipitated at each of the aforementioned temperatures. This result was taken as proof of the validity of the coherency strain hypothesis of LFM for CLFM.

The peak migration velocity was found to be affected by precipitation temperature. A lower precipitation temperature yielded a larger interface concentration difference and hence a higher lattice strain in the diffusion layer ahead of the migrating interface. The higher strain causes a larger concentration gradient across the liquid film and thus a peak migration velocity. Handwerker's model and related experimental evidence have suggested that the peak velocity varies with lattice strain in a parabolic manner for LFM. The experimental result in this dissertation demonstrated that this was also the case for CLFM. Thus, the coherency strain hypothesis of LFM also holds for CLFM.

DISCLAIMER

DISCLAIMER

Portions of this document may be illegible in electronic image products. Images are produced from the best available original document.

ACKNOWLEDGMENTS

My sincere gratitude goes to my advisor and the chairman of my Ph.D. committee, Dr. Raymond G. Thompson, for his extreme patience and guidance throughout all phases of this project. His role model as a professor and, more importantly, as a terrific human being, has inspired me to grow both personally and professionally. The team spirit which he has been advocating and fostering not only has made everything possible for me in the past but also will motivate me to always win as a team player.

I also would like to thank the co-chairman of my Ph.D. committee, Dr. Robin Griffin, for her support and supervision, especially during the late stage of this project. Her invaluable assistance in my graduate work at UAB will be forever remembered.

The input and assistance from other committee members, Dr. Burton R. Patterson, Dr. Mike Rigsbee, and Dr. John Barnard, are also greatly appreciated. Nothing would have been possible without their encouragement and supervision.

TABLE OF CONTENTS

TABLE OF CONTENTS (Continued)

LIST OF TABLES

LIST OF FIGURES

LIST OF FIGURES (Continued)

LIST OF FIGURES (Continued)

LIST OF FIGURES (Continued)

LIST OF SYMBOLS

Symbol	
ε	Lattice strain
Y	Orientation dependence modulus
a	Lattice parameter
ε_0	Lattice strain constant when Vegard's law holds
C^{L1}	Liquid film interfacial composition in equilibrium with solid interfacial composition
C_s	Solid interfacial composition in equilibrium with the liquid film C^{L1}
C_∞	Matrix composition away from the liquid film
C_A	Average alloy composition
v	Migration velocity
D_L	Solute diffusivity in the liquid
D_s	Solute diffusivity in the lattice
κ	Curvature
V_M	Molar volume
t	Liquid film thickness
Δc_0	Concentration gradient across the film
λ	Isothermal holding time

CHAPTER 1.

INTRODUCTION

A. *Diffusion Induced Grain-Boundary Migration and Liquid Film Migration*

Diffusion induced grain-boundary migration (DIGM) is a recently discovered phenomenon initially associated with polycrystalline thin films in electronic materials (1-3). The microstructural features which distinguished DIGM from the curvature driven migration processes were an increase in grain boundary surface area as a result of the migration process, migration away from the center of curvature, and the formation of a solid solution zone behind the migrating boundaries.

Liquid film migration (LFM) can be qualitatively considered a variant of the DIGM process if the grain boundary is replaced by a liquid film. Liquid film migration exhibits all of the microstructural features associated with DIGM. In fact, in the liquid sintering of Mo-Ni systems (4), LFM and DIGM were found to occur simultaneously, indicating that the driving force for the two processes might be the same. Thermodynamically, however, there are differences between DIGM and LFM. In LFM, the solute concentration in the matrix at the solid-liquid (S-L) interface is related to the equilibrium

partition coefficient of the solute. The simultaneous presence of solid and liquid results in a loss of degree of freedom, and in a binary alloy, the solid and liquid concentrations are fixed by the appropriate tie-line at the existing temperature. However, in DIGM the matrix solute concentration at the S-L interface is less constrained since the grain boundary and matrix can exist over a wide range of compositions at any given temperature.

1. *Coherency strain hypotheses for liquid film migration*

A driving force coupling the migration of the liquid film and the transfer of solute atoms from the liquid film to the adjacent matrix should exist during migration. Several hypotheses have been proposed for the driving force for migration during LFM and DIGM (5). The one that explains many of the experimental observations is the coherency strain hypothesis (6). The following sections are devoted to the description of this hypothesis and two models derived from this hypothesis.

HANDWERKER'S MODEL

According the coherency strain hypothesis, the lattice diffusion of solute into the matrix is very slow relative to solute diffusion along the liquid film, as well as across the liquid film. The relatively slow lattice diffusion causes a solute-rich and volume-constrained diffusion layer on each side of the liquid. The lattice parameter in this constrained diffusion layer varies with solute concentration according to

Vegard's law. Therefore, lattice strain exists in this unstrained diffusion layer due to the composition change. This diffusion layer is said to be "coherently strained" with the matrix in the sense that the lattice bonding between the unstrained diffusion layer and unstrained matrix remains continuous. In this model, coherency is maintained during diffusion of solute from the liquid film into the matrix during migration.

Cahn (7) has calculated the strain energy for a coherent surface layer of composition, C_s, and lattice parameter, a, on a solid of composition, C_0, and lattice parameter, a_0. The strain energy was calculated by calculating the work required to elastically deform a slice of material so it can be added coherently to a solid with a different lattice parameter, as shown in Figure 1.

If the composition change is normal to the surface (the x-direction), the surface layer must be subjected to a strain of

$$\delta=(a-a_0)/a_0 \qquad [1]$$

in the plane of the surface (the y and z directions). The deformation required to produce this strain is done in two steps: first, the surface layer is deformed hydrostatically to produce the required strains in the y and z directions; second, the stress in the x direction is allowed to relax reversibly, while the sides of the surface layer parallel to the x direction are clamped. This deformation is, thus,a plan

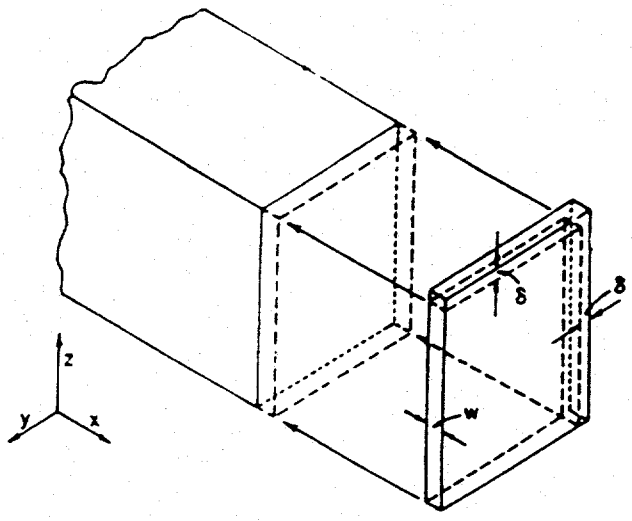

Fig.1--Schematic of coherency lattice strain model (Ref. 7).

plane strain. For cubic crystals, the coherency strain energy is

$$f_{coherent} = \text{elastic energy} = \sigma_{el}\,\epsilon = E\,\epsilon^2 = Y(\bar{n})\delta^2 \qquad [2a]$$

and

$$Y = E/(1-\upsilon), \qquad [2b]$$

where σ_{el} is the elastic stress, ϵ is the elastic strain, $Y(\bar{n})$ is an orientation-dependent elastic modulus, and δ is the lattice strain. For elastic isotropy, E is Young's modulus and υ is poisson's ratio. If stress relaxation occurs, the magnitude of δ will be reduced. In particular, δ equals zero if the diffusion layer is completely unstressed ($\sigma = 0$) due to plastic flow or chemical homogeneity or because the lattice parameter does not vary with composition.

The strain δ is related to compositional variation through the lattice parameter a_0 of the unstrained solid of average composition C_0. Taylor's expansion about C_0 yields

$$a = a_0\,[1 + \eta\,(C-C_0) + \cdots] \qquad [3a]$$

and

$$\delta = (a-a_0)/a_0 = \eta(C_s-C_0), \qquad [3b]$$

where $\eta = (da/dC)/a(C_0) = d\ln a/dC$ and the derivatives are evaluated at C_0; η becomes a constant when the change in lattice parameter with composition is constant (Vegard's law). Therefore, when neglecting higher order terms, the strain δ can be expressed as a function of composition C_s.

Substituting Eq. [3b] back to Eq. [2a] yields Eq. [4]. Equation [4] expresses the dependence of the strain energy in

the diffusion layer as a function of composition C_s (7):

$$f_{coherent} = Y(n)\eta^2(C_s - C_0)^2. \qquad [4]$$

Larche and Cahn (8) have recently derived the conditions for equilibrium between binary liquids and planar, non-hydrostatically-stressed solid solutions by the simultaneous solution of two equations for the concentrations of each phase. These thermodynamic expressions have been modified to include the effects of curved interfaces on interfacial equilibria. On the basis of the calculated composition gradient in the liquid film between two stressed and curved solids, the kinetics of liquid film migration have been treated as a boundary-value diffusion problem (9,10).

For a curved and stressed solid in equilibrium with a liquid, the free energy of the solid is (8,9)

$$f_{total} = f_{chemical} + f_{coherent} + f_{curvature}, \qquad [5]$$

where $f_{chemical}$ is the chemical free energy, $f_{curvature}$ is σx, σ is the isotropic solid-liquid interfacial energy, x is $(1/r_1 + 1/r_2)$, and r_1 and r_2 are the signed principal radii of curvature of the interface. The equilibrium concentrations of the solid and liquid can be derived as outlined below.

For dilute solutions, the equilibrium conditions for a stressed and curved solid in contact with a liquid are (a)

$$\mu_1^{o,s} - \mu_2^{o,s} + RT\ln\frac{\overline{Y}_1^s\overline{C}^s}{\overline{Y}_2^s(1-\overline{C}^s)} + 2V_m Y(\overline{n})\eta^2(\overline{C}^s - C_0) = \mu_1^{o,l} - \mu_2^{o,l} + RT\ln\frac{\overline{Y}_1^l\overline{C}^l}{Y_2^l(1-\overline{C}^l)} \qquad [6a]$$

and

$$\mu_1^{o,s}+RT\ln\gamma_1^s(1-\bar{C}^s)+V_m Y(\bar{n})\eta^2(C_0^2-(\bar{C}^s)^2)+2x\sigma=\mu_2^{o,l}+RT\ln\gamma_2^l(1-\bar{C}^l). \qquad [6b]$$

For an unstressed and planar solid in contact with its liquid, the equilibrium conditions are

$$\mu_1^{o,s}-\mu_2^{o,s}+RT\ln\frac{\gamma_1^s C^s}{\gamma_2^s(1-C^s)}=\mu_1^{o,l}-\mu_2^{o,l}+RT\ln\frac{\gamma_1^l C^l}{\gamma_2^l(1-C^l)} \qquad [7a]$$

and

$$\mu_2^{o,s}+RT\ln\gamma_2^s(1-C^s)=\mu_2^{o,l}+RT\ln\gamma_2^l(1-C^l) \qquad [7b]$$

where the components are labeled 1 and 2, as in Figure 2; T is the temperature, $u_i^{o,s}$ and $u_i^{o,l}$ are the standard chemical potentials, and $\gamma_i^{o,s}$ and $\gamma_i^{o,l}$ are the activity coefficients of the ith component in the solid and liquid, C^s and C^l are the mole fractions of component 1 in the solid and liquid, V_m is the molar volume of the solid, x is the mean curvature, σ is the isotropic solid-liquid interfacial energy, and $\bar{}$ indicates quantities dependent on the hydrostatically stressed solid and liquid.

Equations [6a]-[7b] were derived from the basic laws of thermodynamics. They imply, however, a simple graphical construction (Figure 2) on a free energy diagram for the solutions of Eqs. [6] and [7] for C^s and C^l and for $\bar{C}^s$ and $\bar{C}^l$, respectively. The tangent to the free energy curve for the solid must be parallel to that of its equilibrium liquid, as stated in Eqs. [6a] and [7a]. Furthermore, the tangents to the

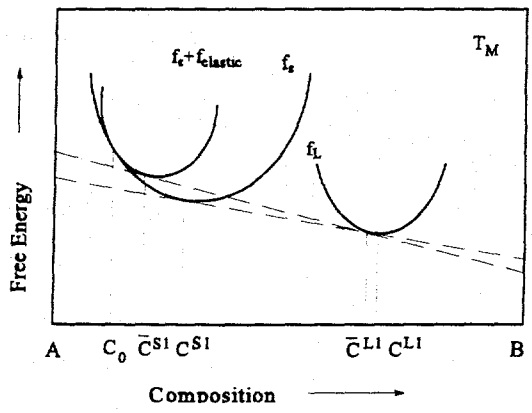

Fig. 2--Free energy versus composition diagrams for liquid film in contact with matrix. C^{S1} and C^{L1} are the compositions in the matrix and the liquid, respectively, in the absence of coherency stress in the matrix. $\bar{C}^{S1}$ and $\bar{C}^{L1}$ are the altered compositions due to the presence of coherency stress in the matrix (Ref. 6).

solid and liquid must go through a common point, as stated in Eqs. [6b] and [7b]. These two conditions together define the common tangent shown schematically in Figure 2.

It is worth while to examine explicitly the implications of incorporating δ and $f_{coherent}$ (Eqs. [2] and [4]) into the conditions for coherent equilibrium, Eqs. [6a] and [7b]. Equation [4] states that the strain in the alloyed region is dependent only on the difference in lattice parameters between the surface composition, $\overline{C}^s$, and the initial matrix material, C_0. Thus, the composition profile and the thickness of the diffusion layer have no effect on the strain of the surface layer in contact with the liquid. Furthermore, Eqs. [6a] and [7a] imply that local equilibrium is maintained at the solid-liquid interface.

The concentration of a liquid in equilibrium with a stressed and curved solid was found to be (5)

$$\overline{C}^l = C^l + \left[\frac{Y(\overline{n})\eta^2 V_m \frac{RT}{C^s(1-C^s)}\left[1+\frac{\partial \ln\gamma^s}{\partial \ln C^s}\right]}{2Y(\overline{n})\eta^2 V_m + \frac{RT}{C^s(1-C^s)}\left[1+\frac{\partial \ln\gamma^s}{\partial \ln C^s}\right]}\right](C^s-C_0)^2 + 2\sigma\kappa V_m \times \frac{C^l(1-C^l)}{RT(C^l-C^s)}\left[1+\frac{\partial \ln\gamma^l}{\partial \ln C^l}\right]^{-1}. \quad [8a]$$

The liquid concentration in equilibriumin terms is the concentration for an unstressed planar solid C^s in equilibrium with a liquid of composition C^l; γ^l and γ^s are the activity coefficients of the solute in the liquid and solid, respectively. The equilibrium liquid composition depends on the local crystallographic orientation, as defined by the

... to the interface, $\bar{n}$; the local interface curvature, x; ... composition C_0 of the underlying matrix. Equation [8a] ... simplified significantly, as follows, assuming that the ... strain limit and Henrian solution behavior apply

$$\left|\frac{Y(\bar{n})\eta^2 V_m \frac{RT}{C^s(1-C^s)}[1+0]}{2Y(\bar{n})0^2 V_m + \frac{RT}{C^s(1-C^s)}[1+0]}\right|(C^s-C_0)^2+2\sigma x V_m\}\times\frac{C^l(1-C^l)}{RT(C^l-C^s)}[1+0]^{-1}. \quad [8b]$$

$$\bar{C}^l=C^1+\left[Y(\bar{n})\eta^2(C^s-C_0)^2+2\sigma x\right]\frac{V_m C^l(1-C^l)}{RT(C^l-C^s)}. \quad [8c]$$

... grain A,

$$(\bar{C}^l)_A=C^1+\left[Y(\bar{n}_A)\eta^2(C^s-C_0)^2+2\sigma x_A\right]\frac{V_m C^l(1-C^l)}{RT(C^l-C^s)}. \quad [8d]$$

... grain B,

$$(\bar{C}^l)_B=C^1+\left[Y(\bar{n}_B)\eta^2(C^s-C_0)^2+2\sigma x_B\right]\frac{V_m C^l(1-C^l)}{RT(C^l-C^s)}. \quad [8e]$$

... grain A in contact with grain B,

$$\Delta C_l=(\bar{C}^l)_A-(\bar{C}^l)_B=\left[(Y(\bar{n}_A)-Y(\bar{n}_B))\eta^2(C^s-C_0)^2+2\sigma(x_A-x_B)\right]\frac{V_m C^l(1-C^l)}{RT(C^l-C^s)}. \quad [8f]$$

The kinetics of liquid film migration are then treated as ... boundary value problem for diffusion through the liquid

using Eq. [8b] to provide the boundary conditions for the flux by Hillert (6), which is briefly presented here and will be named Eq. [11] and discussed in detail in the next section:

$$v = (D_L \bullet V_M \bullet \Delta C_L) / (C^l - C^s)\, t. \qquad [11]$$

When the liquid film seperates two solid grains, A and B, of the same phase and the same initial composition but having different elastic coefficients, $Y(\overline{n}_A)$ and $Y(\overline{n}_B)$, and different curvatures, χ_A and χ_B, the $\overline{C}^l$ for each grain can be calculated from Eq. [8b] to be Eq. [8f]. The term ΔC_L in Eq. [11], which represents the compositional difference between two stressed solids $[(\overline{C}^l)_A - (\overline{C}^l)_B]$, can then be replaced with Eq. [8f]. Consequently, the velocity of the liquid film becomes

$$v = \frac{D_{liq} V_m}{tRT}\left[(Y(\overline{n_A}) - Y(\overline{n_B}))\,\eta^2 (C^s - C_0)^2 + 2\sigma(\chi_A - \chi_B) \right] \frac{C^l(1-C^l)}{(C^l - C^s)^2}. \qquad [9]$$

where t is the liquid film thickness and D_{liq} is the diffusivity through the liquid film. When the stress in grain B is completely relaxed, the coherent strain energy goes to zero in that grain and the velocity of the liquid film becomes

$$v = \frac{D_{liq} V_m}{tRT}\left[(Y(\overline{n_A})\,\eta^2 (C^s - C_0)^2 + 2\sigma(\chi_A - \chi_B) \right] \frac{C^l(1-C^l)}{(C^l - C^s)^2}. \qquad [10]$$

In describing the initiation of film motion, it has been assumed that the solid is initially homogeneous and stress free and is bordered by a compositionally homogeneous liquid.

... the conditions of the system are changed, either by ...ing the temperature or by adding solute to the system, ... compositions of the liquid and the solid will no longer be ... equilibrium compositions. There will be an initial ...ment, after which the liquid compositions will be in ...librium with the stressed surface layers of the solid, as ...cribed by Eq. [8]. If the values of C^1 are different for ... adjacent surfaces, a concentration gradient will exist in ... liquid and the film will migrate according to Eq. [9]. The ...ection of migration will depend on both the differences in ... and x in the two adjacent grains. When x is negligible, ... direction of migration is into the grain with larger ... (5,6).

In summary, for the purpose of this discussion, it has ...en assumed that LFM results from a coherent strain produced ... the matrix at the solid-liquid interface. Literature has ...en reviewed which presents the thermodynamic requirement ...at the concentrations of the solid in equilibrium with ...quid at the S-L interface are altered by the presence of ...attice strain in the diffusion layer. The equilibrium solid and liquid concentrations at the interface are obtained by the condition that the partial molar free energies of the solute in the solid and the liquid are equal. In the presence of a lattice strain in the diffusion layer, the free energy of the solid is increased, while that of the liquid remains the same. For a given solute, the lattice strain in the diffusion

... is directly proportional to the orientation dependent ... moduli (10). Hence, the lattice strains on either side ... the boundary will be unequal because of orientation ... across the grain boundary. The liquid in contact with ... diffusion layer having the higher lattice strain energy ... be more depleted in solute than the liquid in contact ... the diffusion layer having the lower lattice strain ... Hence, a concentration gradient is set up across the ... film, as shown in Figure 3, which activates diffusion ... solute across the film (5,6,10).

THE MODIFIED HILLERT MODEL

Using the Hillert model of equation [11] (5), Handwerker ... the kinetics of liquid film migration as a boundary ... problem for diffusion through the liquid. Handwerker ... Hillert's model of equation [11] to describe the mass ... for DIGM/LFM process (6). Handwerker (6) further ... Hillert's equation for the mass balance between ... and precipitation to LFM.

The presence of coherency strains creates conditions of ... equilibrium at the interface. When two solid ... are separated by a liquid film, the composition at ... solid-liquid interfaces becomes the boundary conditions ... the one-dimensional problem of diffusion through a liquid ... When the coherency strain energies in two adjacent ... are different, a concentration gradient will exist in ... liquid across the film. Diffusion will occur across the

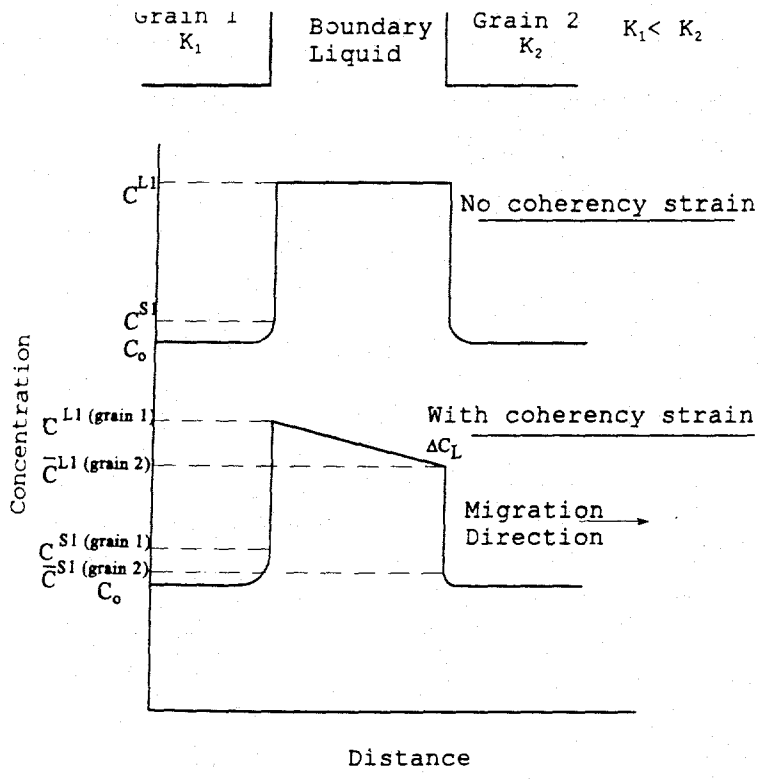

Fig. 3--Concentration gradient which occurs in a grain boundary liquid film due to the presence of coherency strains in the diffusion layer adjacent to the solid-liquid interface. K_1 and K_2 are the orientation dependent modules of grain 1 and grain 2 respectively (Ref. 8).

..quid film, and the liquid film will migrate by dissolution : one grain and reprecipitation onto the other grain. The ..lution to this diffusion problem with the boundary ..nditions that the concentrations of the solid and liquid at ..e two interfaces are constant at any time during migration ..eads to a migration velocity given by Hillert (6) as

$$v = (D_L \bullet V_M \bullet \Delta C_L) / (C^l - C^s)\, t, \qquad [11]$$

where v is the migration velocity; D_L is the solute diffusivity in liquid; V_M is the molar volume of solute, which is assumed to be constant in both the solid and the liquid; ΔC_L is the concentration difference in the liquid; t is the instantaneous film thickness; and the term $(C^l - C^s)$ accounts for conservation of mass at the interface. This results in a migration velocity which is inversely proportional to the film thickness and directly proportional to the lattice strain energy (through the ΔC_L term). The direction of migration is into the grain which has the higher lattice strain at the S-L interface. In Figure 3, the migration occurs to the right, as shown, and the lattice strain in grain 2 is assumed to be higher than in grain 1. The above expression neglects the effect of curvature on the lattice strain, assuming the grain boundary is flat prior to migration. It is also assumed that there is no in-plane flux of solute along the liquid film.

The effect of an in-plane solute flux in the liquid (Figure 3), due to a systematic variation in the thickness of

migrating film, on the migration velocity during LFM has been addressed by Brechet and Purdy (11). It was shown (12) that in the presence of such an in-plane flux of solute atoms along the liquid film, the film remains continuous due to the continuous supply of liquid so that the migration velocity could reach a steady-state value (12). Without the in-plane flux, the liquid film will shrink in thickness, break, and collapse into grain boundary. Hence, no steady state can sustain. The steady-state value was determined by the condition that the in-plane solute flux be equal to the solute flux transferred across the migrating liquid film in growing the solute-rich grain. The steady-state velocity was shown to be (12)

$$v = (12\sigma D_L / 5L^2) \cdot [(4C_o / C^l \bar{x} L) - 1], \qquad [12]$$

where σ is the solid-liquid interfacial energy, D_L is the solute diffusivity in liquid, L is the length of the liquid film, C_o is the solute concentration of the matrix in the growing grain, C^l is the solute concentration in the liquid at the trailing interface, and $\bar{x}$ is the average curvature of the liquid film. The steady-state migration velocity is dependent on the rate at which solute is supplied to the liquid film, as determined by D_L. However, as pointed out by Brechet and Purdy (11), the attainment of steady state would be highly improbable since it requires the right combination of several variables (D_L, L, $\bar{x}$) which should simultaneously satisfy Eqs.

[11] and [12]. For instance, when the liquid diffusion rate is fast, it requires the film length L to be great and the capillary term $(1/\bar{x})$, which produces the lateral gradient, to be small to obtain the steady state. Additionally, because of the constantly changing curvature, a steady-state migration is not attainable.

2. *Experimental evidence of coherency lattice strain hypothesis*

One approach to test the coherency strain model for LFM would be to compare the observed migration velocity with that calculated from the model (i.e., Eqs. [10] and [11]). Due to the difficulty of experimentally measuring many of the factors in Eqs. [10] and [11] in situ, calculation of migration velocity relies largely on estimated data such as diffusivity and film thickness. Consequently, quantitative tests of these models have limitations, and a qualitative test, which relies on a fewer number of parameters, is still of practical meaning. Such a test will be discussed in section 1 of part B in this chapter.

Another way to test the coherency strain model is by demonstrating that the migration velocity indeed varies as a function of lattice strain δ^2. Although qualitative, this would provide evidence that Eq. [10] describes the mechanistic behavior of LFM and that coherency strain is its driving force. In the liquid phase sintering of Mo-Ni alloy, Song *et al.* (13) showed that the migration rates of the liquid films

were proportional to δ^2. Furthermore, in liquid phase sintering of Mo-Ni embedded in a Mo-Ni-Co-Sn matrix (14), the Co/Sn ratio was varied systematically to yield strains from negative to positive. A parabolic curve was obtained corresponding to the relationship between the migration velocity and δ^2 in Eq. [9] as shown in Figure 4. In particular, it should be noticed that migration velocity goes to zero as δ goes to zero, indicating that coherency strain energy is the driving force and that there is no additional driving force.

B. LFM from Constitutional Liquation-CLFM

In 1989, the discovery of a new interface migration mechanism, that of constitutional liquid film migration, was made (15). This form of LFM was similar in many respects to LFM observed by others (16-23). However, this newly discovered mechanism has produced migration velocities about two orders of magnitude greater than previously observed for LFM. Furthermore, the migration occurred in 1-10 seconds. These observations confirmed that CLFM was an extremely powerful migration mechanism.

A phenomenon which can result in the formation of a metastable grain boundary liquid is the "constitutional liquation" of second phase particles in a binary alloy (24, 25). Constitutional liquation of a second phase AB in an AB binary alloy can be explained with reference to Figure 5 (15). Alloy of composition C_o has a certain volume fraction of

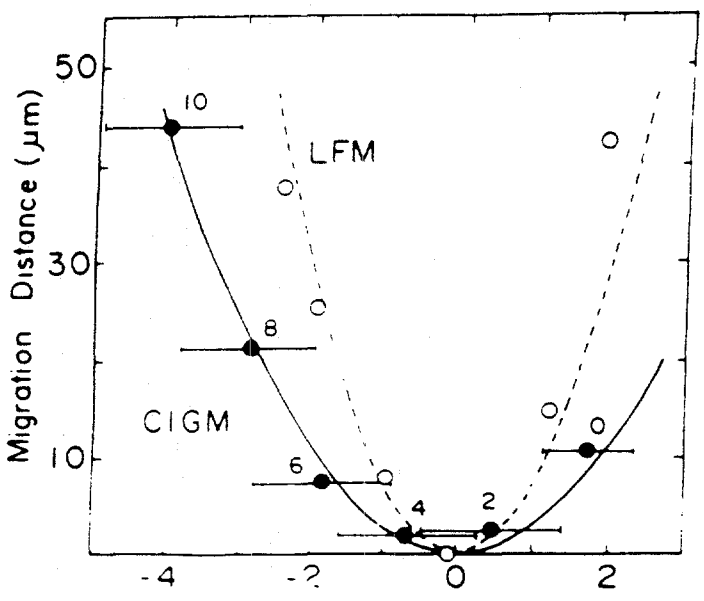

Fig. 4--The observed variation of the average migration distance/velocity for LFM with coherency strain in specimen all heated at 1460°C for 2 hours after embedding in Mo-Ni-Co-Sn liquids of varying Co/Sn ratio. The numbers above the data points indicate the decimal fraction of Co in Co-Sn. (Ref. 13).

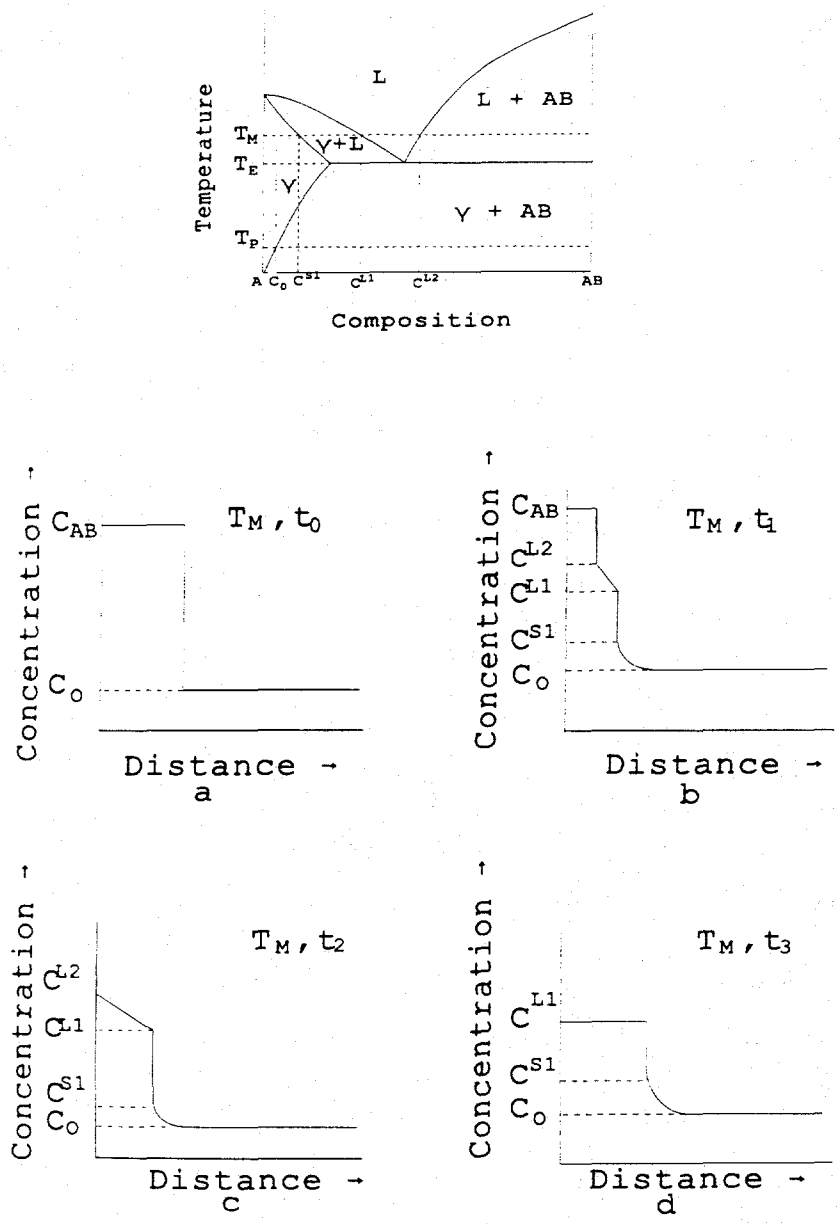

Fig.5--Schematic of constitutional liquation of AB particle in the binary system. (a) Initial configuration of the matrix-AB diffusion couple. (b) Constitutional gradients in front of the liquation AB particle in accordance with the phase diagram. (c) The formation of metastable concentration gradients in the liquid at the end of AB liquation. (d) Elimination of the metastable concentration gradient by diffusion (Ref. 15).

...nd phase particles at room temperature. When the alloy is ...idly heated to a temperature T above the eutectic ...perature T_E, such that there is insufficient time for ...olution of AB, a diffusion couple between the matrix of ...position C_m and AB is established at the peak temperature. ...uid of composition from C^{L1} to C^{L2} forms around the AB ...rticle in accordance with phase diagram requirements (16, ... The concentration gradient expected in front of the ...quating AB particles is shown in Figure 5b. The movement of ... AB liquid interface to the left is governed by the solute ...ffusivity in liquid, as shown in the following equation:

$$V_{AB}=\frac{D_{Liq}(C^{L2}-C^{L1})}{(C_{AB}-C^{L2})\,d}, \qquad [13]$$

...ere d represents the horozontal distance between C^{L2} and C^{L1}. ... AB liquation is expected to take place very rapidly, and ... situation shown in Figure 5c is obtained. The liquid from ...ese liquating particles will enter the grain boundary, ...ther from the particles situated on grain boundaries or from ...se particles intercepted by the moving boundaries. The ...quated pools will spread along grain boundaries because of ...rface tension forces and will ultimately be present in the ...rm of grain boundary films. Since the liquid is formed from ... particles which should not be present under equilibrium ...nditions, the liquid itself is metastable and should ...sappear by back-diffusion of solute from the liquid to the

matrix (18,26). The back-diffusion of solute from this liquid would then cause coherency strain to develop on each side of the liquid film. If this strain develops unevenly due to orientation differences on either side of the film, LFM of the misoriented boundaries (15,27) may initiate.

The Coherently Strained Layer in LFM and CLFM

It has been shown in previous sections that the driving force for LFM is the concentration gradient across the liquid film. The establishment of such a concentration gradient relies on the attainment of a coherently strained layer ahead of the migrating interface. The essence of having such a layer is to maintain a lower matrix solid concentration in equilibrium with the solute concentration in the liquid film. Once this layer is no longer coherently strained, the solute concentration in the solid will go up, and so will the equilibrium solute concentration in the liquid film. Hence, the concentration gradient in the liquid film will be eliminated.

The reason the coherently strained layer can be constrained rather than "relaxed" is that energy is needed to create misfit dislocation to relax the stress (8,9). The energy needed to create the misfit dislocation is independent of the layer thickness (9), but the coherency strain energy is proportional to the thickness of the constrained layer. A critical thickness of diffusion layer occurs when the

herency strain energy exceeds the energy needed to create misfit dislocations.

Two mechanisms by which the coherently strained layer may be altered are lattice diffusion and liquid film migration. Since steady-state diffusion is not favorable for building up coherently strained layer. LFM can also effectively alter the coherently strain layer since the migration direction is into the solid of higher coherency strain energy, thus effectively reducing the energy of the system.

The following paragraphs are intended to show the dependence of LFM/DIGM on the coherently strained layer in specific cases. The ultimate goal is to demonstrate that such a coherently strained layer can exist in an Ni-Nb diffusion couple and that such behavior is consistent with that of both Alloy 718 and Ni-16%Nb that were investigated in this dissertation.

According to the coherency strain hypothesis, the diffusion layer thickness, L, in the growing grain increases by both lattice diffusion and migration according to (28)

$$L=\sqrt{D_l\lambda}+v\lambda, \qquad [14]$$

where λ is the time of diffusion and v is the migration velocity; L reduces to $L = v\lambda$ at long times.

For the dissolving grain, L can be approximated as the following:

$$L=\sqrt{D_1\lambda}\left(\frac{\sqrt{D_1\lambda}}{\sqrt{D_1\lambda}+v\lambda}\right). \qquad [15]$$

The equation can be split into two equations for different situations:

$$L=\sqrt{D_1\lambda}, \qquad for\sqrt{D_1\lambda}\gg v\lambda \qquad [16a]$$

and

$$L=\frac{D_1}{v}, \qquad for\sqrt{D_1\lambda}\ll v\lambda. \qquad [16b]$$

The latter situation applies to all DIGM and LFM phenomena observed. A critical thickness thus exists beyond which the lattice diffusion is much greater than the migration velocity so that the coherently constrained layer will break away (28). The critical layer thickness can be expressed as

$$L_c = D_1/v. \qquad [17]$$

A major question about the application of coherency strain theory to DIGM when this phenomenon was first discovered was how much lattice diffusion (in other words, how thick the diffusion zone) was required to induce the boundary motion. It was initially suggested that DIGM could only occur when lattice diffusion was "frozen out" (*i.e.*, when the composition changed discontinuously across the grain boundary) (29).

The primary objection to the coherency strain model for DIGM is the widespread observation of DIGM at low temperatures where lattice diffusion is too slow (30). At these low temperatures, D_1/v is estimated to be around several atomic layers or less than 1nm. For example, DIGM occurs in Cu(Ni) at 350°C, where D_1/v was calculated to be 5.4×10^{-14} m.

However, both Den Broeder (31) and Tashiro and Purdy (32) established that slow or "frozen out" lattice diffusion is not a necessary condition for DIGM. In fact, significant lattice diffusion was observed during DIGM in Ni(Cu) at 900°C (31) and in Al(Zn) (32) at 160°C-190°C. For Ni diffusing into Cu at 900°C, $L_c=1.6\times10^{-6}$ m using D_1 from (33). For Zn diffusing into Al, Tashiro and Purdy calculated the following values of D_1/v: 1.1×10^{-6} m (166°C); 1.5×10^{-6} m (178°C); and 2.8×10^{-6} m (190°C). The calculated values are the same order of magnitude as those observed by etching differences (Al[Zn]) and by EDS (Cu[Ni]).

In the case of CLFM in alloy 718, the lattice diffusivity reported by Radhakrishnan and Thompson (26) can be shown as

$$D_1 = 300 \exp(-35800/T) \ (cm^2/sec.). \qquad [30]$$

The diffusivity of niobium that was calculated for 1227°C and 1240°C is 1.294×10^{-8} cm^2/second and 1.598×10^{-8} cm^2/second, respectively. Using the peak migration velocities of 2.3×10^{-6} m/second and 2.5×10^{-6} m/second for 1227°C and 1240°C, respectively, the following values of D_1/v are obtained for Nb diffusing into Ni: 5.6×10^{-7}m (1227°C) and 6.3×10^{-7} m (1240°C). These calculated values are about one order of magnitude

smaller than those in DIGM discussed above, indicating that a coherently strained layer is entirely possible for CLFM in alloy 718. A similar argument can be made for Ni-16%Nb alloy, which essentially has the same diffusion couple as alloy 718.

Dissertation Objectives

The coherency strain hypothesis has been assumed to be the mechanism responsible for CLFM in alloy 718 (27). However, the ability of the coherency strain hypothesis of LFM to describe the behavior of CLFM has not yet been substantiated, thus deserving a fundamental and systematic test. The purpose of this dissertation is to test the ability of the coherency strain hypothesis to describe CLFM. The analysis will include testing the coherency strain hypothesis for CLFM in alloy 718 using the modified Hillert model. It will also include a test on binary alloy systems exhibiting CLFM using Handwerker's model. The validity of the coherency strain hypothesis will be deduced from a comparison of the experimental results to the theoretical predictions.

CHAPTER 2.

EXPERIMENTAL PROCEDURE

Alloy Preparation

1. *Alloy 718*

Alloy 718 is a nickel-base superalloy which mainly consists of an FCC solid solution of nickel, iron, and chromium, with a significant amount of molybdenum and niobium. The alloy 718 used in this study was provided by Inco Alloy International. The alloy composition is shown in Table I.

Table I. Composition of Alloy 718 in Weight Percent (%)

Ni	52.44
Cr	18.23
Fe	19.06
Nb+Ta	5.05
Mo	3.01
Ti	1.00
Al	0.55
Co	0.26
Si	0.12
Mn	0.11
C	0.055
S	0.003
P	0.008
Cu	0.05
B	0.0037

The alloy 718 used in these experiments was heat treated at Inco Alloy using the following procedure:

1. The molten alloy was cast and hot rolled into a rod of 0.5 inch in diameter.
2. The alloy was put into a box furnace being held at 954°C and isothermally held for 1 hour at this temperature, followed by water quenching.
3. The alloy was put into a box furnace being held at 718°C and isothermally held for 8 hours, followed by furnace cooling to 621°C.
4. The alloy was isothermally treated at 621°C for 8 hours and air cooled.

The rod was cut into samples approximately 4 inches in ...gth. The samples were placed inside stainless steel bags ... solutioned in a Lindenberg box furnace with no atmosphere ...trol at 1093°C for 30 minutes, followed by water quenching. ... samples were then placed in a furnace at 650°C and aged ... 4 hours, followed by air cooling. This heat treatment ...wed for precipitation and growth of NbC on the boundary ... The heat treated samples were sanded with silicon ...ide paper to remove the thin oxidation layer which formed ... the surface during heat treatment. The samples thus ...repared were used for the constitutional liquation thermal ...le.

2. *Binary alloy*

a. *Binary alloy melting*

Nickel pieces 5cm×5cm×0.6 cm in size and niobium wires ...1 cm in diameter were purchased from Alfa Johnson Matthey.

purity was 99.99 pct for both Ni and Nb. The nickel was into 8 smaller pieces and the wire was cut into shorter pieces about 0.5 cm in length. Nickel and Nb materials were then weighted into the right proportion to make the binary alloy composition Ni-16%Nb by weight (Figure 6). The total weight of the ingot was controlled to be about 150 grams. Nickel pieces were then mixed with short Nb wires in a 99.8 % purity alumina crucible from Coors Ceramics. The crucible was subsequently loaded into an Advanced Vacuum System Inc. induction melting (VIM) system. The melting chamber of the VIM was monitored through a quartz window, and the temperature was recorded using a calibrated infrared radiation thermometer by IRCON.

The power of the system was manually increased to slowly heat up the system at a rate of 10°C/minute until the the high vacuum (< 10^{-5} torr) reading from the high vacuum gauge started to drop, indicating an increase in vapor pressure due to melting. To prevent arcing in the chamber induction coil associated with vapor out-gassing, it was necessary to flow argon at a rate of 15 psig into the chamber. The system was held at a constant power level for about 15 minutes for the melt to mix well under magnetic stirring provided by the induction current. The power was then cut off and the system was cooled down with circulating water that runs through the induction coil.

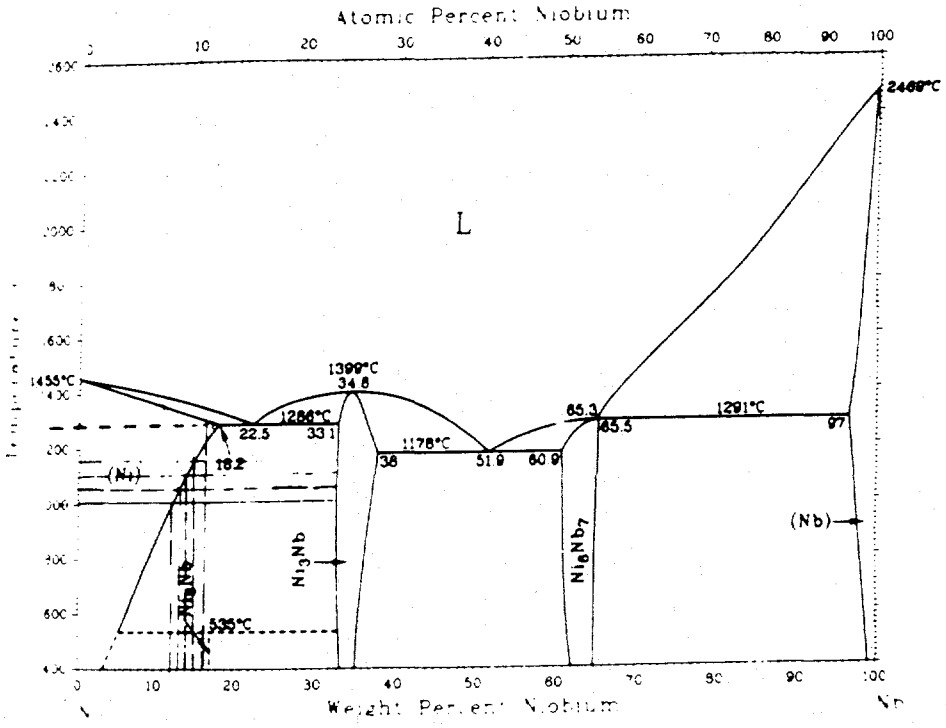

Fig. 6--Phase diagram of Ni-Nb binary system.

b. *Heat treatment*

The ingots were sealed in quartz ampules using a vacuum system equipped with a turbo-molecular pump that was backed up by a rotary pump. When the vacuum pressure reached 10^{-6} torr, argon was back filled to prevent the ampule from sagging at high temperature. The ampule was then sealed with a torch fueled with a mixture of hydrogen and oxygen.

Three sealed ampules were solutionized in a Lindenberg box furnace. The ampules were put on a refractory brick to be close to the thermocouple, which was located at the top of the furnace. Three other box furnaces were also heated to 1150°C, 1100°C, and 1050°C, respectively. After the ampules containing the samples were solutioned at 1290°C for 24 hours, they were transferred to the other three box furnaces. One ampule each was placed in a furnace at 1150°C, 1100°C, and 1050°C, where they were held isothermally for 72 hours. The ampules were then water quenched. A summary of heat treatment is provided in Table II.

Table II. Precipitation Heat Treatment of Ni-16%Nb Alloy

Group 1:	Solution H.T. 24 hrs at 1290°C, Precipitation H.T. 72 hrs at 1150°C.
Group 2:	Solution H.T. 24 hrs at 1290°C, Precipitation H.T. 72 hrs at 1100°C.
Group 3:	Solution H.T. 24 hrs at 1290°C, Precipitation H.T. 72 hrs at 1050°C.

Samples of approximately 1.5cm×1cm×1cm were prepared for thermal cycling in a DSI 1000 thermomechanical system made by

namic System Inc., which is commonly known as the "Gleeble ...." It was necessary to use small samples due to the ...terial availability. Figure 7 shows a schematic of the ...mple configuration used in the Gleeble 1000. The surfaces of ... extending 718 rods were machined parallel. The sample ...rfaces were ground flat using an automatic polishing ...achine. This was done to help ensure good electrical contact ...tween the machined 718 rods and the surfaces of the samples.

Constitutional Liquation Thermal Cycle

The high heating rate typical of welds is needed to ...oduce CLFM. This type thermal cycle can be produced in a ...ermal simulation device called DSI 1000 or commonly known as ...e Gleeble 1000, made by the Dynamic System Inc. A detailed ...escription of this thermomechanical device used in this study ... available in the literature (29). The device essentially ...nsists of a transformer, the secondary of which provides the ...rrent source for resistance heating. Specimens of suitable ...ometry can be connected in the secondary circuit between ...ater-cooled copper jaws. The output power to the secondary ...an be controlled by computer through the feedback from a ...ermocouple percussion welded to the specimen. The specimen ...s held between two alloy 718 anvils, and a high amperage ...ternating electric current is passed through (Figure 7).

A type K thermocouple was percussion welded to the ...idsection of the samples. Thin thermocouple wires, 0.01 inch ...n diameter, were used to minimize heat loss. In order to

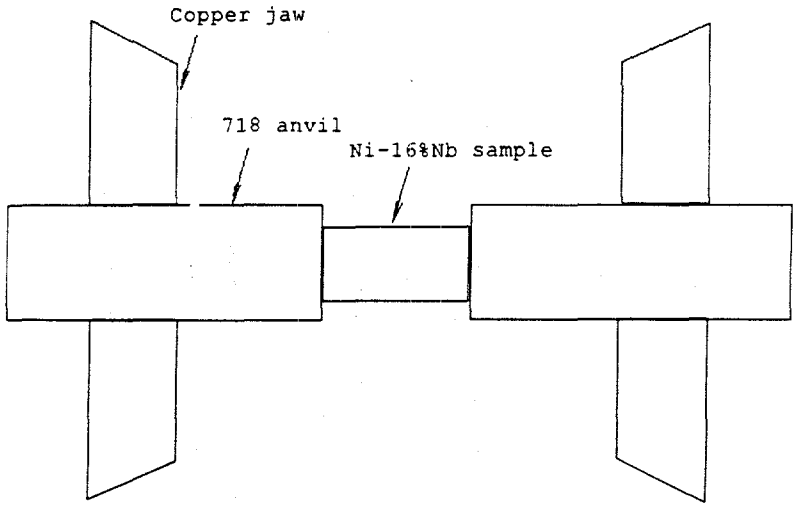

7--Schematic of Ni-16%Nb sample configuration for thermal cycling in the Gleeble machine.

...mote CLFM, the samples were subjected to rapid thermal ...les which were recorded by the thermocouples. A typical ...ermal cycle plot is shown in Figure 8. A heating rate of ... per second was used, in line with previous studies ...,34).

The alloy 718 samples were heated to a peak temperature ... 1227°C and held isothermally for various time intervals of ... 3, 5, 7, and 10 seconds. Samples were quenched to room ...perature in a jet of water.

Samples of Ni-16%Nb alloy from each of the three cycles ...re held at peak temperatures ranging from 1290°C to 1320°C ... for times varying from 1 to 10 seconds. It was observed ...at CLFM at 1300°C was significant and that the 718 rods ...lding the samples did not deform. Hence, the peak ...perature of 1300°C was used for CLFM thermal cycles for ...ples from all groups. Table III summarizes the temperature ... time used for each specimen.

Table III. Isothermal Hold at Peak Temperature of 1300°C for Ni-16%Nb Specimen Precipitate Heat Treated at Different Temperature

	Peak Temperature at 1300°C
Isothermal Holding Time for 1150°C precipitated	1, 3, 5, 7 and 9 seconds
Isothermal Holding Time for 1100°C precipitated	1, 3, 5, 7 and 9 seconds
Isothermal Holding Time for 1050°C precipitated	1, 3, 5, 7 and 9 seconds

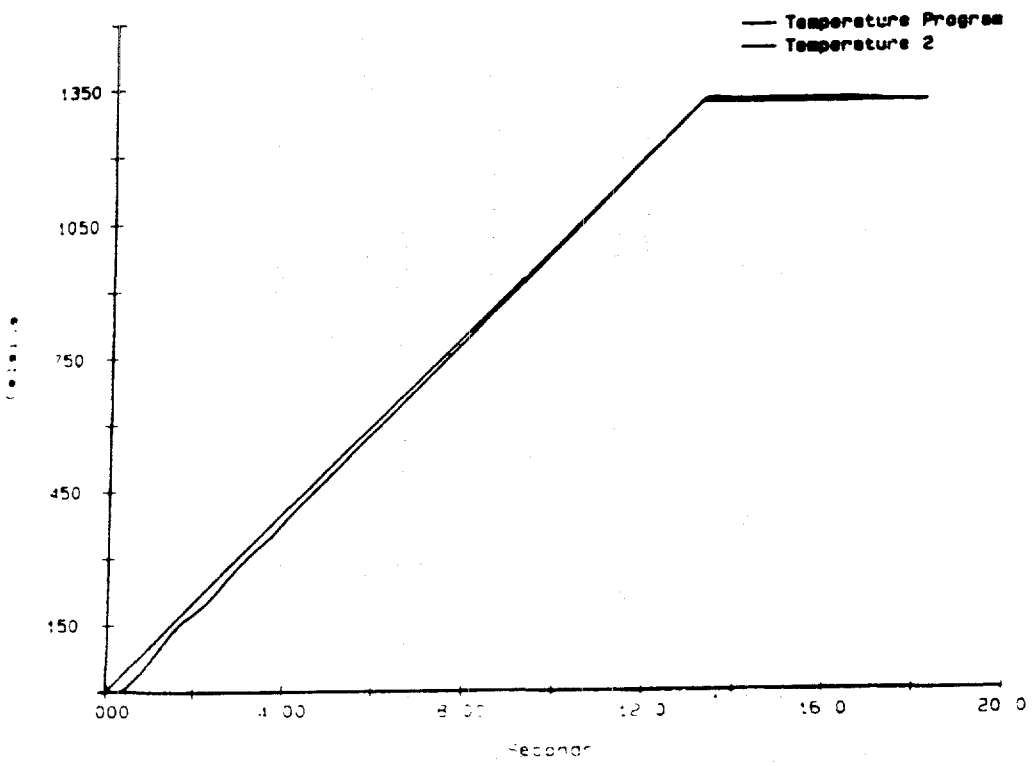

Fig. 8--A typical isothermal cycle producing CLFM for Ni-16%Nb alloy.

Metallography

All samples were prepared for light microscopy by mounting in bakelite and grinding on silicon carbide paper from 240 grit through 600 grit. The samples were then polished on a cloth using 6, 3, and 1 micron diamond paste. A 10 % oxalic acid electrolytical etching was used with alloy 718 to reveal the grain structure and NbC (27,28). The grain structure and Ni_3Nb phase of Ni-16%Nb alloy were revealed in a solution of 50 ml lactic acid, 30 ml nitric acid, and 10 ml hydrofluoric acid (35). To reveal the grain structure for CLFM, etching was performed electrolytically using 10 % oxalic acid for both alloy 718 and Ni-16%Nb alloy.

Migration Velocity Measurement

Migration velocity was measured using stereological techniques on micrographs taken with an optical microscope. The migration velocity was represented by a 3-D grain boundary surface area weighted velocity expressed by the Cahn-Hagel equation

$$v=\frac{1}{S}\frac{dV_v}{dt}, \qquad [18]$$

where v: the surface area (3-D grain boundary area) weighted interface migration velocity.

S_v: the surface area (3-D grain boundary area) per unit volume.

V_v: the volume fraction of the newly formed grains due to migration.

t: the holding time for each sample for migration.

V_V and S_V can be further expressed in terms of measurable parameters:

$$V_V=L_1=l/L \qquad [19]$$

$$S_V=2P_L=2N/L, \qquad [20]$$

where L_1: the line fraction.

l: the length of the test line intersected by migrated area.

L: the length of test line.

N: The number of intersections of test line with final migrated boundary.

The moving surface area is represented by S_V (grain boundary area in 3-D). In the case of CLFM, the surface area represented by the initial boundary was not moving with respect to the migrating boundary; therefore, this surface area should be excluded from averaging. In other words, the number of line intersection(s) with the initial boundary should not be included in N for calculating the surface area per unit volume when using Eq. [16]. The value of V_V versus isothermal holding time (t) was plotted and the slope representing dV_V/dt was obtained from the curve. With known V_V and dV_V/dt, migration velocity at each isothermal holding time was calculated using Eq. [18].

The above-mentioned S_v and V_v are calculated from ...ctive L_1 and P_1, with each being the averaged values over ...mber of observations. The number of observations of CLFM ...ach isothermal holding time was selected to yield a ...efficient of variation smaller than 0.1. All observations ... made from light micrographs with a magnification of 500X.

...uantitative EDS Composition Analysis

Quantitative EDS composition analysis was performed using ...hillips 515 SEM/Kevex 8000 EDS system to determine the ...rix composition of Ni-16%Nb samples that were heat treated ... different temperatures for second phase (Ni_3Nb) ...cipitation. The Ni-16%Nb samples, along with standards of ... pct pure Ni and 99.99 pct pure Nb, were mounted on the ... stub. This allowed the samples and standards to be ...posted to the same analyzing conditions. All the analyses ... carried out under an operating voltage of 16 kv and a 15° ... Niobium was analyzed using the L line, and Ni was ...yzed using the K line.

...-ray Determination of Lattice Parameters

The lattice strain in the coherently constrained layer ...ead of the migrating liquid film was shown to vary as a ...ction of composition (C_s-C_0) previously in Eq. [3b]:

$$\delta = (a-a_0)/a_0 = \eta\ (C_s-C_0). \qquad [3b]$$

When the change in lattice parameter with composition is ...stant (Vegard's law), η becomes a constant. When Eq. [3b] ... applied to CLFM in Ni-16%Nb binary system, C_s becomes the

composition in equilibrum with the liquid (Figure 6), a fixed value of 17.5%Nb, and C_0 is the matrix composition.

A test of Handwerker's model requires an intentional variation of lattice strain δ to evaluate whether migration mobility varies accordingly. A variation in δ can be obtained by varying the matrix composition C_0. Because a range of specific C_0 values can be obtained by precipitation heat treatment at different temperatures (Figure 6), δ for varying C_0 can be calculated using Eq. [3b], provided that the η is known value. Assuming Vegard's law holds, η becomes a constant and can be determined by studying the variation of lattice parameter with composition, as described in the following sections.

Samples of Ni-12%Nb and Ni-16%Nb ingots melted using the VIM system were homogenized for 24 hours at 1280°C, a temperature slightly below the eutectic temperature of 1286°C. The samples were then quenched in water to prevent second phase (Ni_3Nb) precipitation. In fact, it was later found experimentally that nucleation of second phase (Ni_3Nb) took a minimum of 48 hours to occur at each precipitation temperature of 1200°C, 1150°C, and 1100°C. Therefore, water quenching the samples from 1280°C to room temperature allowed single phase microstructures for both Ni-12%Nb and Ni-16%Nb. Thus, the η can be calculated using the following equation:

$$\eta = \frac{a_{0.16} - a_{0.12}}{a_{0.12}} \frac{1}{C_{0.16} - C_{0.12}}. \qquad [21]$$

A siemens x-ray diffractometer was used to determine the lattice parameters ($a_{0.12}$, $a_{0.16}$) of the Ni-12%Nb and Ni-16%Nb samples. These homogenized and quenched samples were polished to obtain a flat surface prior to being loaded on the diffractometer. The following conditions were used for the diffraction scan:

Scan Range (2θ): 20°-100°

Scan Step: 0.05°

Dwell Time: 2 seconds

The 2θ positions for the 5 most intense peaks were obtained. To determine the d-spacing for each reflection, Bragg's law was used

$$\lambda = 2d\sin\theta, \qquad [22]$$

where λ is the wavelength of Cu $K_{\alpha 1}$. The lattice parameter for each reflection was calculated using the following equation

$$1/d^2 = 1/d^2\ (h^2+k^2+l^2) \qquad [23]$$

Lattice parameters for each reflection were determined and plotted versus the Nelson-Riley function

$$N\text{-}R = \frac{1}{2}\left(\frac{\cos}{\sin\theta} + \frac{\cos}{\theta}\right). \qquad [24]$$

and extrapolated back to 2θ=180° (N-R=0) to give the lattice parameter for this sample.

Prior to running the samples, pure (99.99 pct) nickel polished to 1 μm diamond was run with the same conditions as

to verify the systematic error. The results from pure Ni shown in Table IV, and the indexed x-ray is shown in ure 9.

Table IV. Results of Lattice Parameter Determination of ure Nickel at Room Temperature Using X-ray Diffraction

h	l	2θ(°)	d(Å)	N-R	a(Å)
1	1	44.592	2.0304	1.1474	3.5162
2	0	51.921	1.7597	0.9388	3.5193
2	0	76.454	1.2449	0.5067	3.5214
3	1	92.948	1.0624	0.3321	3.5231

A plot of lattice parameter versus Nelson-Riley function shown in Figure 10. The extrapolated lattice parameter is .5234 Å, which is 0.05 pct greater than the theoretical value 3.5236 Å (37). This systematic error can be ignored, pecially when the major concern is the ratio of $(a_{0.16} - a_{0.12})$ er $a_{0.16}$, as shown in Eq. [21].

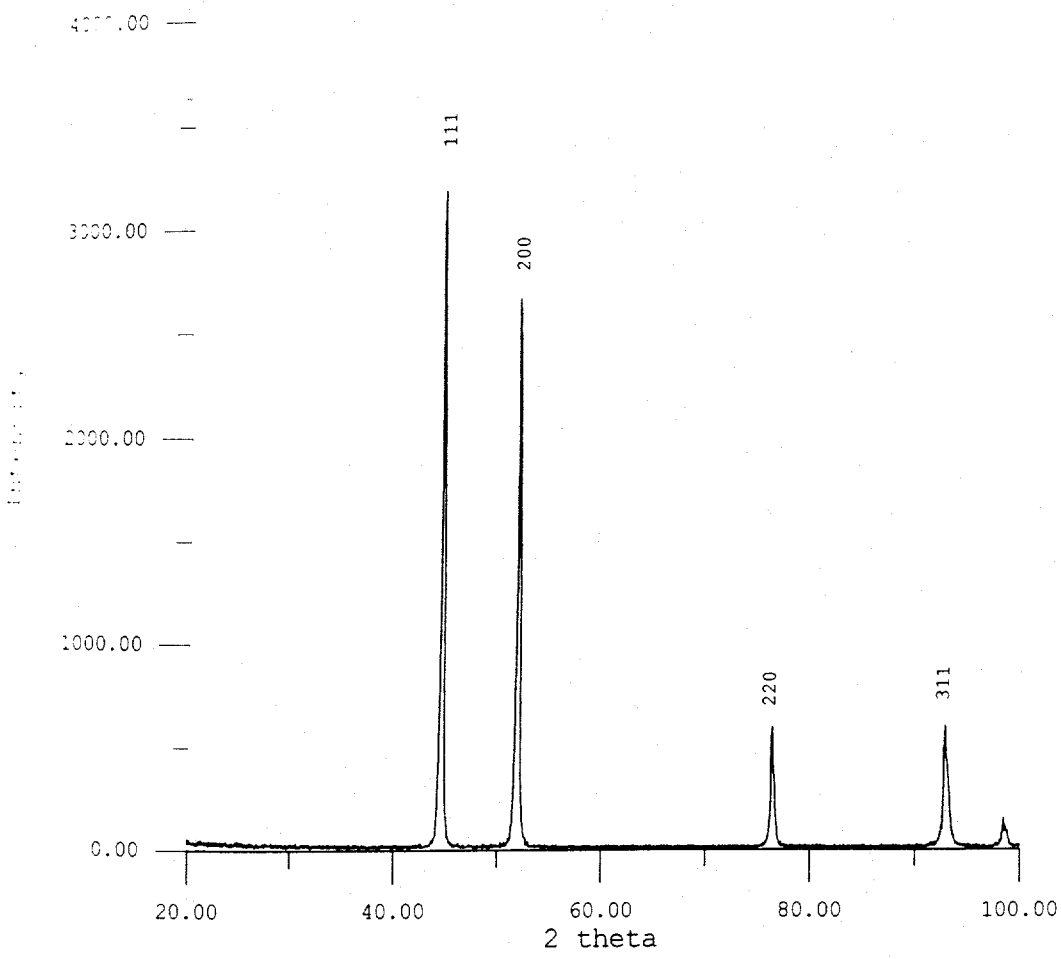

3.9--X-ray diffraction of pure nickel at room temperature.

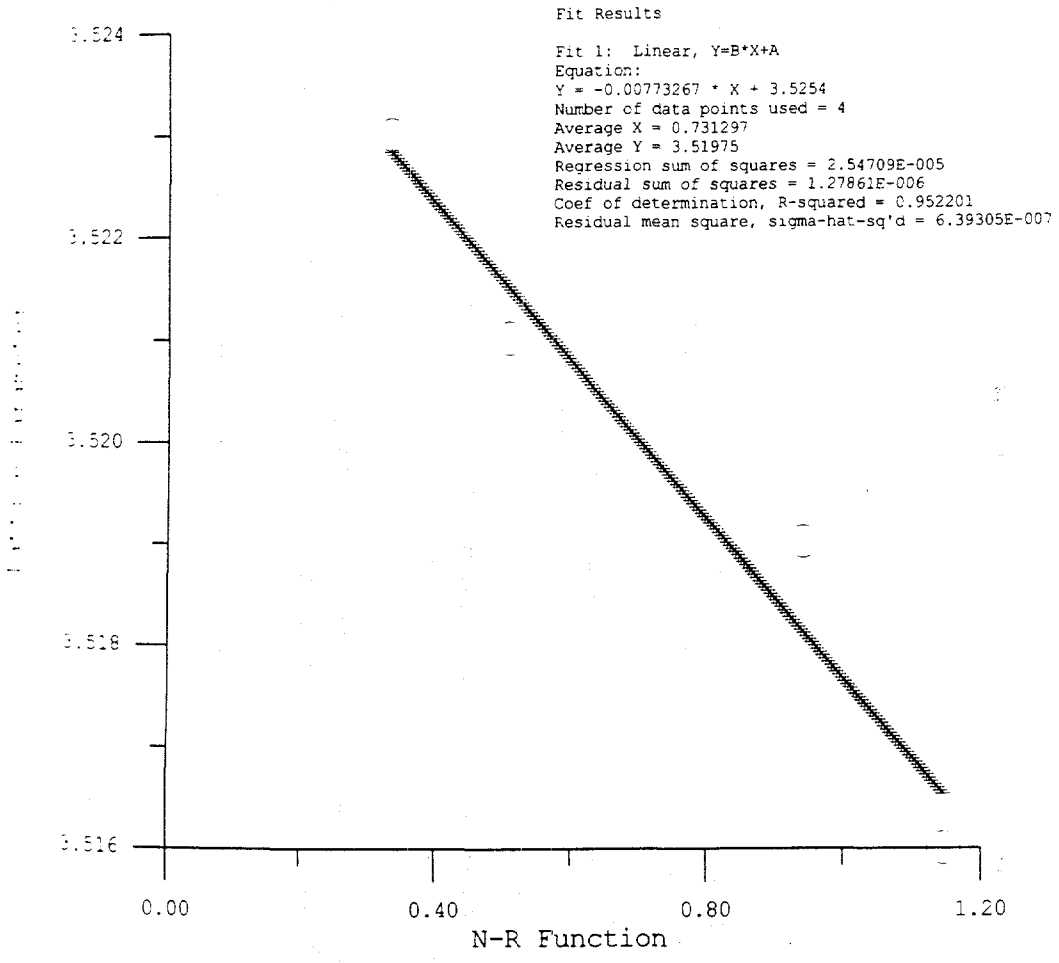

Fig. 10--Lattice parameter vs. Nelson-Riley function.

CHAPTER 3.

RESULTS

Test of Coherency Strain Hypothesis for CLFM in Alloy 718

Section 1 of part B in chapter 1 was devoted to the discussion of coherency strain hypothesis for CLFM in alloy 718. It was concluded that if the coherency strain hypothesis is for CLFM, the modified Hillert model predicts that in stage III of liquation, the migration velocity will increase, reach a maximum, and then decline and approach zero quickly during an isothermal hold. It should be noted that due to the special interest in stage III of constitutional liquation, the experimental work in this study is concentrated on the stage III behavior. The following results are presented in a sequence which explores the possible correlation between the migration behavior predicted by the modified Hillert model and that observed experimentally.

1. *CLFM in alloy 718*

A plot of migration distance versus isothermal hold for CLFM at the peak temperature of 1227°C is shown in Figure 11 (a). Rearrangmemt of this plot by showing migration velocity versus isothermal hold is shown in Figure 12. In Figure 12, the migration velocity for each isothermal hold is

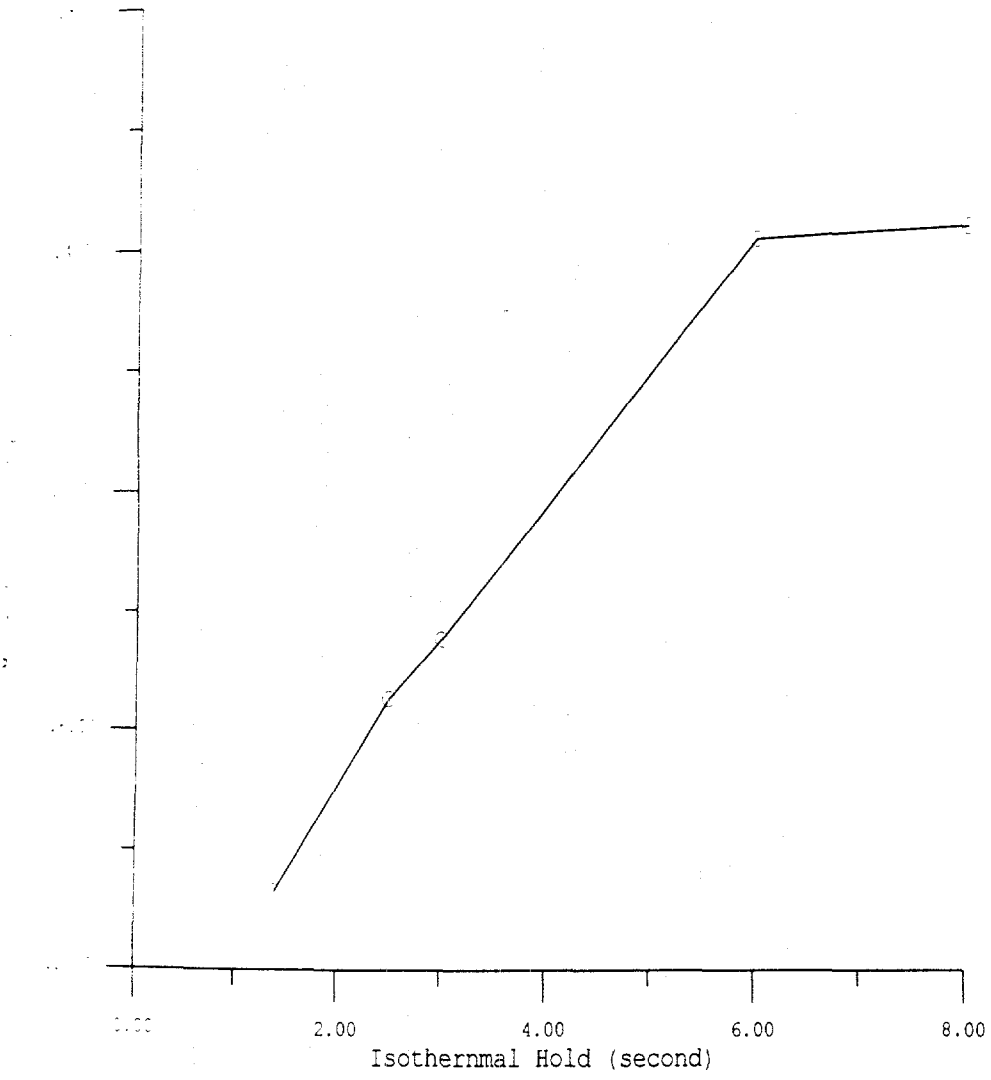

11--Average migration distance as a function of thermal holding time in alloy 718 at an isothermal holding temperature of 1227°C. The migration distance increases with time, showing that migration occurs in the presence of liquid [illegible].

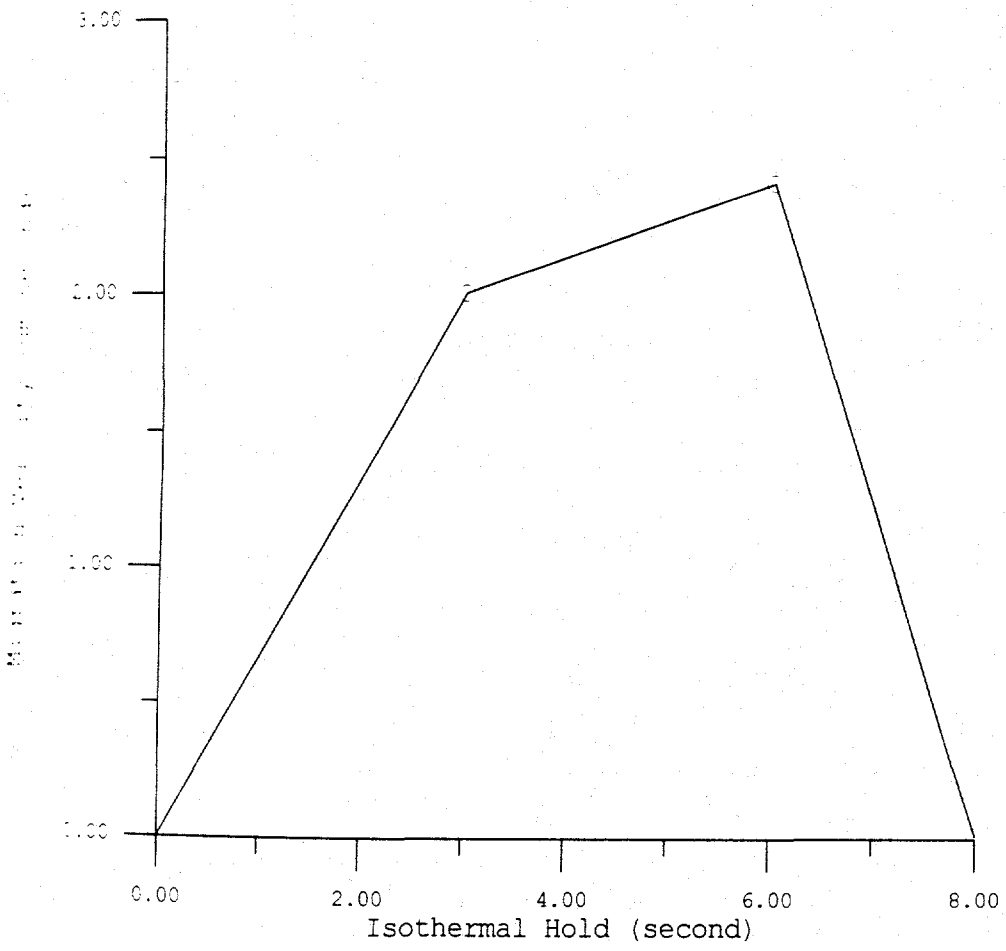

12--Average migration velocity as a function of thermal holding time approximated from Figure 11.

approximated from Figure 11 by obtaining the ratio of $\Delta d/\Delta t$ (i.e., the incremental increase in migration distance over incremental increase in time period).

The present study is intended to obtain a more accurate relationship between migration velocity versus isothermal holding time than was attempted in previous works (27,33). Specifically, it was intended to measure CLFM migration velocity using the Cahn-Hagel equation for isothermal holding time varying from 1 second to 10 seconds at the peak temperature of 1227°C. However, it was found from the microstructure (Figure 13) that the actual temperature was about 1240°C, indicating that the Gleeble calibration was off. This conclusion was based on the comparison of microstructure of CLFM work in this study with other CLFM work done at various temperatures by others (27, 33). Specifically, the comparison of the extent of matrix liquation allowed a fairly close evaluation of the actual temperature (27,33). Hence, the obtained microstructure was considered to be at about 1240°C, instead of the intended temperature of 1227°C.

Figure 13 shows the microstructure of alloy 718 after various isothermal holds at the peak temperature 1240°C. The reversed curvature (i.e., the zigzag motion back and forth across the original grain boundary) is characteristic of LFM and CLFM.

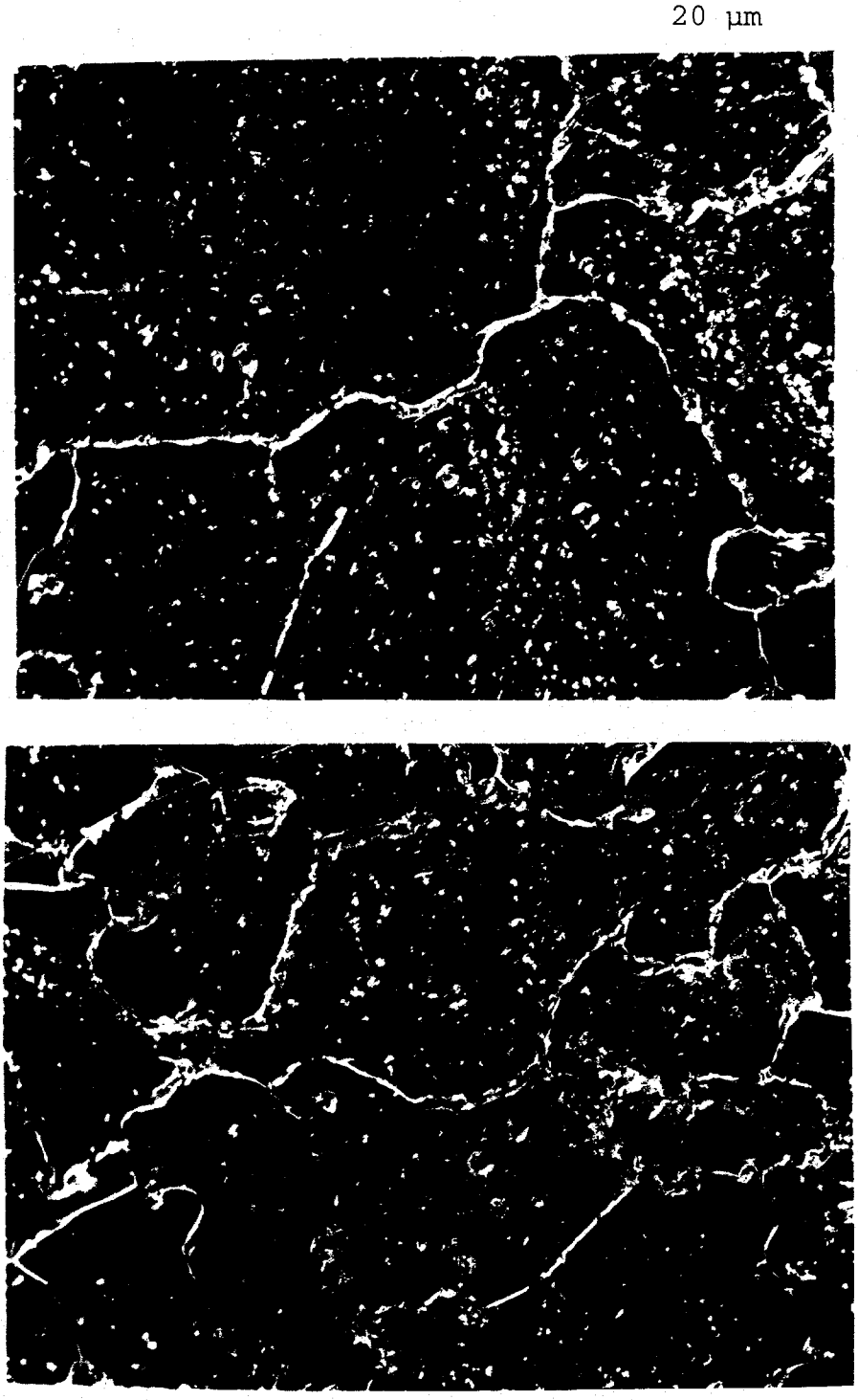

Fig. 13--Light micrographs of 1240°C peak temperature samples showing CLFM after isothermal hold for (a) 2 seconds, (b) 3 seconds, (c) 5 seconds, (d) 7 seconds, (e) 10 seconds, and (f) 30 seconds.

20 μm

c)

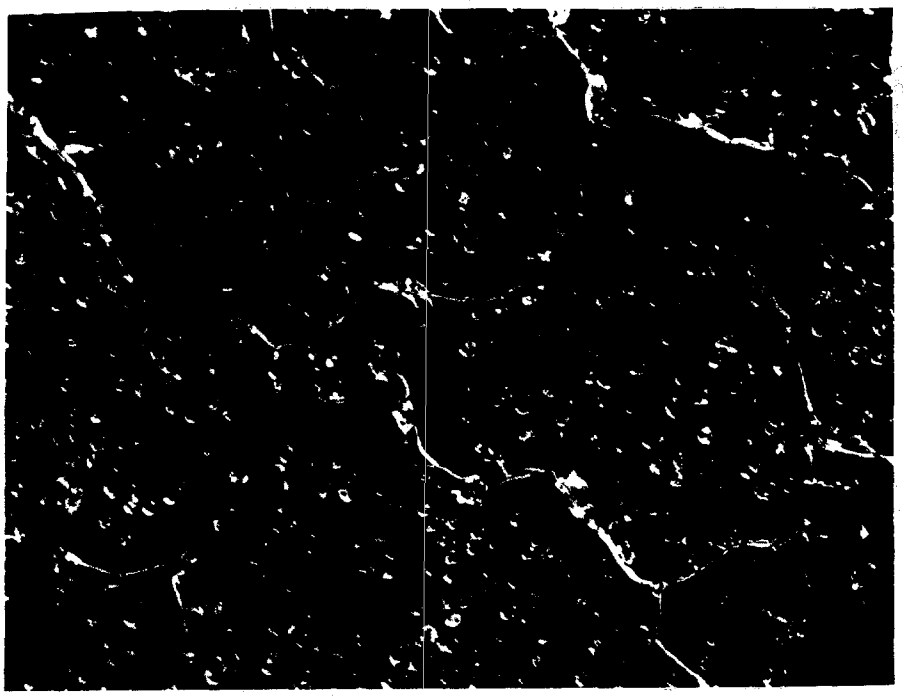

(d)

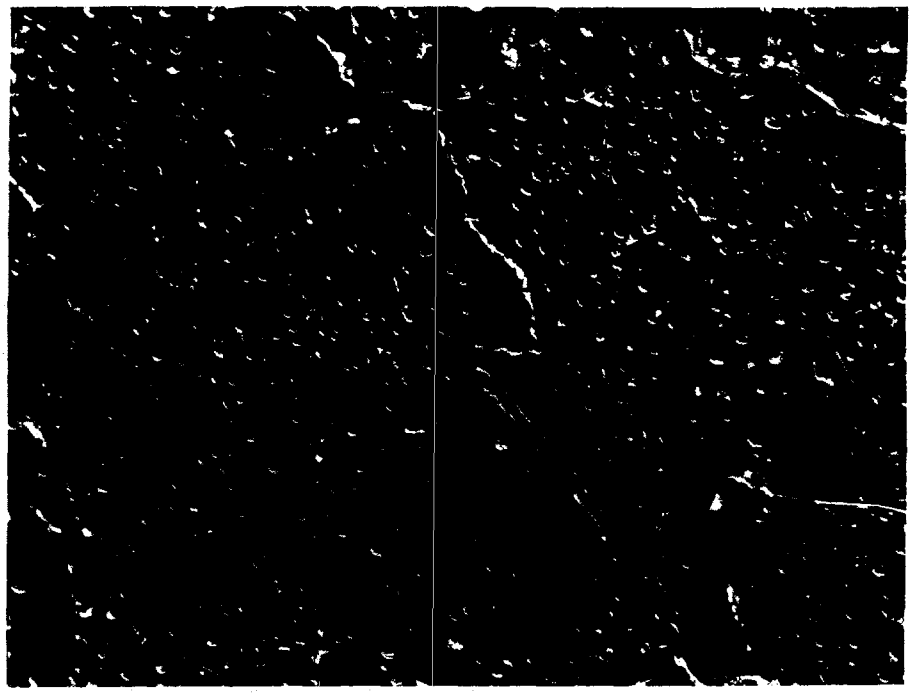

Fig. 13--(Continued).

20 μm

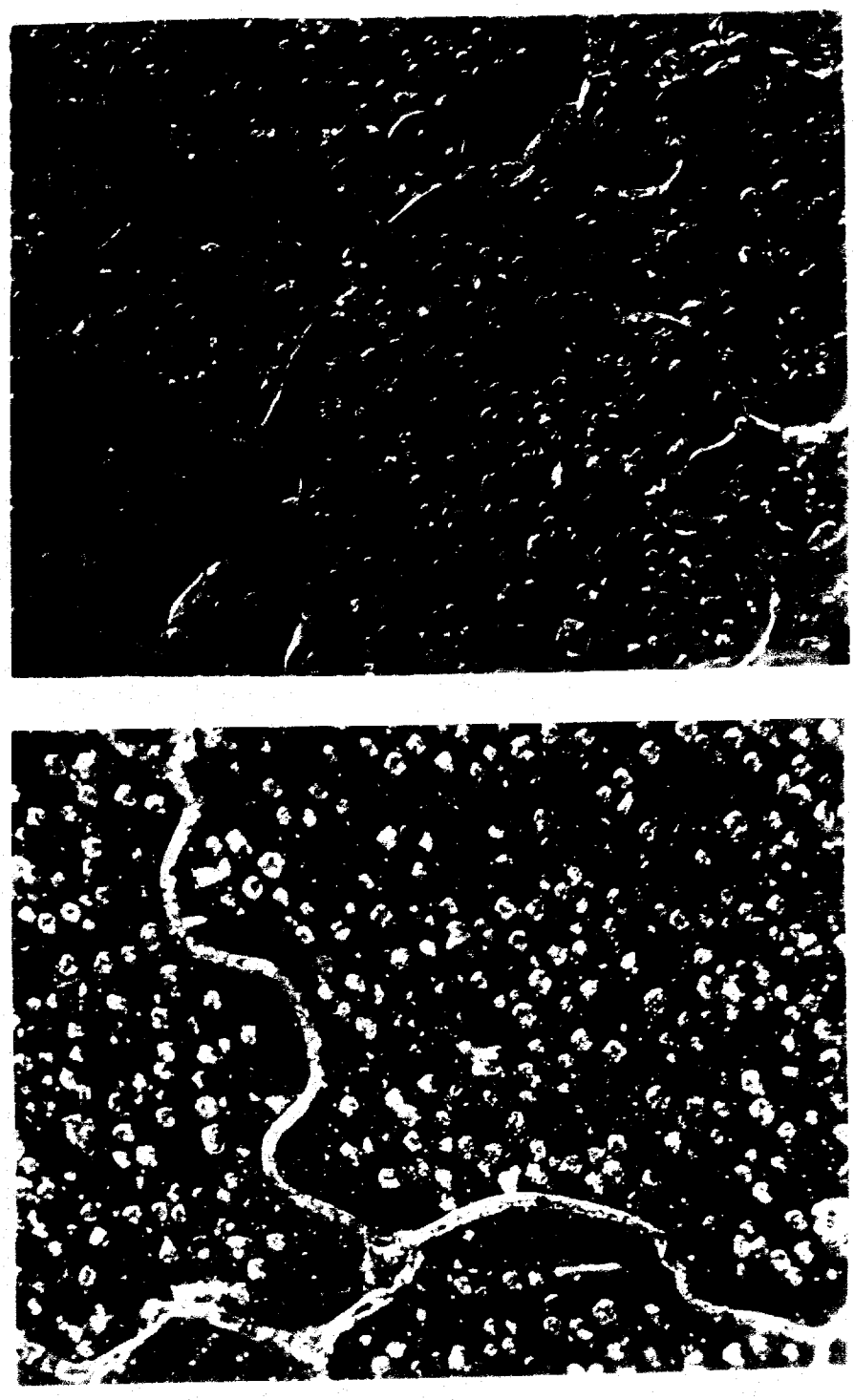

Fig. 13--(Continued).

2. *Migration velocity measurement*

The plot of migration velocity versus isothermal hold is shown in Figure 14. At a peak temperature of 1240°C, the migration velocity was observed to increase, reach a peak velocity in the 6th second of the isothermal hold, and quickly decline to zero at the 7th second of isothermal hold.

B. *Test of Coherency Strain Hypothesis of LFM for CLFM in Ni-16%Nb Binary Alloy*

The purpose of using a binary alloy exhibiting CLFM is to investigate whether Handwerker's model holds for CLFM (i.e., whether the migration velocity varies systematically with the coherency lattice strain).

1. *CLFM in Ni-16%Nb alloy*

a. *Microstructure*

The cast microstructure of Ni-16%Nb is shown in Figure 15. Figure 16 shows the microstructure after homogenization heat treatment at 1290°C for 24 hours, followed by a precipitation heat treatment for another 72 hours at different temperatures of 1150°C, 1100°C, and 1050°C. According to the phase diagram (Figure 6), the volume fractions of the second phase (Ni_3Nb) at these precipitation temperatures are around 5 pct, 10 pct and 14 pct, respectively. These predictions were experimentally verified.

Figure 17 shows CLFM of the samples precipitated at 1150°C for 72 hours and followed by isothermal holds of 1, 3, 5, 7, and 9 seconds at a peak temperature of 1300°C. Figures

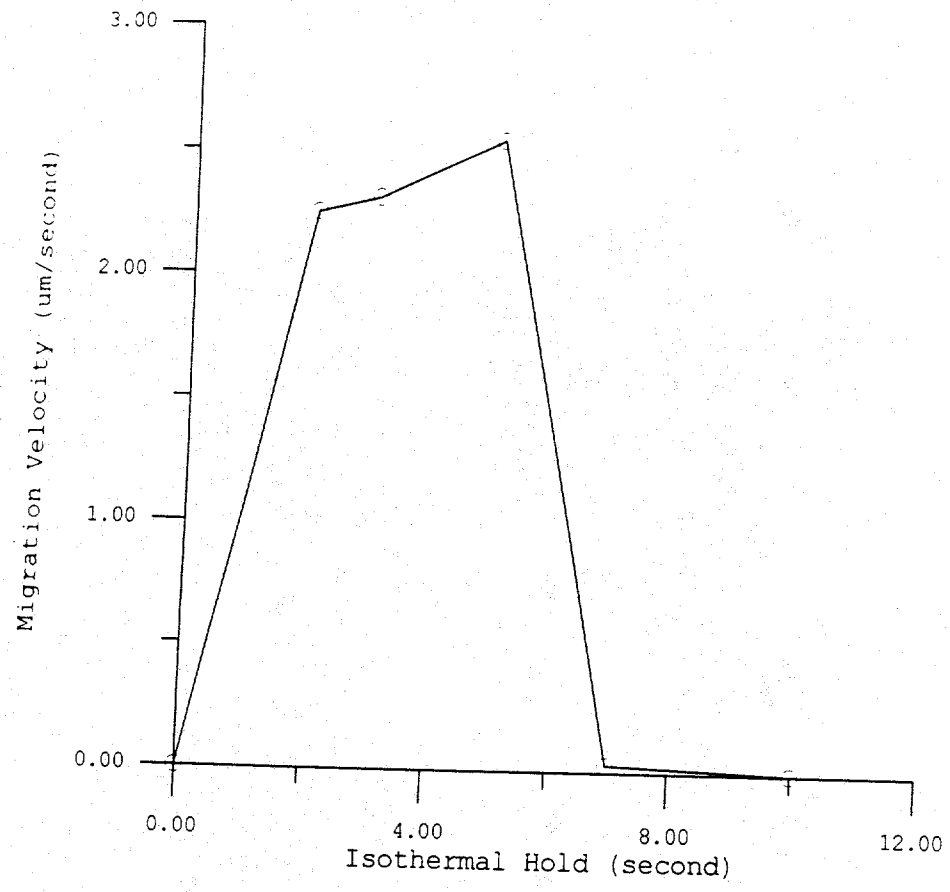

Fig. 14--Migration velocity vs. isothermal holding time for CLFM of alloy 718 held at a peak temperature of 1240°C. The data represent a 90 pct confidence interval.

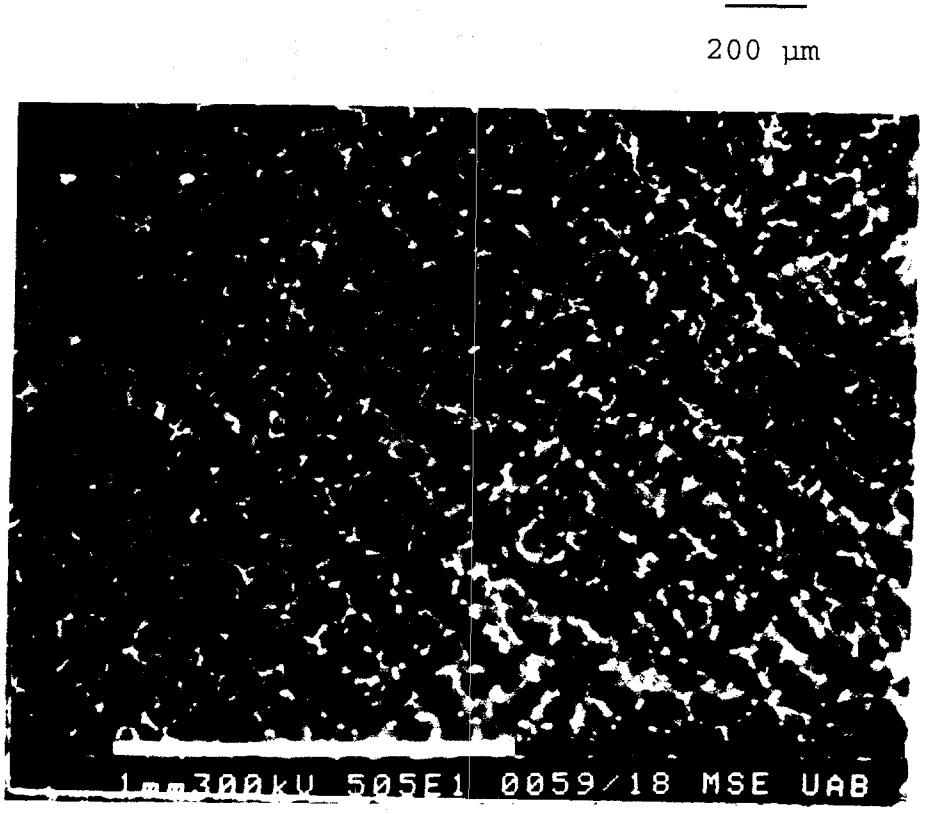

Fig. 15--The cast microstructure of Ni-16%Nb alloy.

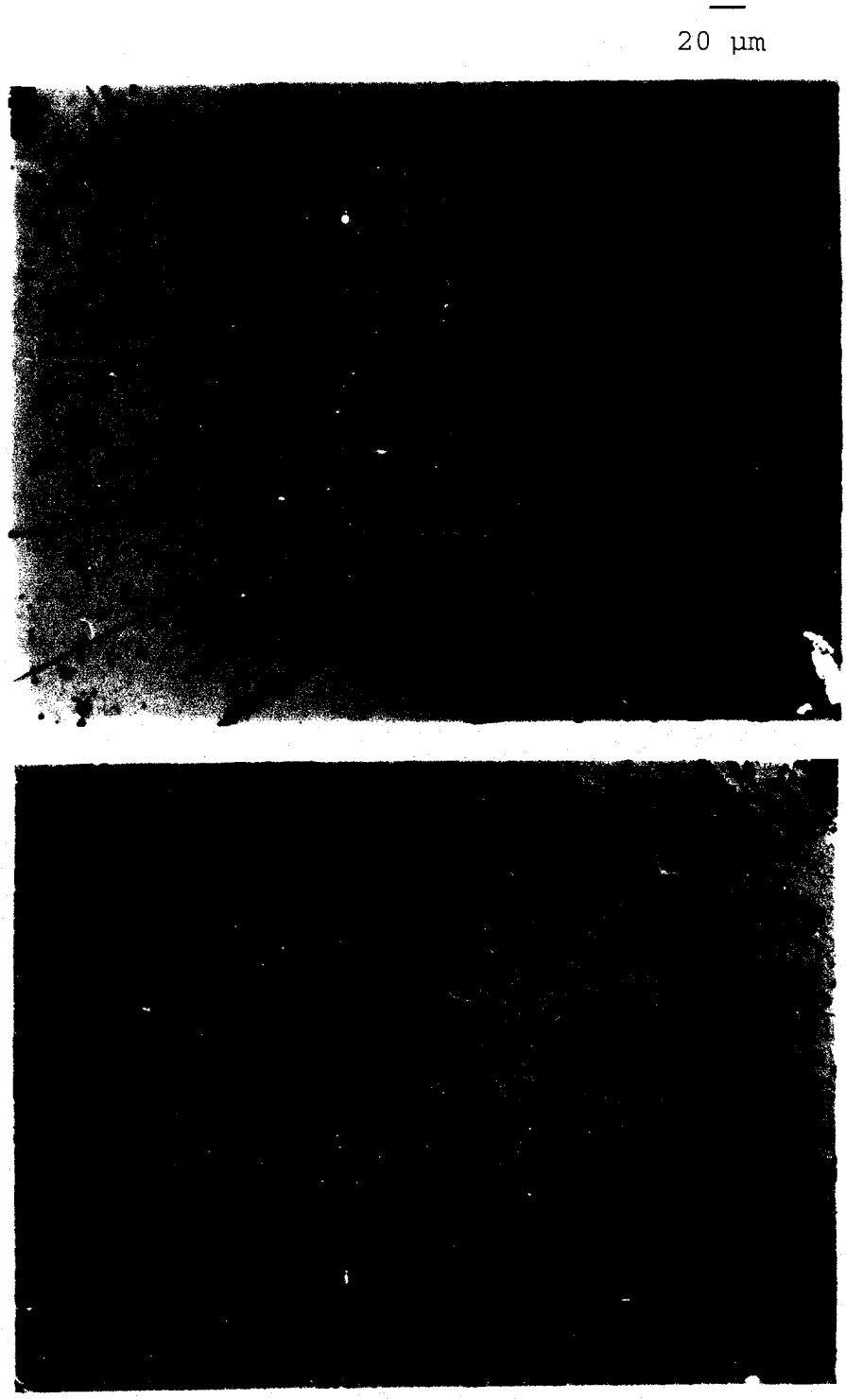

Fig. 16--The microstructure of Ni-16%Nb that was homogenized at 1290°C for 24 hours, followed by a precipitation heat treatment for another 72 hours at different temperatures of (a) 1150°C (b) 1100°C and (c) 1050°C.

20 μm

(c)

Fig. 16--(Continued).

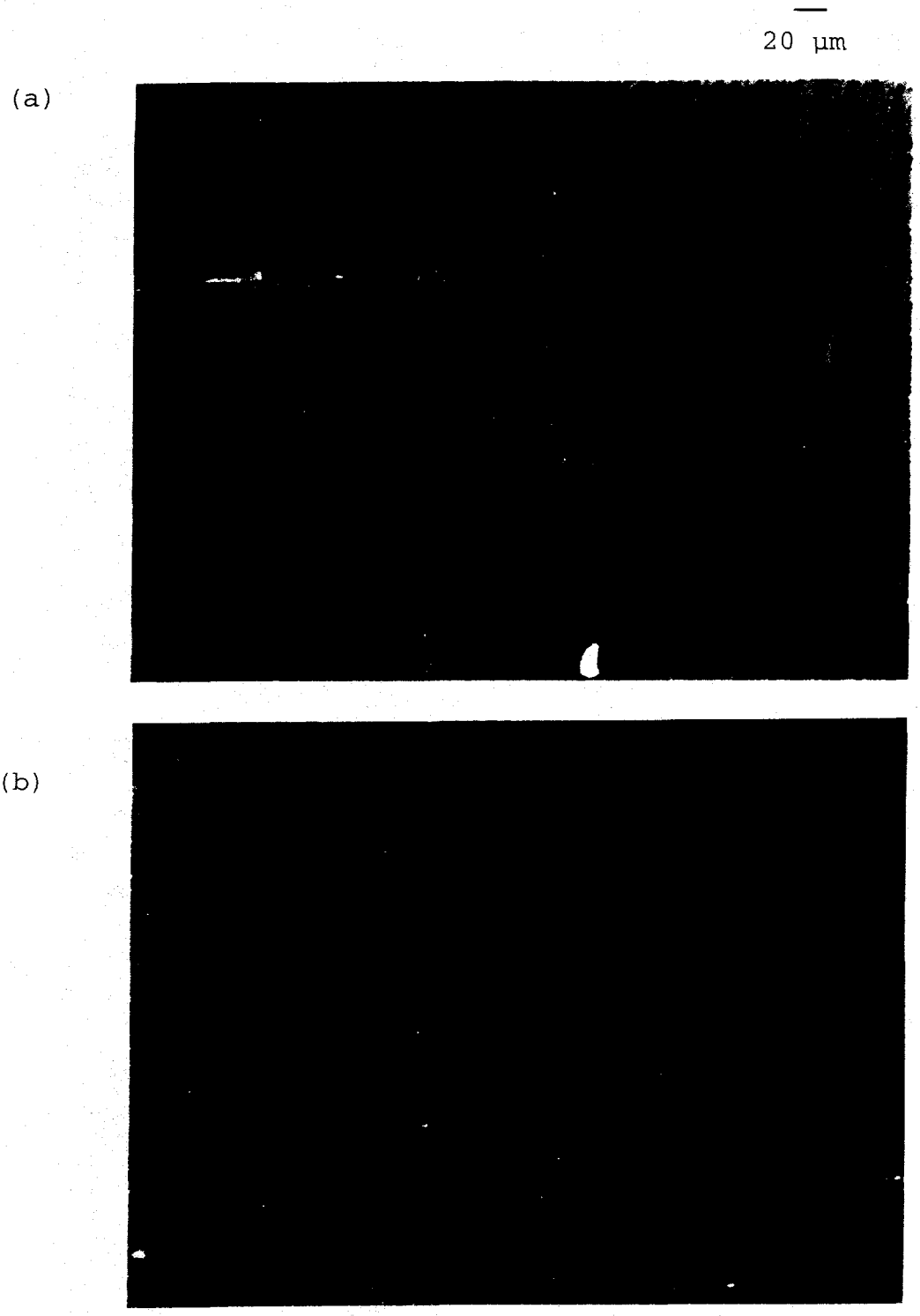

Fig. 17--Light micrograph showing CLFM of Ni-16%Nb samples that were homogenized at 1290°C for 24 hours, followed by a precipitation heat treatment for another 72 hours at 1150°C, and held at a peak temperature of 1300°C for (a) 1 second (b) 3 seconds (c) 5 seconds (d) 7 seconds and (e) 9 seconds.

20 μm

(c)

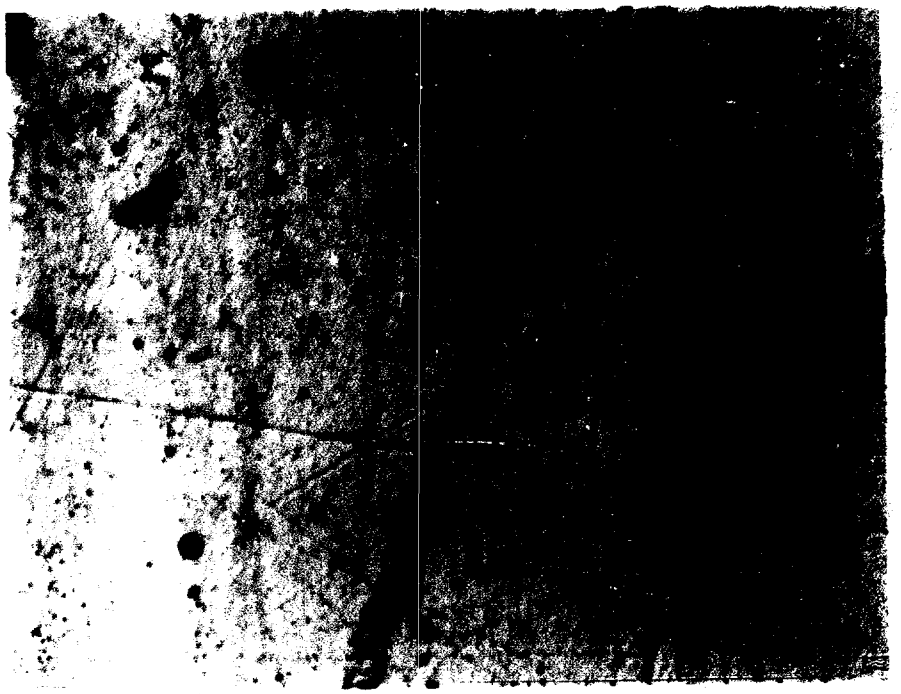

(d)

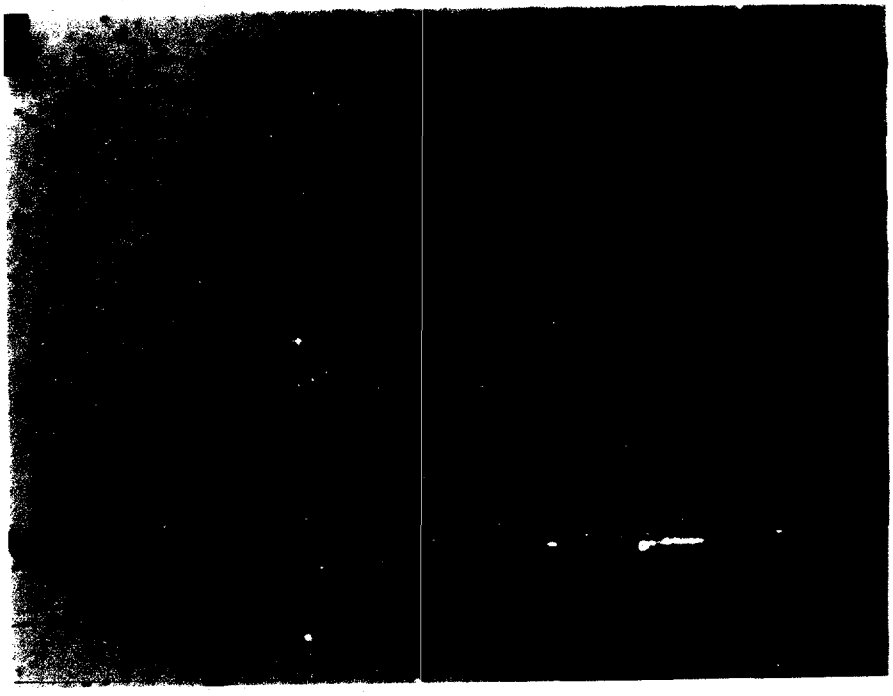

Fig. 17--(Continued).

20 μm

(e)

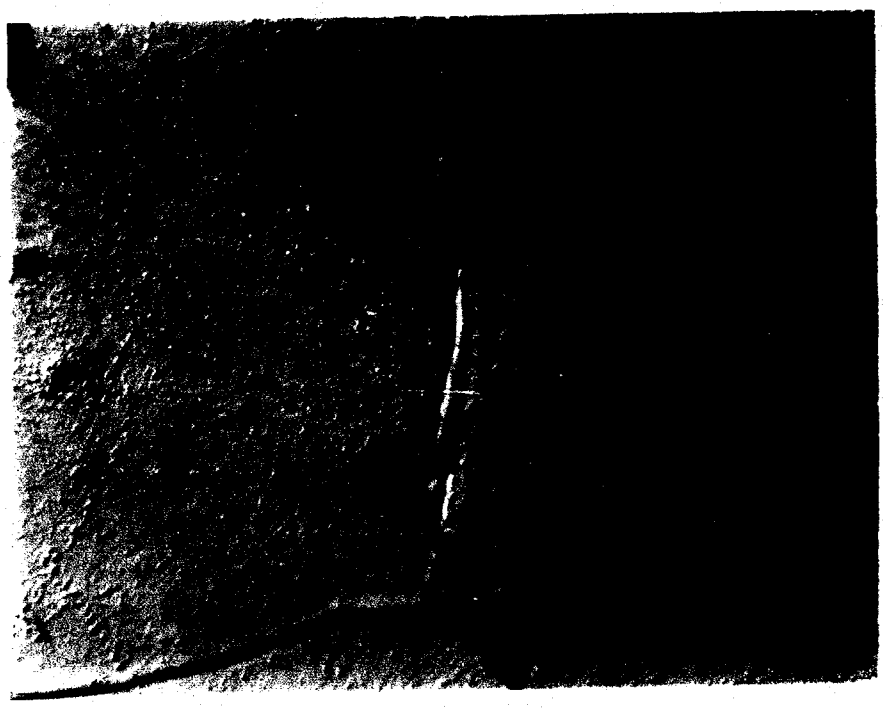

Fig. 17--(Continued).

18 and 19 show similar results for samples precipitated at 1100°C and 1050°C respectively.

b. *Analysis of composition and precipitate volume fraction*

The weight loss during melting was found to be less than 0.2 pct; hence, the average alloy composition was assumed to be the intended Ni-16%Nb in weight percentage. This assumption was confirmed by the quantitative EDS analysis on a sample that was solutionized at 1275°C for 24 hours, followed by water quenching. One representative EDS spectrum collected from this sample is shown in Figure 20, and the spectra of pure Ni and Nb that were used as quantitative standards are shown in Figure 21. The result of the quantitative EDS analysis is shown in Table V.

According to the phase diagram, the matrix compositions of samples precipitated at 1150°C, 1100°C, and 1050°C are 15 pct, 14 pct, and 13 pct, respectively. Since the differences in matrix composition among these samples are small, it was not intended to use quantitative EDS analysis to distinguish the compositional difference among these samples with great accuracy. It was noted from the phase diagram that the Ni_3Nb precipitate volume fraction was significantly different, even for 1 pct composition variations from 15 pct to 14 pct, or from 14 pct to 13 pct. Hence, a quantitative measurement of Ni_3Nb precipitate volume fraction was done on samples precipitation heat treated at temperatures of 1150°C, 1100°C,

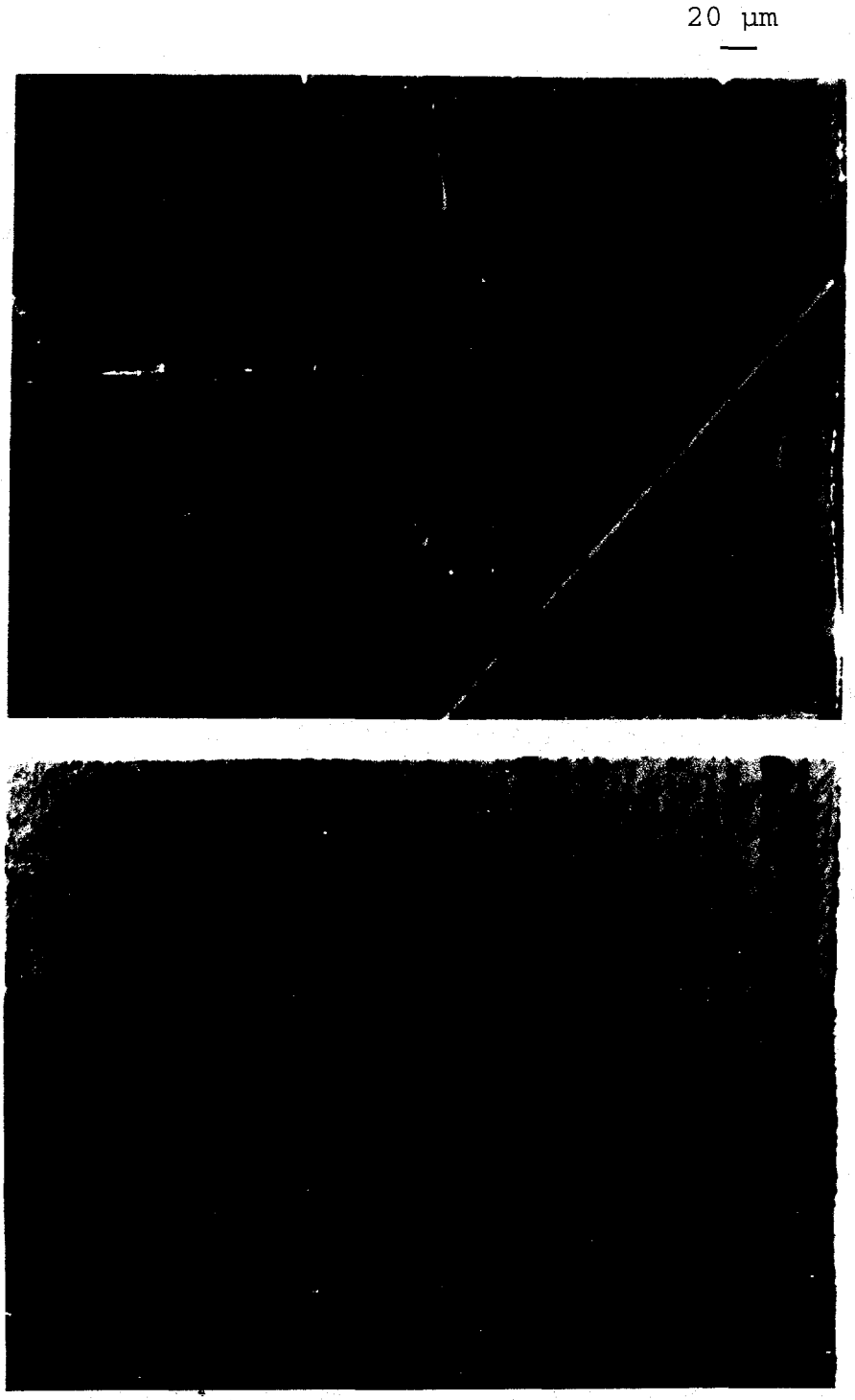

Fig. 18--Light micrograph showing CLFM of Ni-16%Nb samples that were homogenized at 1290°C for 24 hours, followed by a precipitation heat treatment for another 72 hours at 1100°C, and held at a peak temperature of 1300°C for (a)1 second (b) 3 seconds (c) 5 seconds and (d) 7 seconds.

20 μm

(c)

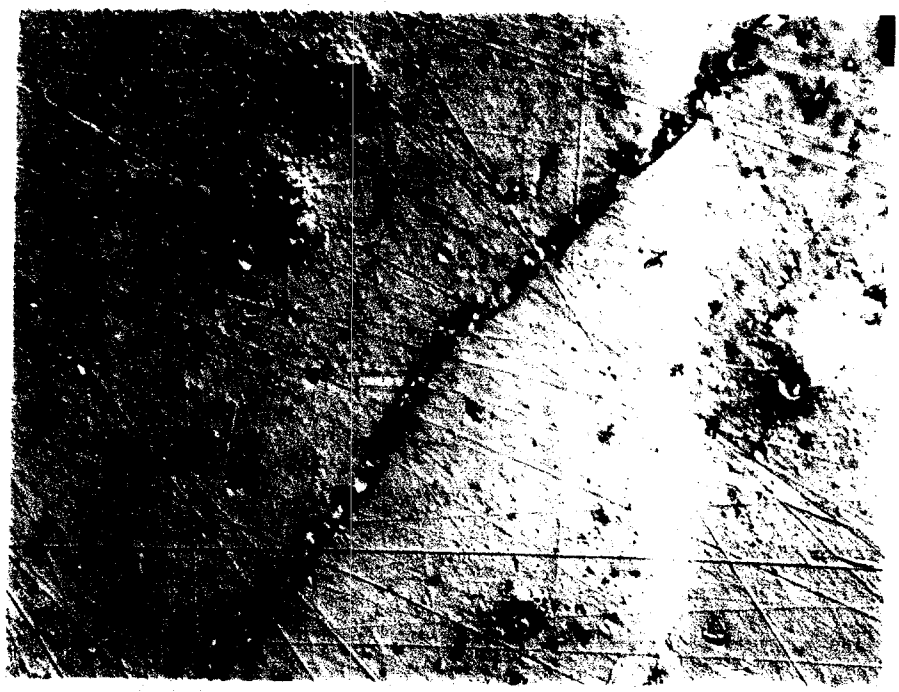

(d)

Fig. 18--(Continued).

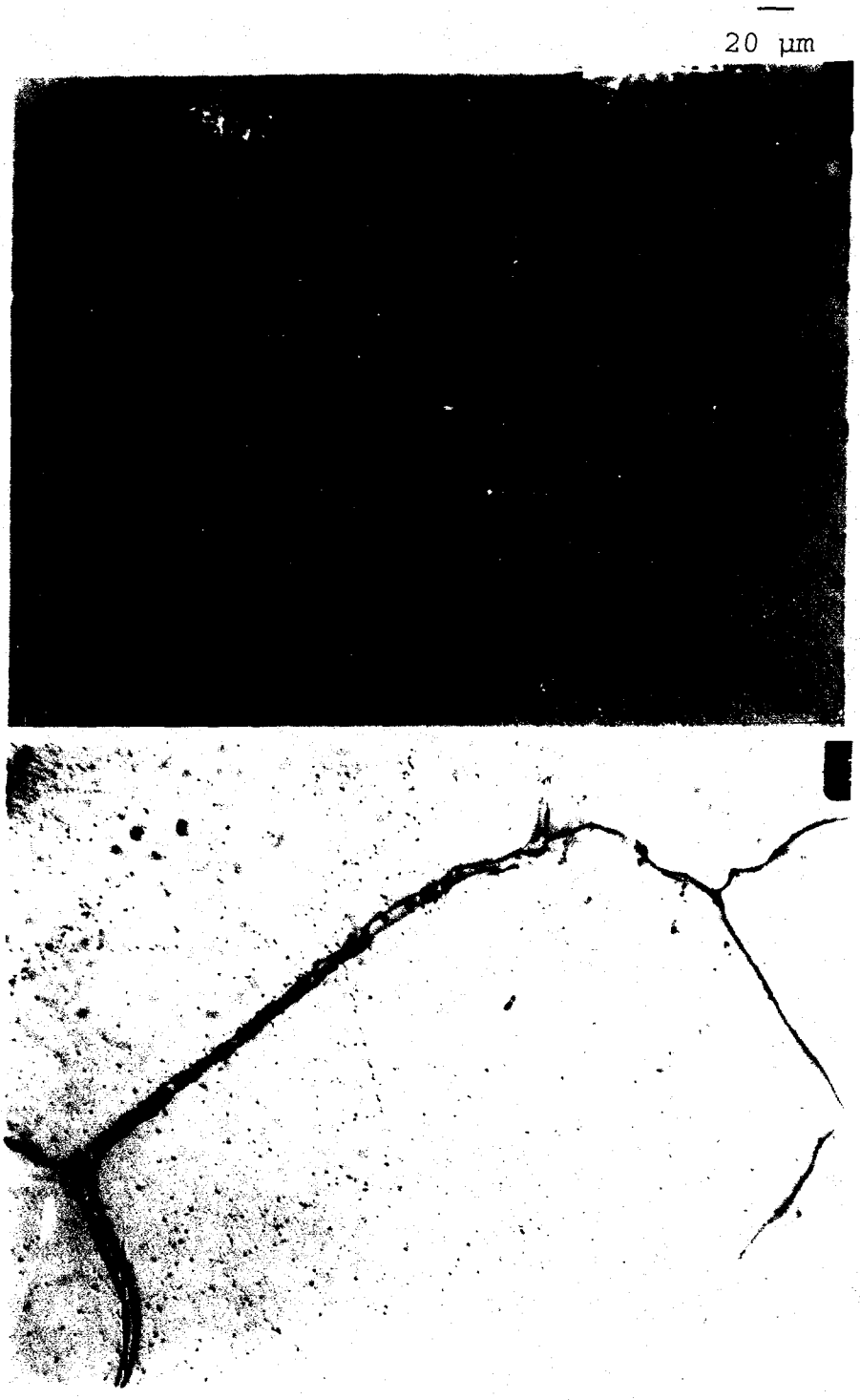

Fig. 19--Light micrograph showing CLFM of Ni-16%Nb samples that were homogenized at 1290°C for 24 hours, followed by a precipitation heat treatment for another 72 hours at 1050°C, and held at a peak temperature of 1300°C for (a) 1 second (b) 3 seconds (c) 5 seconds (d) 7 seconds and (e) 9 seconds.

20 μm

(c)

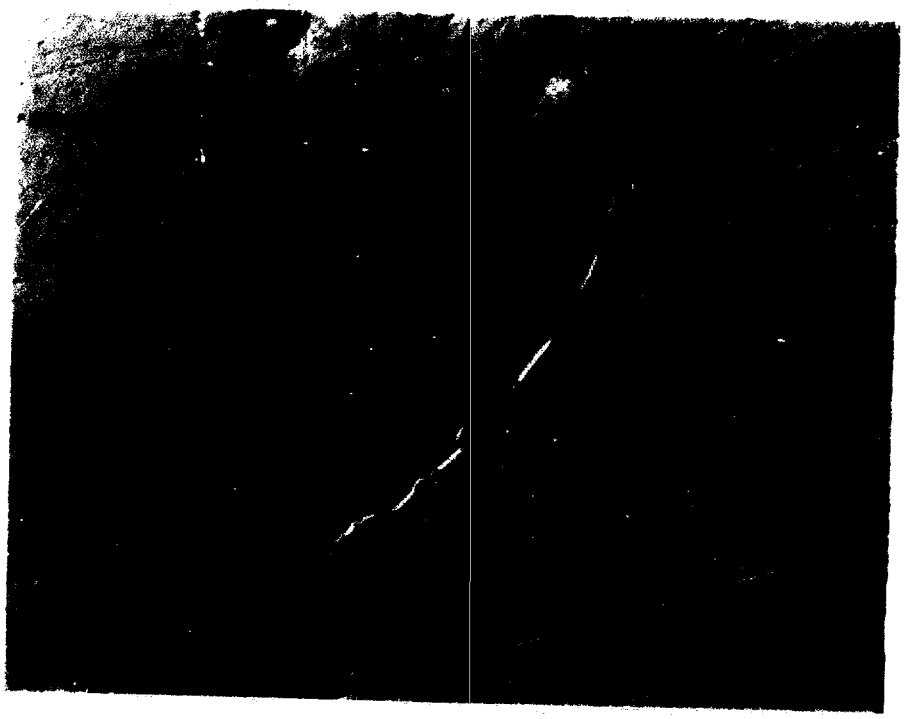

(d)

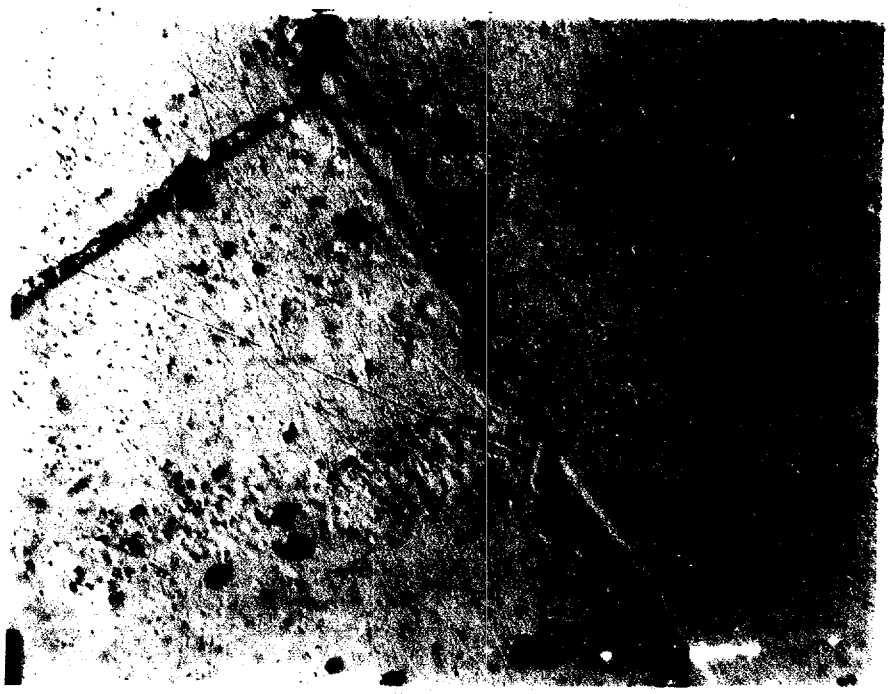

Fig. 19--(Continued).

20 μm

(e)

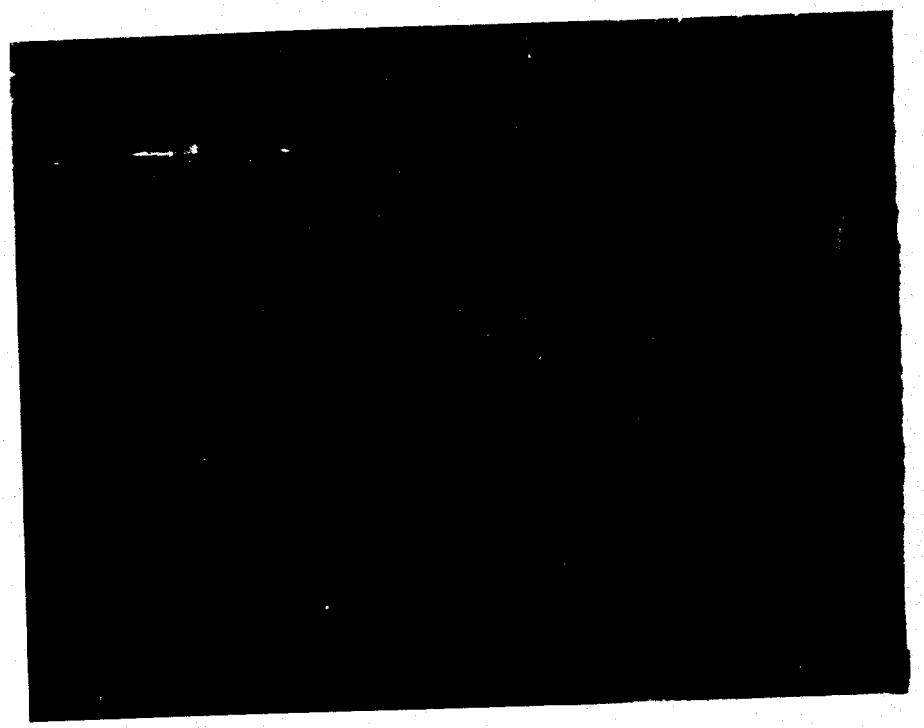

Fig. 19--(Continued).

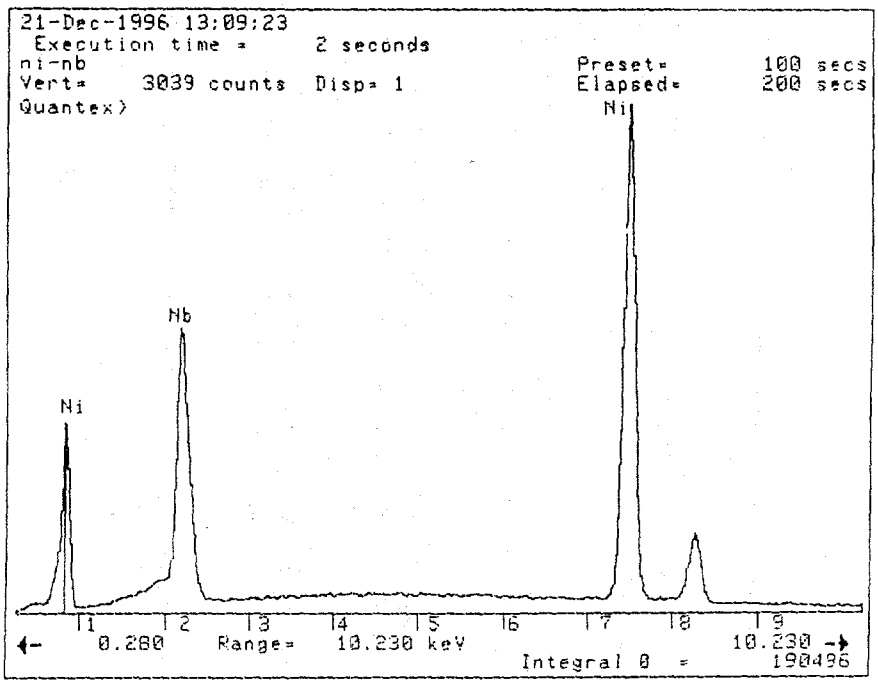

Fig. 20--Representative EDS spectra of Ni-16%Nb that was solutionized at 1280°C for 24 hours, followed by water quenching.

(a)

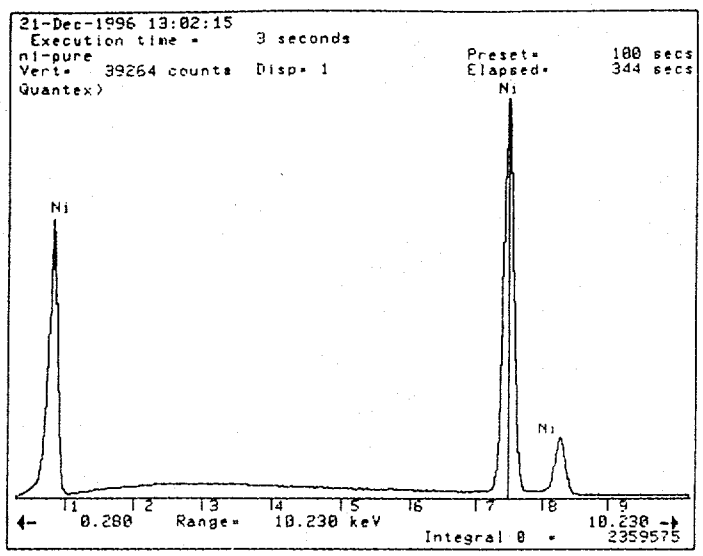

(b)

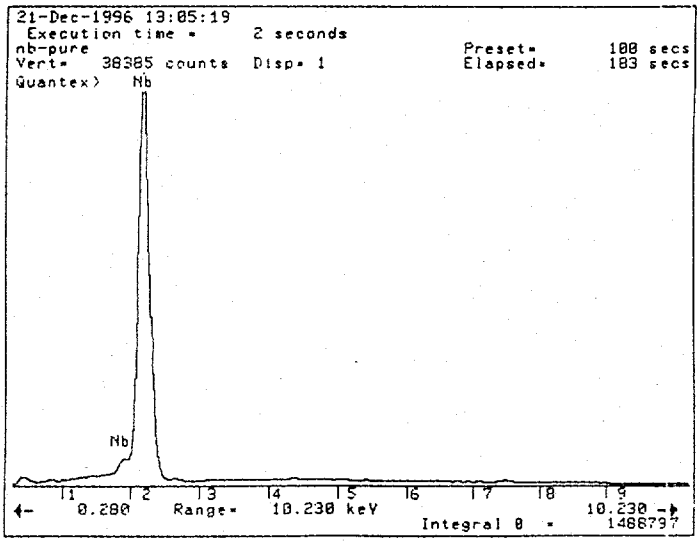

Fig. 21--EDS spectra of (a) pure Ni and (b) pure Nb that were used as quantitative standards.

Table V. Quantitative EDS Analysis Using Standards

	Ni	Nb
Intended Composition	84%	16%
Measured Composition	83.6% (83.2-83.9)	15.8% (15.6-16.1)

* The values reported represent the mean for five different locations. The range is given within parentheses.

and 1050°C as an aided approach to identify whether the matrix compositions were following the phase diagram data reasonably closely. Table VI shows the measured Ni_3Nb precipitate volume fraction ard that calculated from the phase diagram using level rule.

Table VI. Measured and Calculated Ni_3Nb Volume Fraction

	Measured	Calculated
Precipitated at 1150°C (Intended composition 15%)	(6.1 ±0.33)%	5.5%
Precipitated at 1100°C (Intended composition 14%)	(9.8 ±0.42)%	10.2%
Precipitated at 1050°C (Intended composition 13%)	(14.8±0.37)%	14.5%

The results show the matrix compositions from different precipitation heat treatment are consistent with that obtained from the phase diagram. Hence, the composition data from the phase diagram were used for the strain calculation to be described in the next section.

c. *Strain calculation through x-ray diffraction*

The indexed x-ray scan for Ni-12%Nb alloy, which was homogenized at 1280°C for 24 hours, followed by water

quenching, is shown in Figure 22. The related results for the determination of lattice parameter are shown in Table VII.

Table VII. Lattice Parameter Determination of Ni-12%Nb at 1280°C Using X-ray Diffraction

h	k	l	2θ(°)	d(Å)	N-R	a(Å)
1	1	1	43.951	2.0594	1.1692	3.5668
2	0	0	51.116	1.7855	0.9591	3.5710
2	2	0	75.291	1.2612	0.5216	3.5672
3	1	1	91.552	1.0749	0.3447	3.5650

A plot of lattice parameter versus Nelson-Riley function is shown in Figure 23. The extrapolated lattice parameter is 3.5649Å.

Similarly, the indexed x-ray scan for Ni-16%Nb alloy, which was subjected to the same heat treatment, is shown in Figure 24. The related results for the determination of lattice parameter are shown in Table VIII.

Table VIII. Lattice Parameter Determination of Ni-16%Nb at 1280°C Using X-ray Diffraction

h	k	l	2θ(°)	d(Å)	N-R	a(Å)
1	1	1	44.461	2.0806	2.1602	3.6035
2	0	0	50.733	1.7981	1.1852	3.5962
2	2	0	74.625	1.2708	0.9690	3.5943
3	1	1	90.500	1.0846	0.9571	3.5972

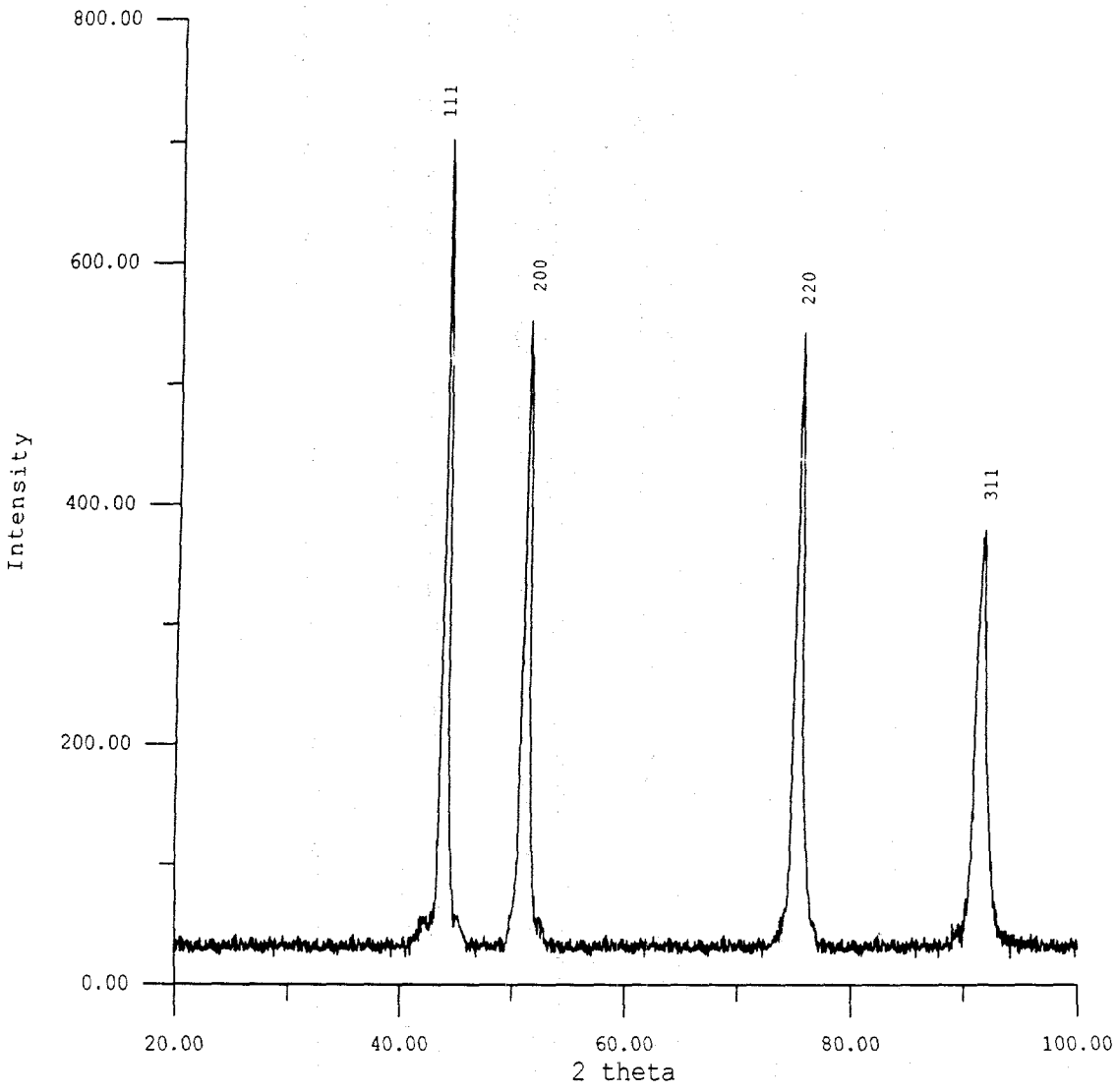

Fig. 22--X-ray diffraction scan of Ni-12%Nb alloy that was homogenized at 1280°C for 24 hours, followed by water quenching.

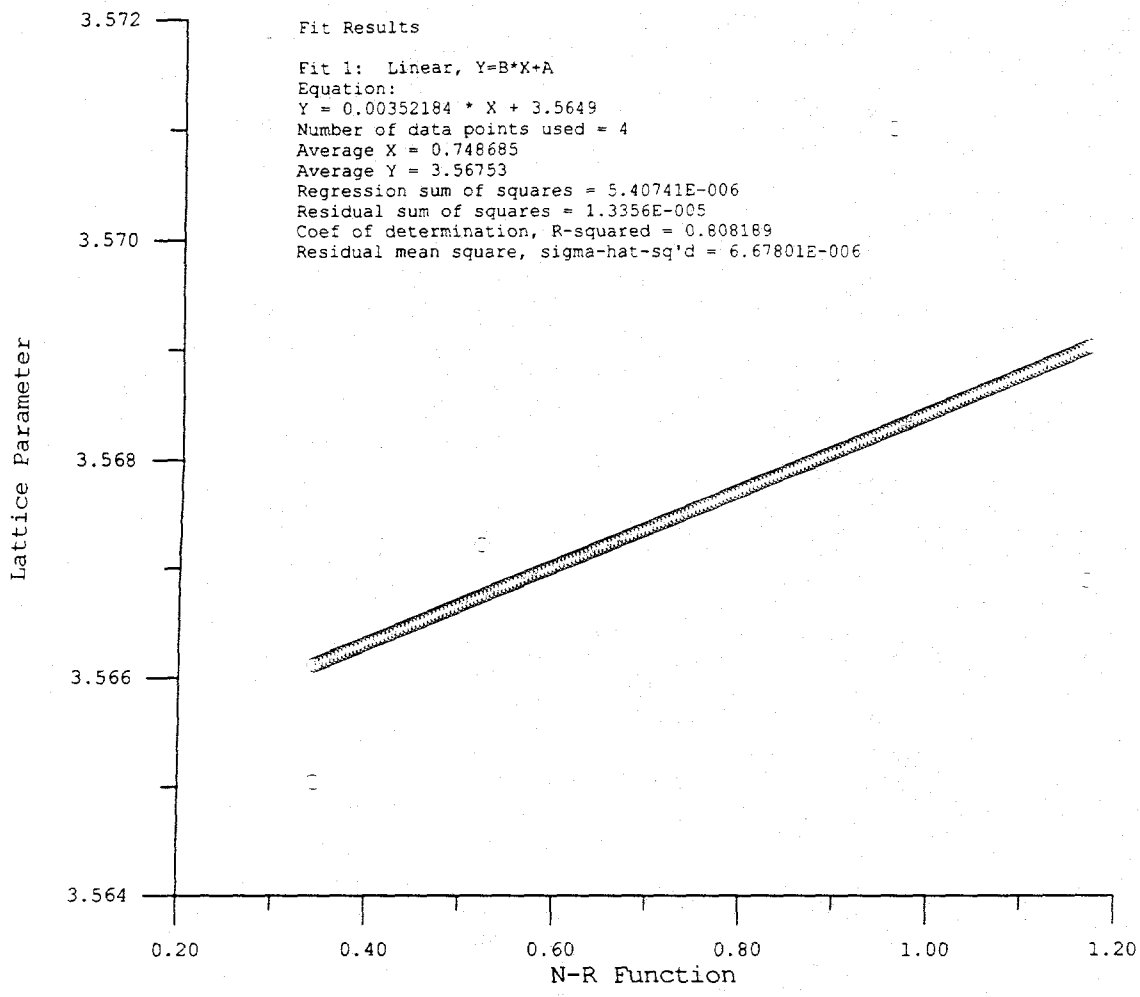

Fig. 23--Lattice parameter vs. N-R function for Ni-12%Nb alloy. The extrapolated lattice parameter is 3.5649Å.

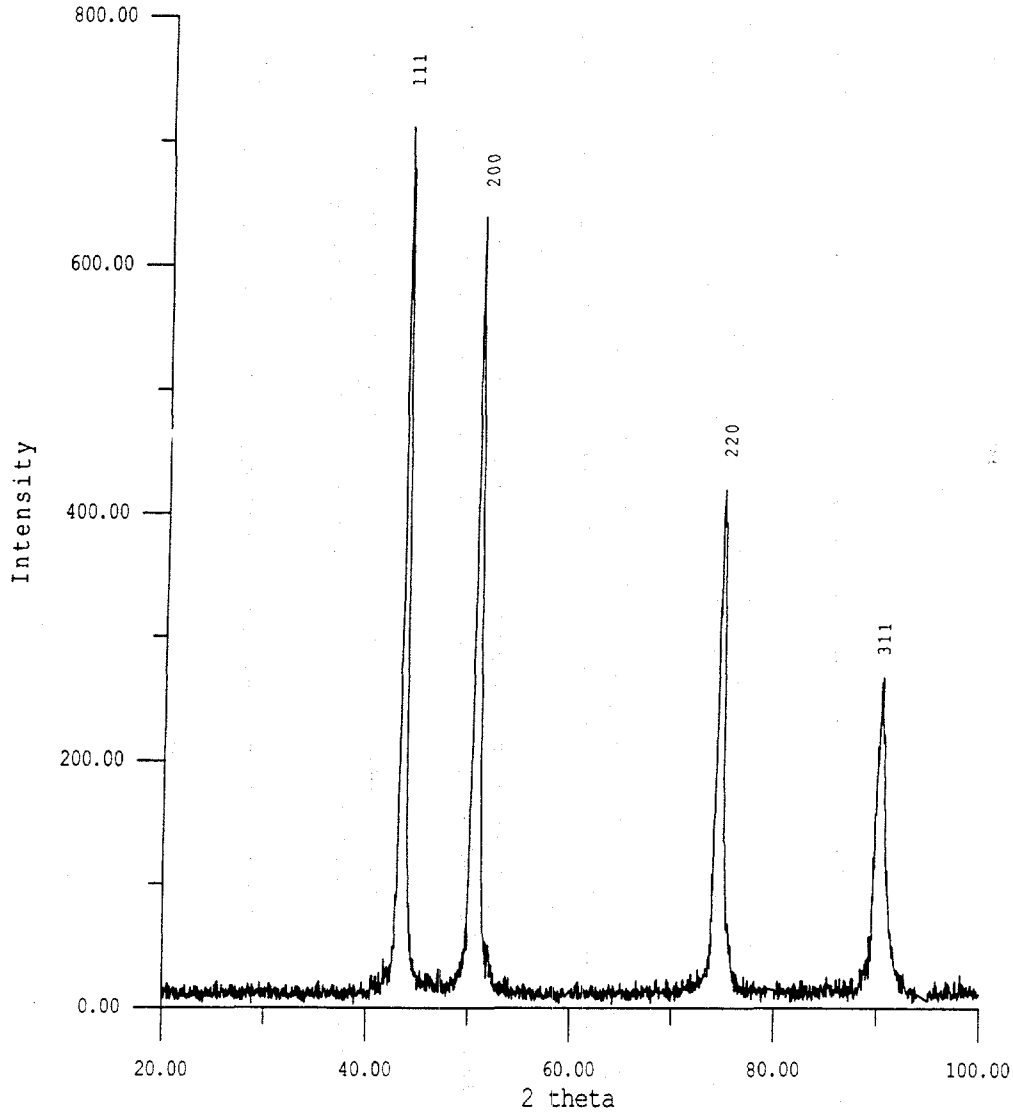

Fig. 24--X-ray diffraction scan of Ni-16%Nb alloy that was homogenized at 1280°C for 24 hours, followed by water quenching.

A plot of lattice parameter versus Nelson-Riley function is shown in Figure 25. The extrapolated lattice parameter is 3.5891Å.

It can be seen from comparing Figure 9 with Figures 22 and 24 that there is no additional x-ray peak present in Figures 22 and 24, indicating that homogenizing at 1280°C for 24 hours had indeed obtained single phase microstructure for both Ni-12%Nb and Ni-16%Nb alloys. The position (2 theta) for each of the main reflections of pure Ni (Figure 8) shifted as Nb was added to form Ni-12%Nb (Figure 21) and Ni-16%Nb (Figure 23), respectively. The shift is seen to increase with increasing $h^2+k^2+l^2$ value in the sequence of 111, 200, 220, and 311.

By substituting $a_{0.16}$ = 3.5891Å, $a_{0.12}$ =3.5649Å, $C_{0.16}$=0.16, and $C_{0.12}$=0.12 into Eq. [17], which was shown previously, the η is calculated to be 0.1697.

$$\eta = \frac{a_{0.16}\ a_{0.12}}{a} \frac{1}{C\quad -C} \qquad [21]$$

From the phase diagram shown in Figure 6, the solid composition in equilibrium with liquid during CLFM C^s = 17.5 pct. The matrix compositions (C_0) for samples precipitated at 1150°C, 1100°C, and 1050°C are 15 pct, 14 pct, and 13 pct, respectively. Using Eq. [3b] below, which was shown previously, the strains for these matrix compositions are calculated to be 4.24×10^{-3}, 5.94×10^{-3}, and 7.64×10^{-3}, respectively.

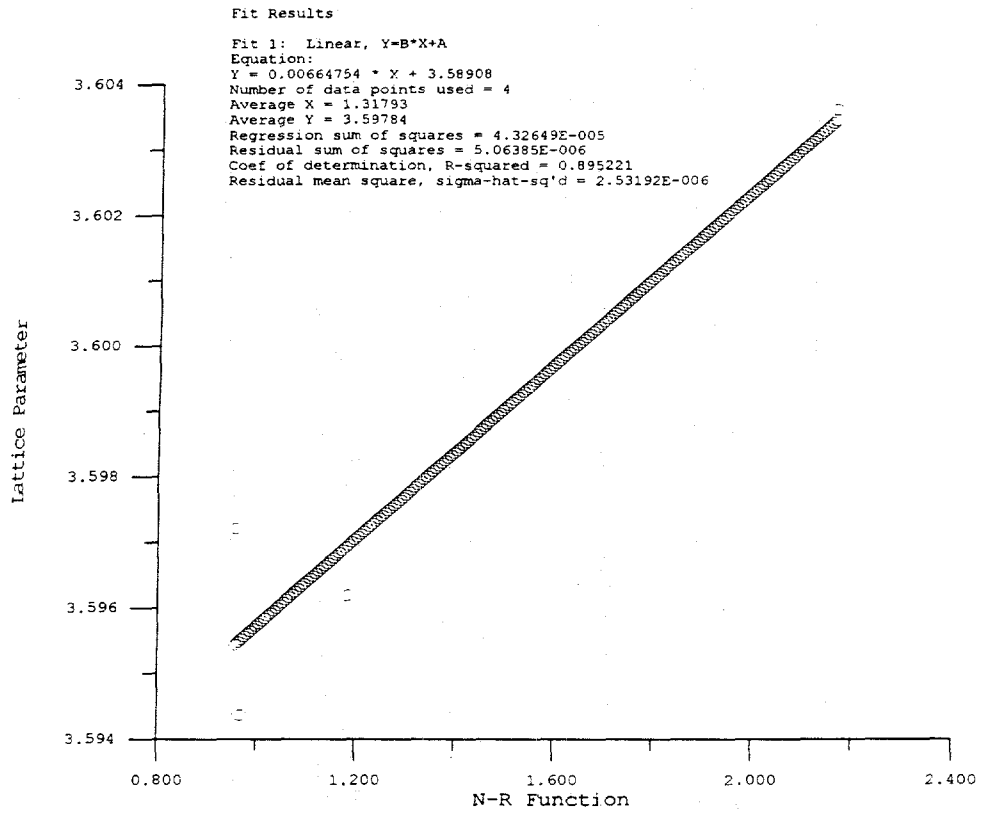

Fig. 25--Lattice parameter vs. N-R function for Ni-16%Nb alloy. The extrapolated lattice parameter is 3.5891Å.

$$\delta = (a-a_0)/a_0 = \eta\ (C^s-C_0) \qquad [3b]$$

Compared with strain needed to drive migration in LFM shown in Figure 4, the strain produced in Ni-16%Nb binary alloy is one order of magnitude greater and, hence, is believed to be able to drive CLFM.

2. *Migration velocity measurement*

A confidence interval of 90 pct was obtained for the counting statistics for the measurements of V_v and S_v, and the migration velocity was calculated from Eq. [20]. A plot of migration velocity versus isothermal holding time for samples, which were precipitated at 1150°C, followed by isothermal holds at a peak temperature of 1300°C, is shown in Figure 26. Figures 27 and 28 show similar plots for samples at 1100°C and 1050°C.

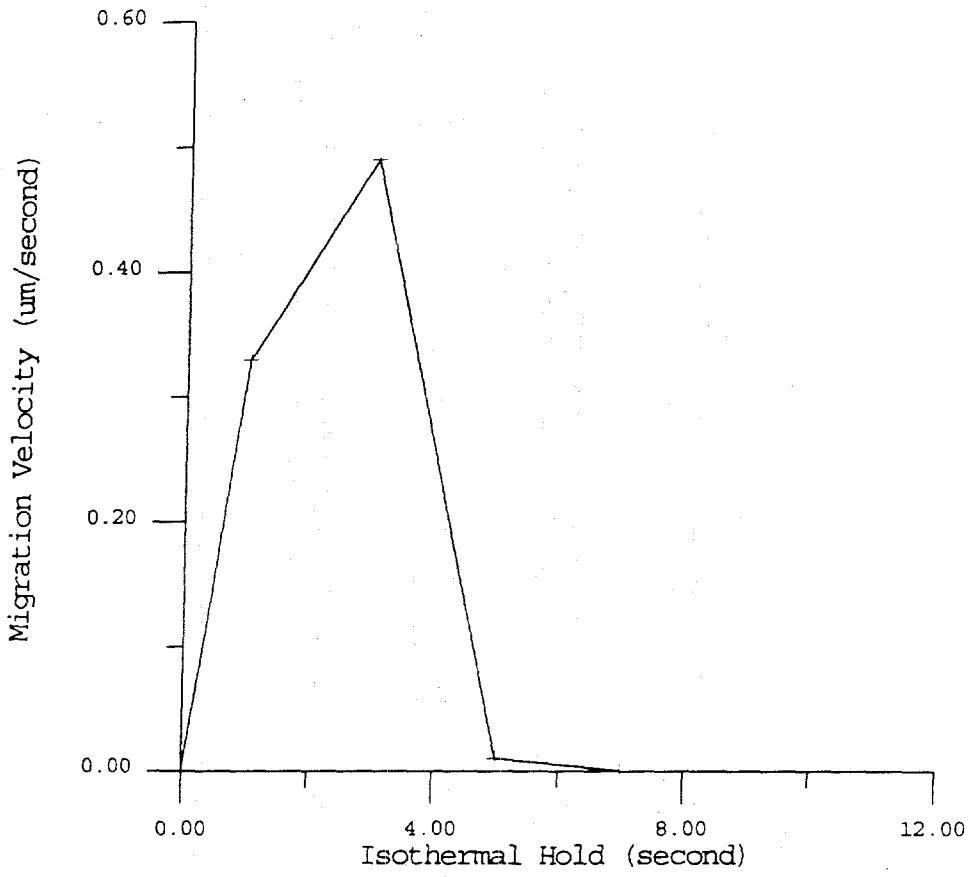

Fig. 26--Migration velocity versus isothermal hold for Ni-16%Nb samples that were homogenized at 1290°C for 24 hours, followed by a precipitation heat treatment for another 72 hours at 1150°C. The CLFM temperature was 1300°C.

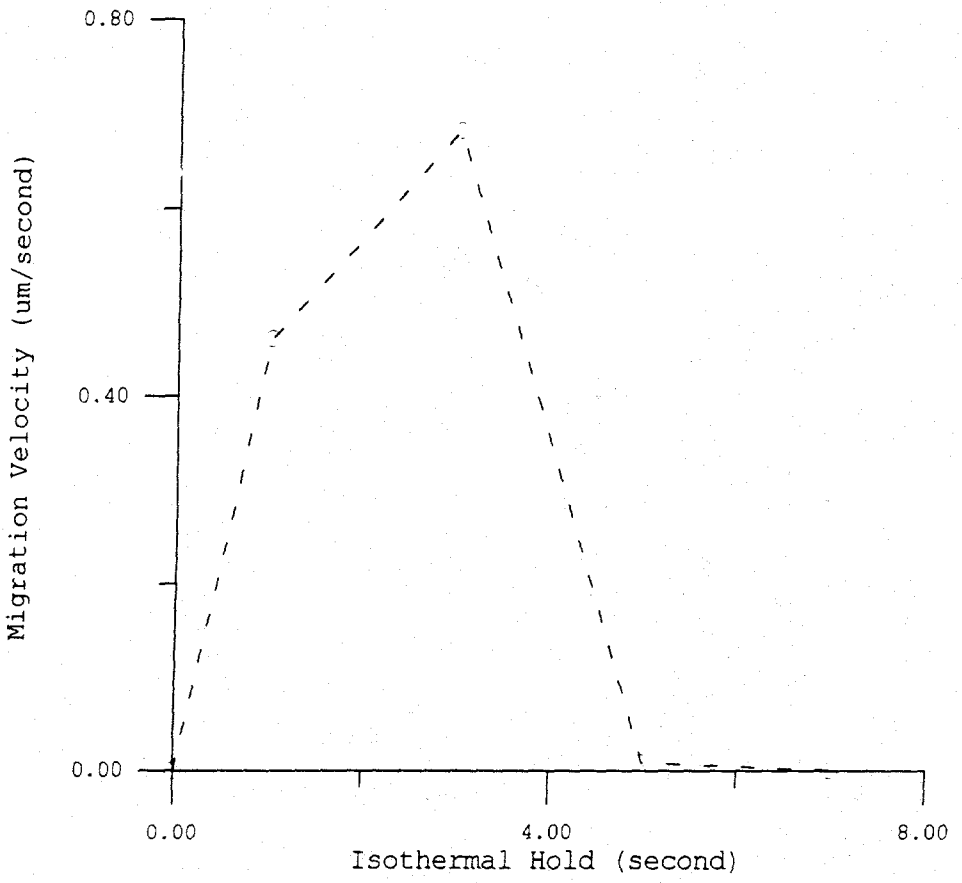

Fig. 27--Migration velocity versus isothermal hold for Ni-16%Nb samples that were homogenized at 1290°C for 24 hours, followed by a precipitation heat treatment for another 72 hours at 1100°C. The CLFM temperature was 1300°C.

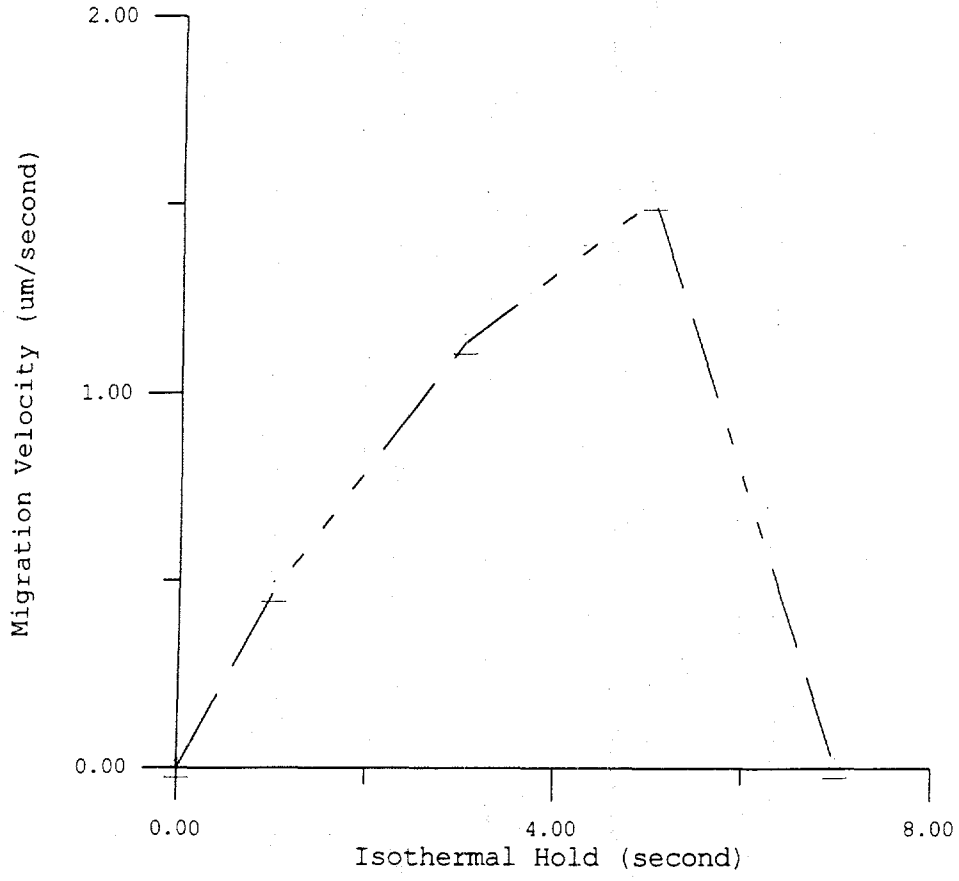

Fig. 28--Migration velocity versus isothermal hold for Ni-16%Nb samples that were homogenized at 1290°C for 24 hours, followed by a precipitation heat treatment for another 72 hours at 1050°C. The CLFM temperature was 1300°C.

CHAPTER 4.

DISCUSSION

The coherency strain hypothesis has often been cited as the mechanism responsible for DIGM and LFM (5,6,9,10,13). The main scope of this dissertation is not to prove or disprove the coherency strain hypothesis but to accept it as a basis for discussion in this dissertation. The purpose of this dissertation is to evaluate whether the coherency strain hypothesis also applies for CLFM. This is done by testing whether the model(s) of coherency strain hypothesis also accurately describes CLFM.

CLFM is similar to LFM characteristically, but unique in the formation of a liquid film by constitutional liquation of second phase precipitates on the grain boundaries. This chapter starts with a thorough examination of the stages involved in constitutional liquation, with the attempt to distinguish to which stage(s) the models of coherency strain hypothesis can be applied. A test of the coherency strain hypothesis for CLFM in alloy 718 is presented and discussed, based on whether the migration velocity predicted by the modified Hillert model fits the experimentally measured data. A further test is done in an Ni-16%Nb binary alloy system

exhibiting CLFM to evaluate whether both the modified Hillert model and Handwerker's model apply for CLFM.

A. *Application of coherency strain hypothesis to CLFM*

CLFM in alloy 718 has been observed to occur over a range of temperatures from subsolidus to supersolidus temperatures (24,29). However, subsolidus constitutional liquation differs from supersolidus constitutional liquation according to the phase diagram. A detailed description of each of these two processes is provided in the following sections.

1. *Subsolidus constitutional liquation*

Subsolidus constitutional liquation involves the formation of metastable liquid, as shown in Figure 29. It can be described by a three stage process; two stages during heating describe the liquation process, and the third stage describes final solidification (24).

In stage I, as shown in Figure 30(a), the precipitate melts by establishing a diffusion couple with the matrix. Stage I begins with the initiation of liquation and ends when the precipitate is completely liquated (Figure 30[b]).

Stage II covers the time required for the liquid to eliminate a diffusion gradient, as shown in Figures 30(c) and (d). Microstructurally, this stage is the time from when the precipitate finishes liquation until the grain boundary liquid film reaches its maximum thickness.

The kinetics of stages I and II should depend upon the ability of the liquid to wet the grain boundaries, which can be described by a balance of the surface tension of forces

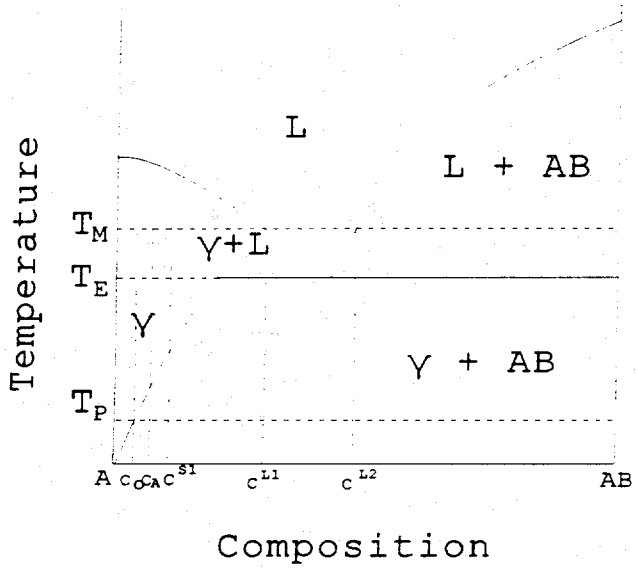

Fig. 29--Phase diagram showing subsolidus constitutional liquation of particle AB at temperature T_M. Compositions are C_0-matrix at room temperature, C_A-average alloy, C^{S1}-solidus, C^{L1}-liquid 1, C^{L2}-liquid 2, C_{AB}-phase AB.

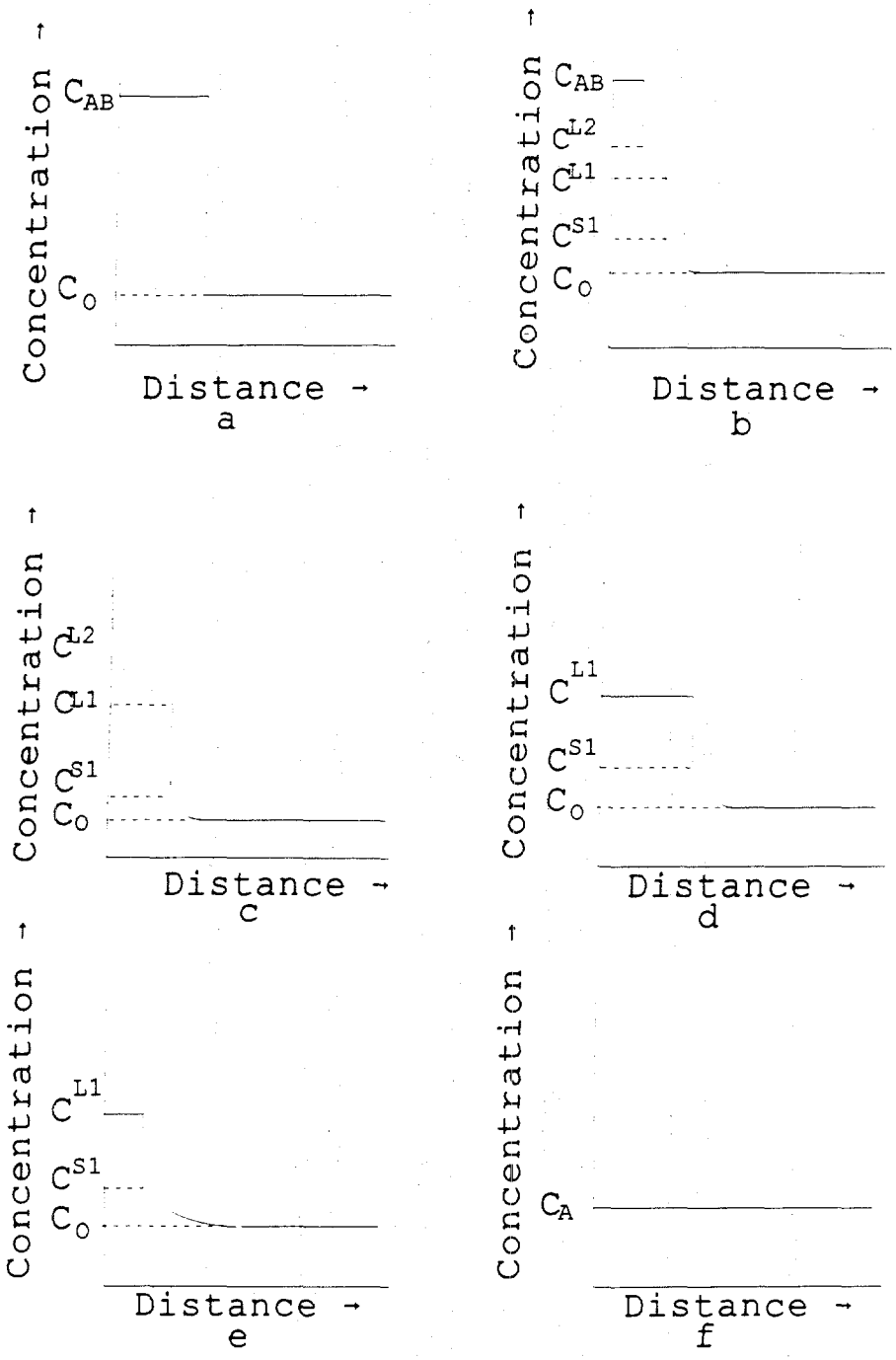

Fig. 30--Evolution of subsolidus constitutional liquation of the AB phase in the matrix of the binary alloy at temperature T_M. Stage I: (a,b) AB partially liquated. Stage II: (c) AB fully liquated, (d) concentration gradient eliminated in liquid. Stage III: (e) CLFM to eliminate excess solutes, (f) system equilibration by gradient elimination in solid.

at the triple point between the grain boundary liquid and the grain boundary. Spreading is favored if the S-L interfacial energy, γ^{SL}, is very small compared to the solid-solid interfacial energy (grain boundary energy), γ^{SS}. However, since the metastable liquid always reacts with the solid in which its dissolves, in the form of diffusion of solute(s) across the S-L interface, the nonequilibrium S-L interfacial energy is extremely low in alloy 718 (26), and the liquid completely wets the grain boundaries. During the spreading of solute(s) along the grain boundaries, an in-plane concentration gradient, ranging from C^{L1} to C^{L2}, exists, as shown in Figure 31. The concentration of the liquid in equilibrium with the matrix along which it spreads is always given by the concentration C^{L1}. It is assumed that complete mixing of solute(s) in liquid exists since the diffusion of solute(s) in liquid is fast with respect to solute diffusion into the matrix from the film. Thus, it can be expected that the concentration gradient will be eliminated at the end of stage II. Therefore, at the end of stage II, the solute concentration in contact with the matrix on both sides of the liquid film will be C^{L1}. It is assumed for this discussion that stage III runs from the point of maximum film thickness to the final solidification event.

The above analysis shows that when the alloy is rapidly heated to a subsolidus temperature which contains a tie-line to a liquid phase, the initial volume fraction of the liquid produced is greater than the equilibrium volume fraction of

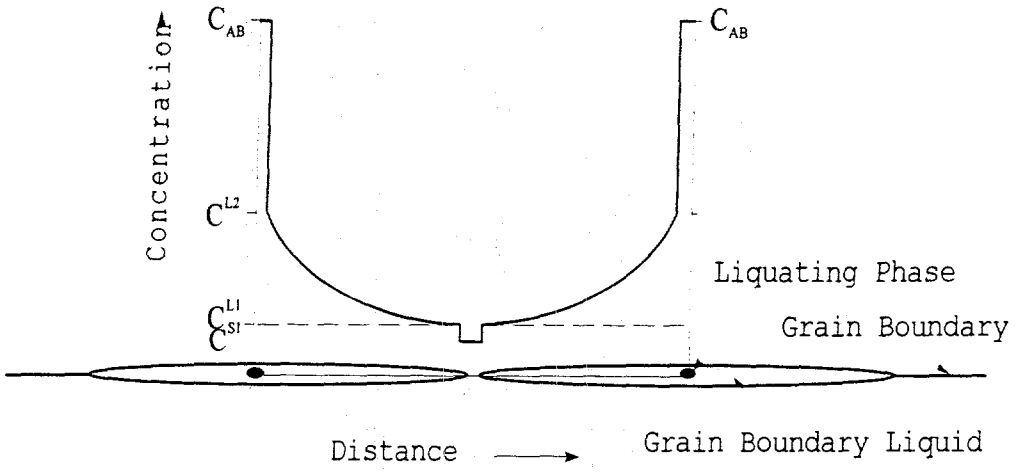

Fig. 31--Schematic of the formation of an in-plane concentration gradient in the grain boundary liquid film produced by constitutional liquation of AB particles. The concentration gradient is in accordance with the phase diagram shown in Figure 29.

liquid. Hence, the system is not initially in chemical equilibrium. The role of CLFM starting from stage III is to drive the system toward equilibrium by eliminating the excess liquid and solute produced during stages I and II with respect to chemical equilibrium. It should be noted from Figure 29 that CLFM could occur in a composition range crossing the L-S tie line until the liquid film collapses into a solid-state grain boundary. The system will ultimately reach equilibrium when the gradient in the solid is eliminated (Figure 30[f]).

2. Supersolidus constitutional liquation

Supersolidus constitutional liquation can be depicted using the phase diagram of Figure 32. The classification of stages of supersolidus constitutional liquation is similar to that of subsolidus constitutional liquation; that is, the supersolidus can also be described in a three-stage process.

Stage I, shown in Figure 33, begins with the initiation of liquation and ends when the precipitate is completely liquated.

Stage II covers the time required for the liquid to eliminate a diffusion gradient, as shown in Figures 33(c) and (d). Microstructurally, this stage is the time from when the precipitate finishes liquation until the grain boundary liquid film reaches its maximum thickness.

However, supersolidus constitutional liquation differs from subsolidus constitutional liquation in stage III. Supersolidus constitutional liquation is only partially

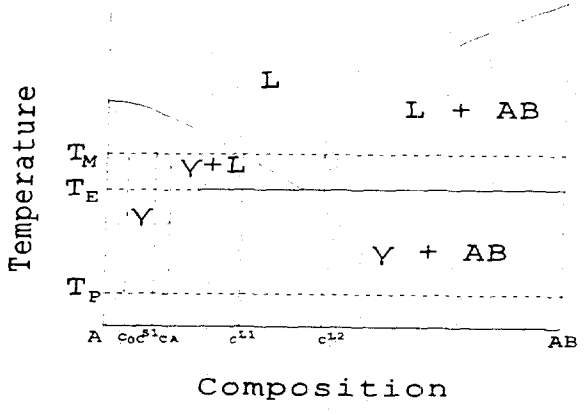

Fig. 32--Phase diagram showing supersolidus constitutional liquation of particle AB at temperature T_M. Compositions are C_0-matrix at room temperature, C_A-average alloy, C^{s1}-solidus, C^{L1}-liquid 1, C^{L2}-liquid 2, C_{AB}-phase AB.

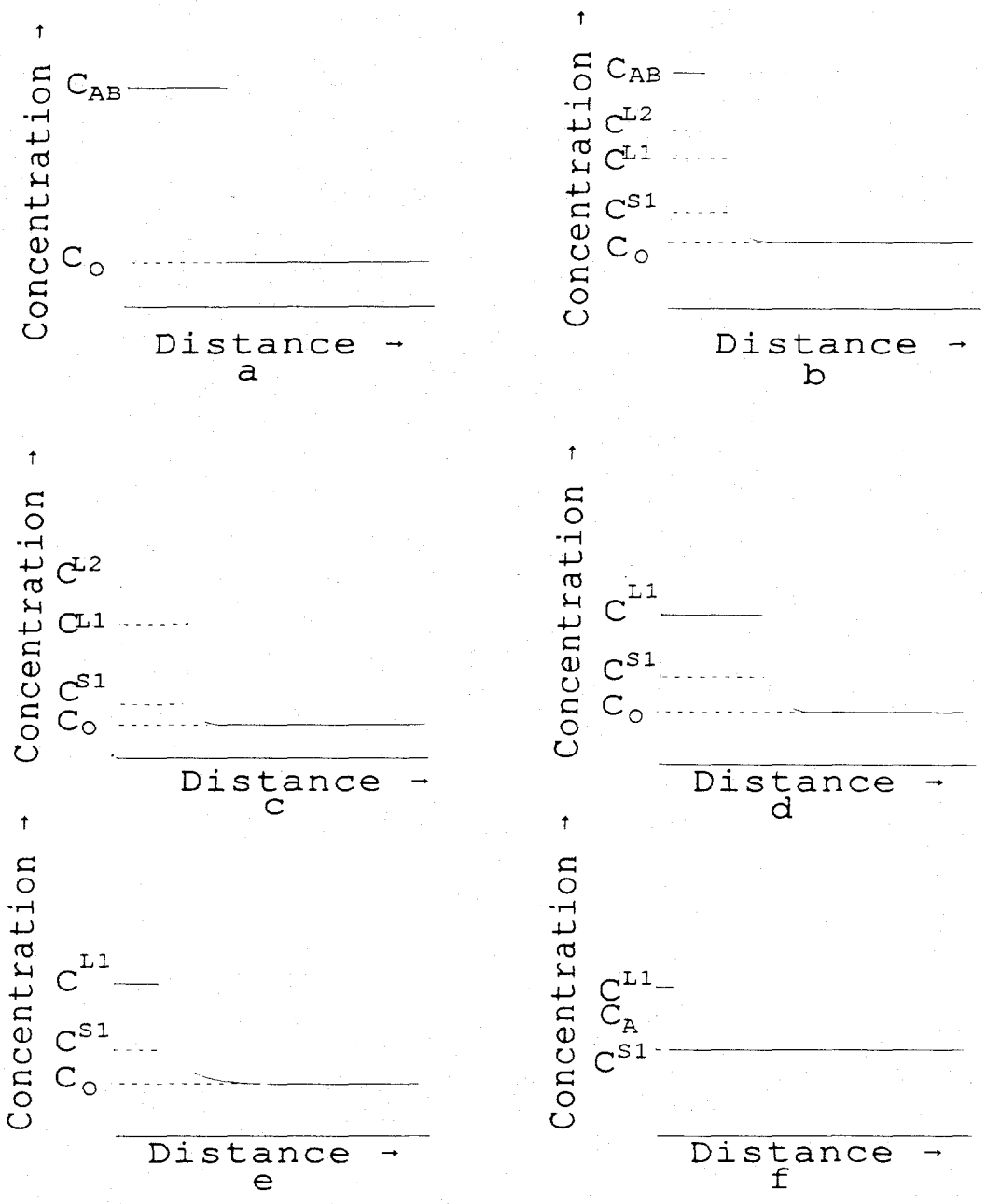

Fig. 33--Evolution of supersolidus constitutional liquation of the AB phase in the matrix of the binary alloy at temperature T_M. Stage I: (a,b) AB partially liquated. Stage II: (c) AB fully liquated, (d) concentration gradient eliminated in liquid. Stage III: (e) CLFM to eliminate excess solutes, (f) system equilibrated with a stable liquid volume fraction.

"constitutional" in the sense that once equilibrium is reached at T_M, there will be a stable volume fraction of liquid, as given by the phase diagram shown in Figure 32. In subsolidus constitutional liquation, CLFM starts at the beginning of stage III, with the composition crossing the S-L tie line given by the phase diagram (Figure 29), and stops when the liquid is completely consumed; thus, the liquid film collapses into a grain boundary. It is assumed for this discussion that CLFM in supersolidus constitutional liquation also starts at the beginning of stage III but stops once the equilibrium by the phase diagram is reached. A stable liquid film will still exist at the end of CLFM (Figure 32).

B. *Test of Coherency Strain Hypothesis in CLFM of Alloy 718*

The applicability of the coherency strain hypothesis to CLFM is tested by evaluating whether the modified Hillert model for coherency strain sufficiently describes CLFM in alloy 718. Section 1 deals with the prediction of migration velocity from the modified Hillert model, and Section 2 shows the migration velocity measured from the experiments. From a comparison between these two, it is then possible to show whether the modified Hillert model also applies for CLFM in alloy 718.

1. *Migration velocity vs. isothermal hold predicted by the modified Hillert model*

When Nb solute diffuses back into the matrix from the metastable liquid film, the solute concentration gradient

produces lattice strain. Under the circumstance that the temperature for constitutional liquation is close to the melting temperature of the alloy (i.e., T/T_m >0.9 [33]), dislocation interactions with the solute strain field on either side of the liquid film are ignored. The coherency strain is thus only a function of solute concentration gradient. A thermodynamic consideration discussed previously in Figure 2 leads to a concentration difference across the liquid film between the unstressed and stressed diffusion layers in Figure 3. This concentration difference, which is a function of the coherency strain, becomes the driving force term ΔC_L in the modified Hillert model of Eq. [11].

In the case of either sub- or supersolidus constitutional liquation, the liquid film thickness reaches a maximum value quickly at the end of stage II. A concentration gradient will build up across the liquid film, as shown in Figure 34, due to the orientation difference, according to the coherency strain hypothesis. Thus, migration will occur toward the right in Figure 34 to maintain interfacial equilibrium. The solute flux that must diffuse out of the distance dx into the matrix ahead of migrating interface in time period $d\lambda$ will be

$$J = - \frac{(C^l - C^s)}{V_M} \frac{dx}{d\lambda} = - \frac{(C^l - C^s) v}{V_M}, \qquad [21]$$

where V_M is the molar volume of the solute and v is the migration velocity. In the meantime, the flux across the concentration ΔC_L over the film thickness t will be

$$J = - D_L \frac{\partial C}{\partial x} = - D_L \frac{C_L}{t}. \qquad [22]$$

Equate equations 21 and 22 and rearrange, and we have the modified Hillert model of equation 11 that was previously shown in Chapter 1:

$$v = (D_L \bullet V_M \bullet \Delta C_L) / (C^l - C^s)\, t. \qquad [11]$$

It should be noted that the lateral flux has been assumed to be zero (Figure 3). In either supersolidus or subsolidus constitutional liquation, the lateral flux stops at the end of stage II, at which time the film thickness reaches a maximum value. As a result, the modified Hillert model can be used to describe CLFM, which occurs from the beginning of stage III.

It can be seen from the modified Hillert model of Eq. [11] that for a specific alloy system at a given temperature, D_L is the solute diffusivity in liquid; V_M is the molar volume of solute, which is assumed to be constant in both the solid and the liquid; and C^l and C^s are the equilibrium solute concentrations at the interface. Hence, ΔC_L and t are the only variables during isothermal liquation. One way to test the modified Hillert model would be to test whether the migration velocity is a function of driving force (ΔC_L) and film thickness (t) during stage III of constitutional liquation. These two factors are virtually impossible to measure quantitatively in situ during CLFM. However, the variation of ΔC_L with isothermal holding time can be predicted using the

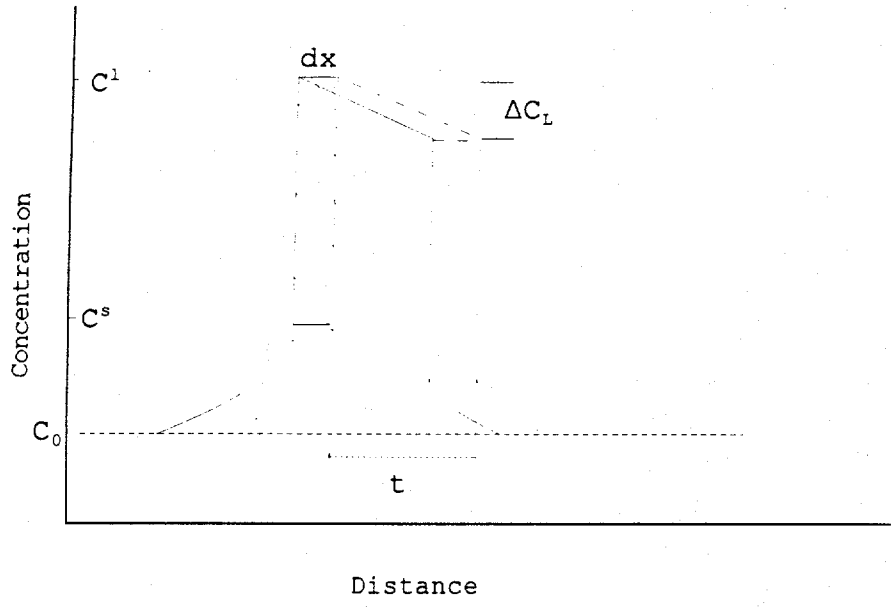

Fig. 34--Derivation of Hillert's model with the presence of a concentration gradient across the liquid film due to orientation difference on each side of the liquid film. The interface moves a distance of dx over time dλ.

coherency strain hypothesis, and the variation of film thickness t with isothermal holding time has been documented (24,25) for constitutional liquation. Hence, the modified Hillert model can be analyzed as a function of isothermal holding time. The trend of migration velocity varying as a function of isothermal holding time can then be predicted and compared with that experimentally observed. A good fit will then support the validity of the model.

a. *Predicted CLFM velocity at supersolidus temperatures*

Once the liquid film has formed along the grain boundary due to the liquation of either NbC in alloy 718 or Ni_3Nb in Ni-16%Nb alloy, back diffusion of Nb into the matrix on each side of the liquid film will occur. The time required to form a coherently strained layer with a typical thickness of 0.001 micron on both sides of the liquid film can be approximated using the following equation:

$$x = \sqrt{D_l \lambda}, \qquad [23]$$

where x is the thickness of diffusion layer, D_l is lattice diffusivity, and λ is time of diffusion. Taking x as 0.001 micron and D_l 10^{-7} cm^2/second, then the time of diffusion λ is calculated to be around one thousandth of a second. This means that the coherently strained layer can form instantaneously due to back diffusion of Nb into the matrices. Given the assumption concerning stage III of liquation and a large grain size which minimizes any curvature effects, the concentration

gradient across the liquid film can be considered as a constant prior to reaching chemical equilibrium. Thus, a stable ΔC_L-strain configuration can exist until the excess Nb relative to chemical equilibrium is completely consumed, at which time the volume of liquid in the system reaches its equilibrium level. Consequently, the driving force for CLFM drops to zero and CLFM stops. The variation of driving force (ΔC_L) with time is shown in Figure 35.

Consequently, the migration velocity varies exclusively with the inverse of the film thickness. Hence, the migration velocity can be predicted to increase to a peak velocity until the equilibrium is reached. The easiest way to treat the model mathematically is to assume that the film thickness decreases linearly with time during CLFM. As will be shown experimentally, this is a fairly close assumption.

The variation of liquid volume fraction as a function of isothermal hold in CLFM during supersolidus constitutional liquation for alloy 718 was shown by Thompson and Radkrishnan (24) in Figure 36. The volume fraction of liquid was seen to decline approximately in proportion to isothermal holding time at a peak temperature of 1227°C. The system reached chemical equilibrium at the 6th second of isothermal holding time and leveled off to a stable volume fraction of liquid. The volume fraction of liquid during stage III can be related to the film thickness in the following equation:

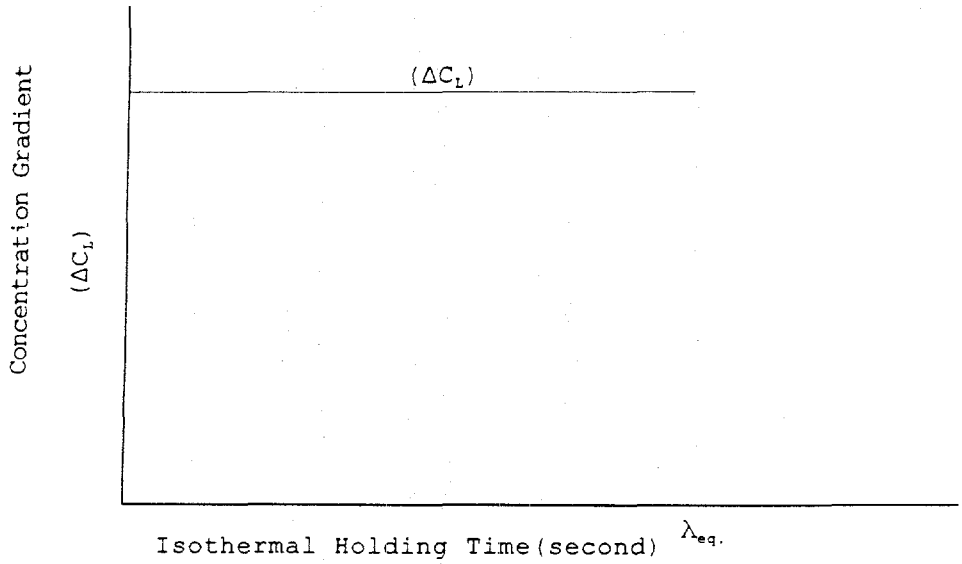

Fig.35--Variation of driving force with time in stage III of supersolidus constitutional liquation.

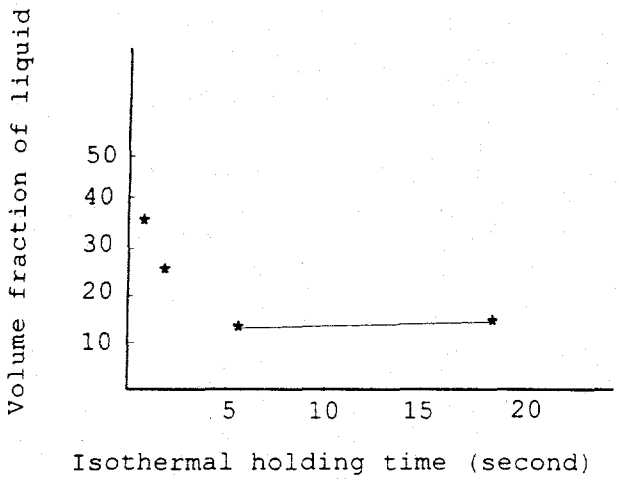

Fig. 36--Volume fraction of liquid as a function of isothermal hold during stage III of constitutional liquation of alloy 718 at 1227°C (Ref. 24).

$$V_v = S_v t, \qquad [24]$$

where V_v is the volume fraction of the liquid, S_v is the surface area per unit volume occupied by the liquid, and t is the film thickness. In stage III, where grain growth is no longer significant due to the pinning effect of the liquid film, the average grain size is assumed not to change with time, so S_v is constant during stage III. Consequently, the film thickness (t) changes in a manner proportional to V_v. Thus, the film thickness varies with isothermal holding time in a manner shown in Figure 37.

The driving force and film thickness from the beginning of stage III to the moment that the chemical equilibrium is reached can be expressed in terms of isothermal holding time λ as the following, respectively:

$$\Delta C_L = C_2 \qquad [25a]$$

$$t = -K_1\lambda + C_1 \qquad [25b]$$

where K_1 and C_2 are positive constants.

The modified Hillert model of Eq. [11] can be treated as a function of t and ΔC_L as the following:

$$v = K_2 \Delta C_L / t \qquad [26]$$

where K_2 is a positive constant accounting for a combined constant of $D_L V_M (C^l - C^s)$. Equations [25] and [26] can be combined to have

$$v = \frac{C_3}{-K_1\lambda + C_1}. \qquad [27]$$

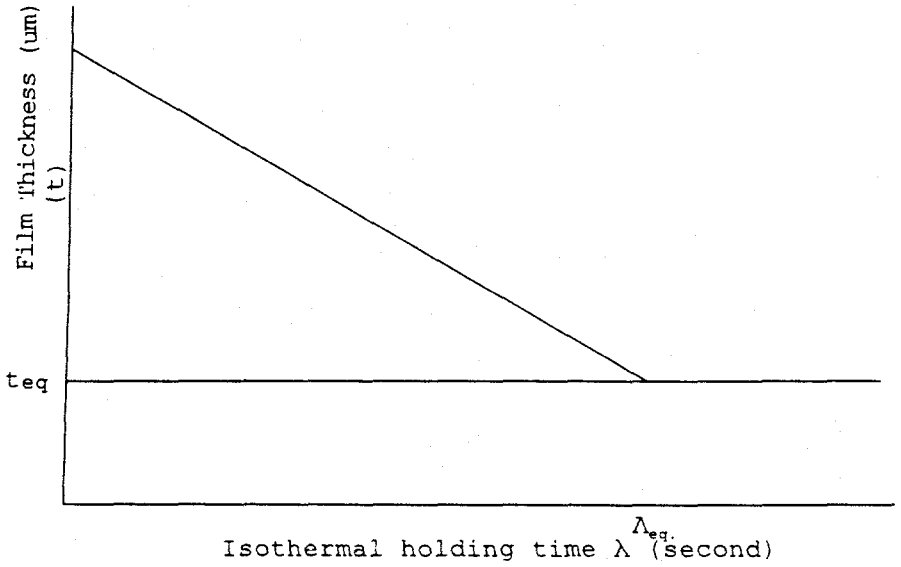

Fig. 37--Liquid film thickness as a function of isothermal hold during stage III of supersolidus constitutional liquation.

The shape of the curve represented by Eq. [27] can be estimated by taking the second derivative. A positive value of the second derivative indicates that there is a minimum value, so that the curve is concave downward, while a negative value of the second derivative indicates that there is a maximum value, so that the curve is concave upward. Taking the second derivative of Eq. [27], we have

$$v'' = -\frac{2C_3K_1}{(-K\lambda+C)^3} < 0. \qquad [28]$$

Hence, a combined effect of driving force and film thickness on migration velocity in stage III can be shown in Figure 38. The migration velocity in this stage is seen to experience an initial increase, followed by a maximum and then a rapid decline. Consequently, the modified Hillert model of Eq. [11] will predict that migration velocity will vary with time, as shown in Figure 38. One feasible experimental approach to test the modified Hillert model would be to test whether the migration velocity varies with time according to the prediction by the model just presented (i.e., whether the migration velocity will increase, reach a maximum, and then drop to zero with time).

b. *Predicted CLFM velocity at subsolidus temperatures*

CLFM at subsolidus temperatures can be expected to vary with isothermal holding time in a similar manner to supersolidus temperatures. However, CLFM at subsolidus temperatures can occur in the composition range that allows

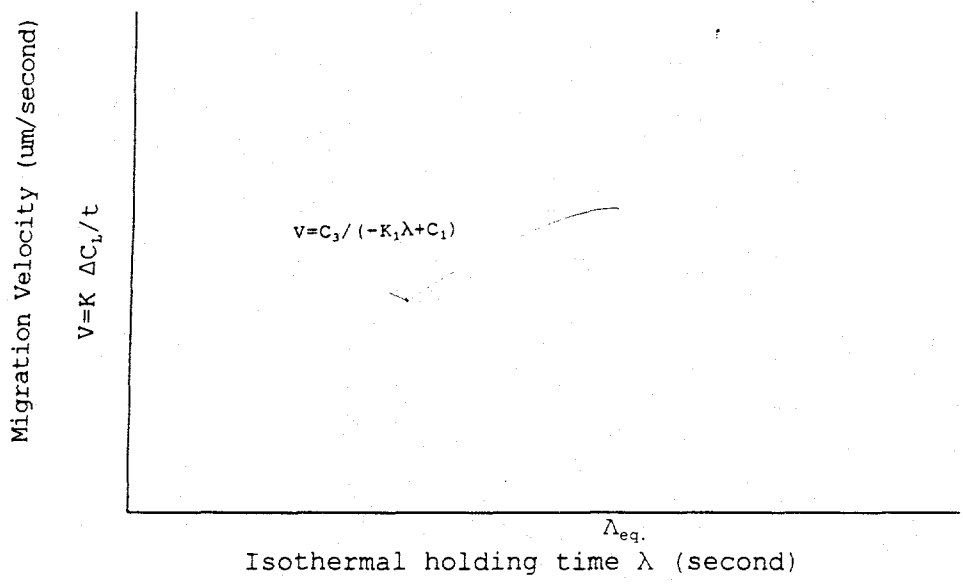

Fig. 38--Migration velocity vs. isothermal holding time predicted by the modified Hillert model for supersolidus constitutional liquation.

the liquid to cross the L-S tie line toward complete solid, at which point the liquid film collapses into a grain boundary. Therefore, the variation of migration velocity with isothermal holding time can be predicted in a manner synonymous with Figure 38.

Although no systematic results have been found on how the thickness of the liquid film varies during LFM/CLFM, a minimum liquid film thickness can be assumed to exist below which the liquid film will break up into isolated liquid blocks and eventually disappear by diffusion, or the film may wet the surfaces until it is of atomic dimensions, at which point it obtains the character of a grain boundary. Hence, CLFM migration will terminate.

In summary, both super- and subsolidus constitutional liquation can be divided into three stages of liquation, film growth, and migration. A concentration gradient across the liquid film can develop due to orientation differences according to the coherency strain hypothesis. CLFM is assumed to occur at the beginning of stage III. For supersolidus constitutional liquation, CLFM will stop once the chemical equilibrium determined by the phase diagram has been reached, by which time the excess Nb relative to the chemical equilibrium is completely depleted. For subsolidus constitutional liquation, CLFM will continue until the nonequilibrium liquid is completely depleted. The migration velocity is predicted by the modified Hillert model to increase to a maximum and drop to zero for both super- and

subsolidus constitutional liquation. For supersolidus constitutional liquation, migration velocity drops to zero because the chemical equilibrium of the system has been reached, while for subsolidus constitutional liquation, migration velocity drops to zero because the liquid is completely consumed. In either case, the shape of the migration velocity versus isothermal hold curve will be the same as long as the modified Hillert model holds.

2. *Experimental test of the modified Hillert model*

The migration velocity is predicted by the modified Hillert model to vary as a function of isothermal holding time. It will increase to a peak velocity and then drop to zero rapidly for CLFM during either supersolidus or subsolidus constitutional liquation (Figure 38).

Experimentally, similar curves have been obtained in CLFM of alloy 718, as shown in Figures 12 and 14 for a peak temperature of 1227°C and 1240°C, respectively. Figure 12 shows that at a peak temperature of 1227°C, the migration velocity increases and reaches a peak velocity at the 6th second of isothermal hold. The migration is observed to be around zero at the 8th second of isothermal hold.

A similar tendency has also been observed when alloy 718 was subjected to an isothermal holding cycle at a peak temperature of 1240°C. As shown in Figure 14, the migration velocity varies as a function of isothermal holding time. It quickly reaches a peak velocity at the 5th second of isothermal hold and then stops at the next observation.

All these predictions and experimental evidence indicate that the modified Hillert model holds for CLFM of alloy 718 and that the coherency strain hypothesis correctly predicts the behavior observed for CLFM in alloy 718.

C. *Test of Coherency Strain Hypothesis Using Binary Alloy Exhibiting CLFM*

CLFM was initially discovered in alloy 718, a multi-component system. When NbC on the grain boundary liquates constitutionally, the solutes in the liquid film spread along the boundary, forming a diffusion couple with the Ni matrix, thereby leading to the occurrence of CLFM. However, alloy 718 is such a complex system that many other matrix elements (Fe, Cr, etc.) and boundary elements (B, C, etc.) may contribute to the occurrence of CLFM. It is thus enlightening to study a binary system such as Ni-Nb.

The significance of studying CLFM in a binary alloy system is that the individual role of each element can be identified. In addition, the constitutional liquation of a specific binary system can be traced in terms of specific compositions given by the phase diagram. This section starts with the guidelines that were followed in search of CLFM in binary alloys. The test of the modified Hillert model and Handwerker's model on a proper binary alloy system is then presented.

1. *Guidelines for searching CLFM in binary alloys*

Because CLFM is similar to LFM in many ways, the conditions for LFM are usually also required for CLFM. The early search of CLFM started with systems that were found to exhibit DIGM and LFM. However, the occurrence of CLFM requires that additional conditions be met.

a. *Atomic misfit strain*

In most systems observed to exhibit DIGM, LFM, or CLFM (1-13), the atomic misfit strain was found to be greater than 10% in absolute value. This range of atomic misfit strain corresponds to diffusion species that will form substitutional diffusion. A slow lattice diffusivity due to substitutional diffusion will favor the accumulation of the coherently strained layer ahead of the migrating interface.

b. *Homologous temperature*

If a coherency strain hypothesis holds for CLFM, then it might be expected that a temperature would exist above which coherent lattice strain could no longer be developed. The calculation normally made to describe the potential strain in the matrix associated with the addition of a solute atom is a ratio of atomic size difference over the original atomic size. However, such a calculation begins to lose meaning as the melting point of the matrix is approached. A homologous temperature (T_{he}) is defined as the migration or liquation temperature of the system relative to the melting point of the pure matrix element. At this high value of T_{he}, the lattice is

greatly expanded with thermal energy and the solute atoms have significant space in which to be accommodated without strain. Thus, T_{he} has to be taken into consideration in search of CLFM in binary alloys.

c. *Grain boundary wettability*

The pre-condition for the occurrence of CLFM is that the liquid film produced from liquating precipitates can wet and spread along the grain boundaries. The binary alloy systems are thus sought based on whether the precipitates on the boundary can liquate and spread along the boundary. A good indication of wettability is that a continuous intergranular precipitate can be obtained on the grain boundary by proper heat treatment.

d. *Phase diagram requirement*

In addition to the above-mentioned conditions, a phase diagram requirement has to be met in the alloy system that has been observed to exhibit CLFM. The phase diagram of the chosen alloy should allow a relatively wide range of precipitation heat treatment temperature (Figure 6). The peak temperature of constitutional liquation should be low enough to be achieved in the Gleeble 1000 system.

2. *Test of coherency strain hypothesis in binary alloy*

Binary alloy systems initially sought for CLFM included Al-4%Cu, Co-10Nb, Mo-1%Nb, Ni-36%Mo, and Ni-16%Nb. The latter two systems were found to have all the above requirements and to exhibit significant CLFM. The Ni-16%Nb alloy was used to

conduct a systematic test of the coherency strain hypothesis, as discussed in the following sections.

a. *Test of the modified Hillert model*

When the binary alloy shown in Figure 39 is given different precipitate growth temperatures T_1 and T_2, the matrix compositions will be C_{01} and C_{02}, respectively. The volume fraction of precipitates will be greater for the system that is precipitated at a lower temperature (T_2). When these two alloy systems are rapidly heated to the same constitutional liquation temperature T_M, it can be expected that at the end of stage II, the volume fraction of liquid will be greater for the system that has a greater volume fraction of precipitates. Thus, the initial film thickness is greater for the system that has a higher initial volume fraction of precipitates. However, it can be expected that the film thickness with different initial values will reduce to the same minimum value at the end of CLFM when the solute is completely depleted. This minimum film thickness is independent of initial precipitate volume fraction as long as the constitutional liquation temperature remains the same. The only difference is that it takes longer for the system with a higher volume fraction of liquid to reach the same minimum film thickness. The thickness of the liquid film varies in proportion to the liquid volume fraction according to Eq. [24] (previously shown):

$$V_v = S_v\, t; \qquad [24]$$

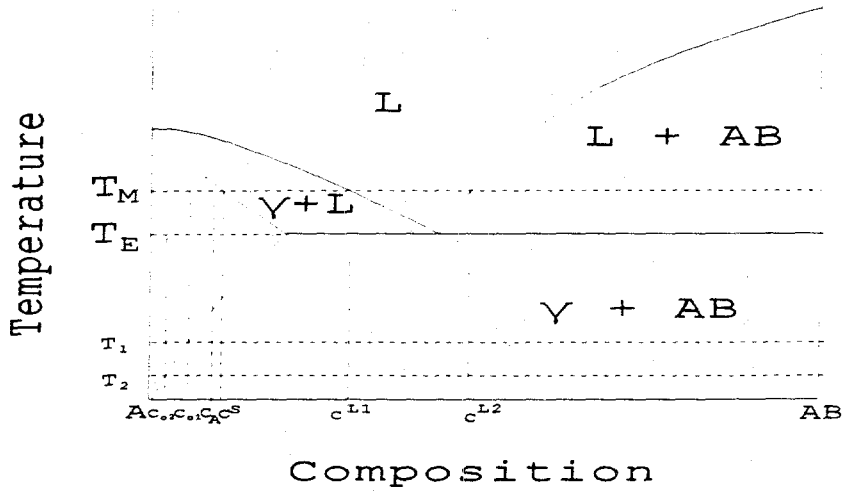

Fig. 39--Schematic showing a binary alloy with average composition C_A precipitated at different temperatures T_1 and T_2 to obtain different matrix compositions C_{o1} and C_{o2}, respectively. Notice the volume fraction of AB phase will be greater at a lower precipitation temperature.

therefore, the variation of liquid film thickness (t) with time is approximately linear and can be shown in Figure 40.

The concentration gradient across the liquid film can be evaluated from Eq. [9], which was previously shown in chapter 1.

$$\Delta C_L = \frac{V_m}{RT}\left[\left(Y(\overline{n_A}) - Y(\overline{n_B})\right)\eta^2 (C^s - C_0)^2 + 2\sigma(x_A - x_B)\right]\frac{C^l(1-C^l)}{(C^l - C^s)} \qquad [9]$$

Once migration occurs into a grain at a given peak temperature and curvature effect, the above equation becomes the following:

$$\Delta C_L = \frac{V_m}{RT}\left[Y(\overline{n_A})\eta^2 (C^s - C_0)^2\right]\frac{C^l(1-C^l)}{(C^l - C^s)}. \qquad [29]$$

It can be seen from the equation that the concentration gradient varies with grain orientation. Once the alloy system and migrating grain pairs are fixed, the concentration becomes a sole function of concentration gradient. Therefore, the concentration gradient will be a constant for each alloy system precipitated at a specific temperature. However, for alloy systems precipitated at different temperatures, the concentration gradient will be a function of $(C^s - C_0)$. Figure 39 shows that an alloy system that is precipitated at a lower temperature will have a greater $(C^s - C_0)$ value and thereby a greater driving force. The starting film thickness will be greater, resulting from a higher volume fraction of AB particles at a lower precipitation temperature. Thus, the time required to reach the same minimum film thickness will be

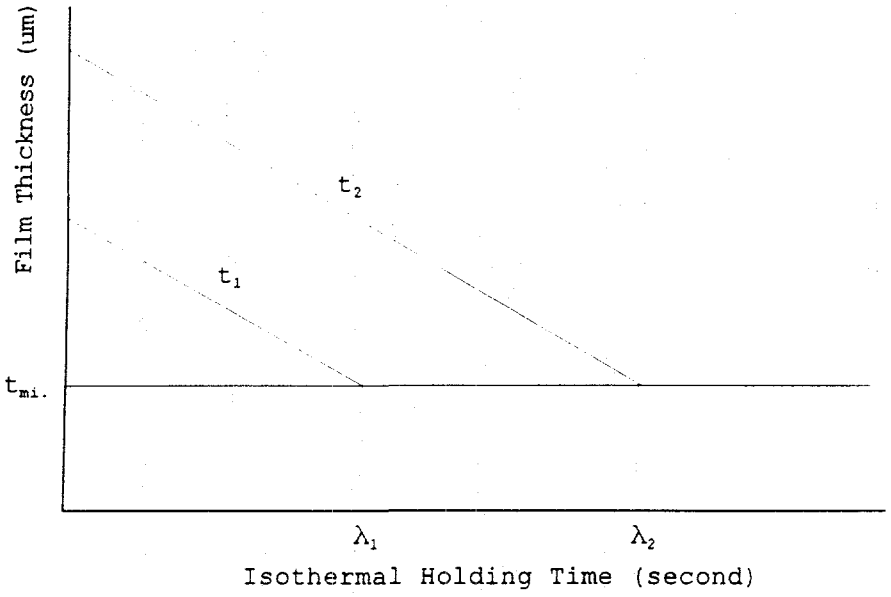

Fig. 40--Film thickness as a function of isothermal holding time in stage III of subsolidus constitutional liquation for different starting film thicknesses due to different initial volume fraction of second phase precipitates.

longer. The migration velocity for each alloy precipitated at different temperatures will reach a peak value when the minimum film thickness is reached. The highest peak migration velocity occurs when the film thickness of the alloy system precipitated at the lowest temperature reached the minimum value. Thus, a plot of concentration gradient versus isothermal holding time can be shown in Figure 41 for two alloys that are precipitated at different temperatures. A plot of migration velocity versus isothermal holding time predicted from the modified Hillert model can then be obtained by combining Figures 40 and 41. The resulting plot is shown in Figure 42.

The experimental proof supporting the above theoretical discussion has been found in the CLFM study of the binary alloy Ni-16%Nb. The Ni-16%Nb alloy was precipitated at temperatures of 1150°C, 1100°C, and 1050°C. The samples were exposed to CLFM at a peak temperature of 1300°C for varying isothermal holding times. The plots of migration velocity versus isothermal holding time are shown in Figures 26-28.

The variation of migration velocity versus isothermal holding time in CLFM of Ni-16%Nb binary alloy shown in Figures 26-28 is seen to be similar to those observed in CLFM of alloy 718, as shown in Figures 12 and 14. It should be noted that stages I and II of constitutional liquation in this alloy are expected to be complete prior to the first second of isothermal hold (24, 27), so all the plots shown here are

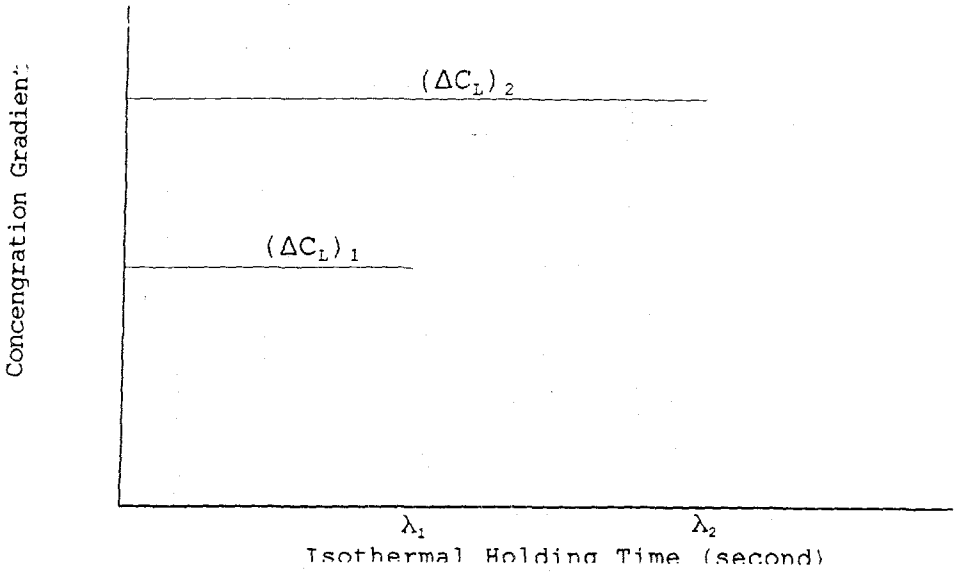

Fig. 41--Concentration gradient across the liquid film as a function of isothermal holding time in stage III of subsolidus constitutional liquation for different starting concentration gradients but same orientation dependent modulus.

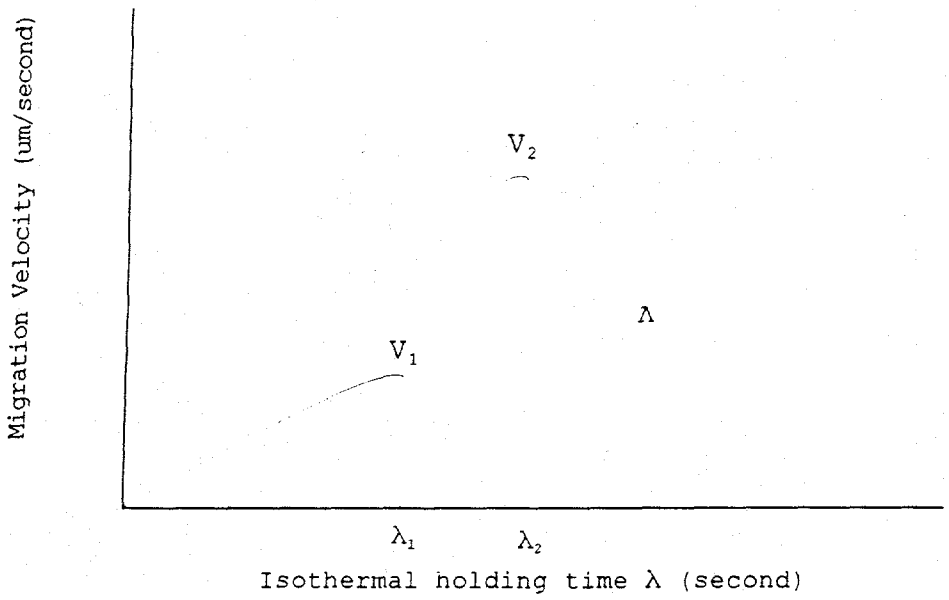

Fig. 42--Migration velocity as a function of isothermal holding time in stage III of subsolidus constitutional liquation. Different curves result from the modified Hillert model that combines film thickness and concentration gradient from Figures 40 and 41.

assumed to start from stage III of constitutional liquation. For the Ni-16%Nb alloy that was precipitated at 1150°C, as shown in Figure 26, the migration velocity is observed to increase, reach a peak velocity at the 3rd second of isothermal hold, and quickly decline to zero at the 5th second of observation. The Ni-16%Nb alloy precipitated at 1100°C is also shown in Figure 27 to have a higher peak velocity at the 3rd second of isothermal hold and to reach zero velocity at the 5th second of observation. The Ni-16%Nb alloy precipitated at 1050°C is seen to have the highest peak velocity at the 5th second of isothermal hold and to decline to zero at the 7th second of observation.

A plot combining Figures 26-28 is shown in Figure 43. Comparing Figure 43 with Figure 42, it can be seen that experimental results match the trend of theoretical prediction well.

The match between the experimental results of CLFM in the binary alloy and those predicted by the modified Hillert model of LFM clearly indicates that the coherency strain hypothesis of LFM can be used to describe CLFM in the binary alloy.

b. *Test of Handwerker's model*

Once migration is initiated for a given alloy system at a given constitutional temperature, the driving force is a constant if the curvature effect is ignored. The curvature effect was shown to be much less significant than the lattice strain (3,9,10) term. Figures 18-20 show that the migrating

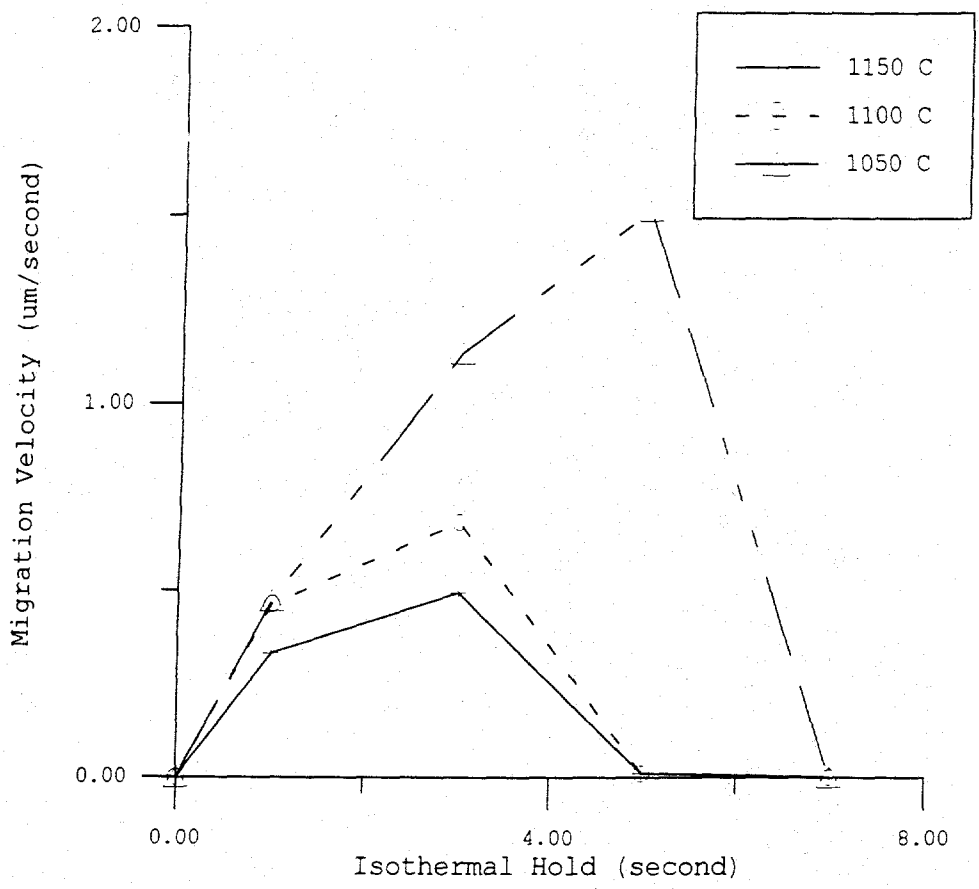

Fig. 43--Migration velocity versus isothermal hold for Ni-16%Nb samples that were homogenized at 1290°C for 24 hours, followed by a precipitation heat treatment for another 72 hours at 1150°C, 1100°C, and 1050°C. The CLFM temperature was 1300°C.

interface is fairly flat as grain growth was very significant during precipitation heat treatment, creating a large grain size (>200 um); therefore the assumption that the curvature effect was insignificant and could be ignored appeared to be reasonable in this study. Thus, the driving force can be expressed as the following equation, assuming the migration is into grain A:

$$\Delta C_L = \frac{V_m}{RT}\left[Y(\overline{n_A})\,\eta^2 (C^s - C_0)^2\right]\frac{C^l(1-C^l)}{(C^l-C^s)}. \qquad [29]$$

This concentration gradient represents the maximum driving force for CLFM. The corresponding migration velocity will be

$$v = \frac{D_{liq}V_m}{tRT}\left[(Y(\overline{n_A})\,\eta^2 (C^s - C_0)^2\right]\frac{C^l(1-C^l)}{(C^l-C^s)^2}. \qquad [30]$$

When dealing with the peak migration velocity for each Ni-16%Nb binary alloy system precipitated at different temperatures, the film thickness in this equation for sub-solidus liquation becomes the same minimum film thickness for different initial volume fractions of second phase (Ni_3Nb) precipitates. The curvature effect is minimized by a large grain size, as witnessed in Figure 16 for the Ni-16%Nb system. At a given temperature, molar volume, diffusivity, and equilibrium compositions at the interface are all constant. Hence, it can be seen for a given orientation dependent modulus from the above equation that the migration velocity should vary as a function of lattice strain δ^2 (where a δ =

$\eta[C^s-C_0]$), resulting from the precipitation heat treatment of the Ni-16%Nb alloy systems at different temperatures. As a result, Handwerker's model of Eq. [30] can be tested by evaluating whether the migration velocity varies as a function of lattice strain δ^2. Similar work was done in LFM by Song *et al.* (13), as shown in Figure 4. This result provided convincing evidence that coherency lattice strain is the driving force for LFM.

For a well defined binary system such as an Ni-Nb system (Figure 6), C^s is the composition of the precipitate and C_0 is the matrix composition. When CLFM occurs in a system such as Ni-16%Nb, precipitates of Ni_3Nb can be grown at a range of temperatures to yield different matrix compositions (C_0), while the precipitate concentration remains constant as C^s. The calculations in the section "Strain calculation through x-ray diffraction" in Chapter 3 has shown that the lattice strain at these C_0 compositions is around 0.001, almost one order of magnitude greater than what is necessary to drive migration, as shown in Figure 4. If it can be proven that migration velocity varies as a function of (C^s-C_0) in a parabolic curve, then it can be argued that the coherency strain hypothesis holds for CLFM.

The lattice strain calculation was done using lattice parameter measurement by x-ray diffraction and using Eq. [17], shown previously in Chapter 3:

$$\eta = \frac{a_{0.16} \; a_{0.12}}{a} \frac{1}{C \quad -C} . \qquad [17]$$

The lattice parameter of an Ni-16%Nb alloy, $a_{0.16}$, was measured to be 3.5891Å (Figure 23). The lattice parameter for an Ni-12%Nb alloy, $a_{0.12}$, was measured to be 3.5649Å. Putting $C_{0.16}$ = 0.16 and $C_{0.12}$ = 0.12 into Eq. [17], the η is calculated to be 0.1697.

From the phase diagram shown in Figure 6, the solid composition in equilibrium with liquid during CLFM is C^s = 17.5%. The matrix compositions (C_0) for samples precipitated at 1150°C, 1100°C, and 1050°C are 15 pct, 14 pct, and 13 pct, respectively. Using Eq. [3b] in Chapter 1, the strains for these matrix compositions are calculated to be 4.24×10^{-3}, 5.94×10^{-3}, and 7.64×10^{-3}, respectively.

A plot of the peak migration velocity for CLFM of binary alloy Ni-16%Nb versus different lattice strains resulting from different precipitation heat treatments is shown in Figure 44. The dependence of peak migration velocity on lattice strain is clearly seen. Similar to the liquid phase sintering work in an Mo-Ni alloy by Song *et al.* (13), as shown in Figure 4, a parabolic curve was obtained. This is convincing evidence that Handwerker's model applies to CLFM, indicating the coherency strain hypothesis holds for CLFM. It should be noted that in Figure 44 the migration velocity is assumed to be zero when δ is zero, according to the coherency strain hypothesis.

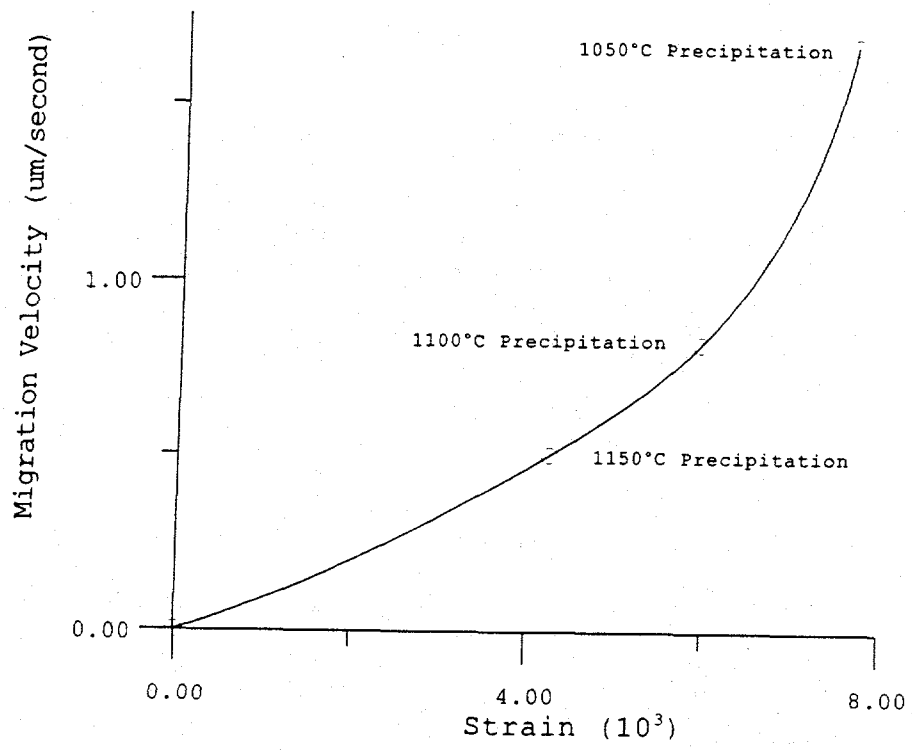

Fig. 44--Peak migration velocity as a function of strain during CLFM for samples precipitated at different temperatures.

D. *Experimental Error*

Two main sources of experimental error were considered during the experimental work. One source was from the measurement of migration velocity using the Cahn-Hagel equation. A systematic error was involved when measuring the slope $dV_v/d\lambda$, where V_v is the volume fraction of newly formed solid solution behind the migrating interface and λ is the isothermal holding time. The slope was measured consistently for different isothermal holding times, so systematic error was kept to a minimum.

The other main source of experimental error was from the determination of the time at which the migration velocity reached a maximum peak velocity. The migration velocity was observed at isothermal holding times of 1, 3, 5, 7, and 9 seconds of isothermal hold, respectively. The peak velocity was assumed to be at the integer second of the observation. In reality, the peak migration velocity might lead or lag behind the observed peak migration velocity.

The correlation between experimental results and predicted behavior is taken as an indication that this experimental design error did not significantly alter the analysis.

CHAPTER 5.

SUMMARY AND CONCLUSION

A. *The Applicability of the Coherency Strain Hypothesis of LFM to CLFM in Alloy 718*

The coherency strain hypothesis was tested by evaluating whether the modified Hillert model used by previous researchers to describe LFM could also be applied to CLFM. For both super- and subsolidus constitutional liquation, the CLFM migration velocity was predicted to vary as a function of isothermal holding time using the modified Hillert model. Migration was predicted to increase to a maximum peak velocity and then quickly drop to zero during isothermal hold. Experimental results of CLFM in alloy 718 at both 1227°C and 1240°C showed that migration velocity followed this trend predicted by the modified Hillert model. This indicates that the coherency strain hypothesis for LFM also describes CLFM. It was thus concluded that the lattice strain was the driving force for CLFM.

B. *The Applicability of the Coherency Strain Hypothesis of LFM to CLFM in Ni-16%Nb Binary Alloy*

1. *Test of the modified Hillert model*

CLFM was successfully sought in an Ni-16%Nb binary alloy system. Samples of Ni-16%Nb alloy were precipitated at

temperatures of 1150°C, 1100°C, and 1050°C to yield different volume fractions of Ni_3Nb precipitates. An isothermal cycle treatment at 1300°C allowed a subsolidus constitutional liquation according to the phase diagram.

The experimental results showed that migration velocity varied as a function of isothermal holding time, following the trend predicted by the Hillert. This result was taken as proof that the coherency strain hypothesis correctly describes CLFM.

2. *Test of Handwerker's model*

The peak migration velocity was found to be related to the precipitation temperatures. The lower precipitation temperature yielded a higher lattice strain in the diffusion layer ahead of the migrating interface, thus causing a higher peak velocity. Handwerker's model predicted that the peak velocity would vary with lattice strain in a parabolic manner for LFM. The experimental results in this dissertation demonstrated that this was also the case for CLFM. Thus, the coherency strain hypothesis of this model was also found to describe CLFM.

LIST OF REFERENCES

1. F.J.A. Den Broader: *Acta Metall. Mater.*, 1972, vol. 20, pp. 319-332.

2. M. Hillert and G.R. Purdy: *Acta Metall. Mater.*, 1978, vol. 26, pp. 333-340.

3. R.W. Baluffi and J.W. Cahn: *Acta Metall. Mater.*, 1981, vol. 29, pp. 493-500.

4. Y.J. Baik and D.N. Yoon: *Acta. Metall. Mater.*, 1986, vol. 34, pp. 2039-2044.

5. C.A. Handwerker: *Diffusion Phenomena in Thin Films and Microelectronic Materials*, D. Gupta and P.S. Ho, eds., Noyes Publications, NJ, 1989.

6. M. Hillert: *Scripta Metall.*, 1983, vol. 17, pp. 237-240.

7. J.W. Cahn: *Acta Metall. Mater.*, 1961, vol. 9, pp., 795-801.

8. F.C. Larche and J.W. Cahn: *Acta Metall. Mater.*, 1985, vol. 33, 331-357.

9. C.A. Handwerker, J.W.Cahn, D.N. Yoon, and J.E. Blendell: TMS/AIME Publication, Warrendale, PA 1985.

10. D.N. Yoon, J.W. Cahn, C.A. Handwerker, J.E. Blendell, and Y.J. Baik: ASM Press, Metals Park, OH 1985.

11. Y. Brechet and G.R. Purdy: *Scripta Metall.*, 1988, vol. 22, pp. 1629-1633.

12. H.K. Kang, S. Hackney, and D.N. Yoon: *Acta Metall. Mater.*, 1988, vol. 36, pp. 695-699.

13. Y.D. Song, S.T. Ahn, and D.N. Yoon: *Acta Metall. Mater.*, 1985, vol. 33, pp. 1907-1910.

14. D.N. Yoon: *Annu. Rev. Mater. Sci.*, 1989, vol. 19, pp. 43-58.

15. B. Radhakrishnan and R.G. Thompson: *Scripta Metall.*, 1990, vol. 24, pp. 537-542.

16. B. Radhakrishnan and R.G. Thompson: accepted for publication in *Metall. Trans. A.*.

17. J.J. Pepe and W.F. Savage: *Welding Journal*, 1967, vol. 46, pp. 411-s-422-s.

18. B. Radhakrishnan and R.G. Thompson: *Metall. Trans. A*, 1992, vol. 12A, pp. 1783.

19. W.H. Rhee and D.N. Yoon: *Acta Metall. Mater.*, 1987, vol. 35, pp. 1447-1451.

20. T. Mushik, W.A. Kaysser, and T. Hehenkamp: *Acta Metall. Mater.*, 1989, vol. 37, pp. 603-613.

21. Y.S. Kucharenko: *Phys. Metall.*, 1975, vol. 39, pp. 121-128.

22. M. Sulonen: *Z. Metallk.*, 1964, vol. 55, pp. 543.

23. Y.J. Baik and D.N. Yoon: *Acta Metall. Mater.*, 1989, vol. 33, pp. 1911-1917.

24. B. Radhakrishnan and R.G. Thompson: Proceedings of the 2nd International Conference on Trends in Welding Research, Gatlinburg, Tennessee, 1993, pp. 637-648.

25. B. Radhakrishnan and R.G. Thompson: *Metall. Trans. A*, 1992, vol. 21A, pp. 1356-1422.

26. B. Radhakrishnan and R.G. Thompson: *Metall. Trans. A*, 1992, vol. 23, pp. 1783-1799.

27. V.L. Acoff, R.G. Thompson, and R.D. Griffin: *Proceedings of 1994 Solid-Solid Phase Transformations Conference*, 1994, in press

28. C.A. Handwerker: *Duffusion Phenomena in Thin Films and Microelectronic Materials*, Noyes Publications, NJ, 1988.

29. R.W. Balluffi and J.W. Cahn: *Acta Metall. Mater.*, 1981, vol. 29, pp. 493-500.

30. D. Broeder: *Thin Solid Films*, 1985, vol. 124, 135-148.

31. D. Broeder: *Scripta Metall.*, 1983, vol. 17, pp. 399-404.

32. K. Tashiro and G. Purdy: Scripta. Metall., 1983, vol. 17, pp. 455-458.

33. J. Askill: *Tracer Diffusion Data for Metals, Alloys and Simple Oxides*, IFI/Plenum Publishing Co., NY, 1970.

34. B. Radhakrishnan: *Ph.D. Dissertation*, The University of Alabama at Birmingham, 1989.

35. V. Voort: *Metallography Principles and Practice*, McGraw-Hill Book Company, NY, 1984.

36. R. Dehoff and F. Rhines: *Quantitative Microscopy*, McGraw-Hill Book Company, NY, 1968.

37. C. Barrett and T. Massalski: *Structure of Metals*, 3rd Rev. Ed., International Series on Materials Science and Technology, vol. 35, 1987.

GRADUATE SCHOOL
UNIVERSITY OF ALABAMA AT BIRMINGHAM
DISSERTATION APPROVAL FORM

Name of Candidate Hongjun Zuo

Major Subject Materials Engineering

Title of Dissertation Mechanism of Constitutional Liquid Film Migration

Dissertation Committee:

Ray Thompson, Chairman

Ray Thompson

J. M. Rigsbee

B. R. Patterson

Robin Griffin

John Barnard

Director of Graduate Program

Dean, UAB Graduate School

Date

PS-1428